COMPLIANT CONTROL OF ROBOTIC CO-WORKERS IN SURGICAL APPLICATIONS

A Thesis Submitted to
the Graduated School of Engineering and Sciences of
İzmir Institute of Technology
in Partial Fulfillment of the Requirements for the Degree of

DOCTOR OF PHILOSOPHY

in Mechanical Engineering

by
Orhan AYİT

January 2023
İZMİR

ACKNOWLEDGMENTS

First of all, I would like to express my sincere gratitude to my thesis advisor Prof. Dr. Mehmet İsmet Can DEDE, for his invaluable coaching and also sharing his experience and knowledge with me. During my graduate education, his academic advices and lectures made a high contribution to my engineering skills and intelligence.

I also state my deepest appreciation to my Ph.D. thesis members; Prof. Dr. Enver TATLICIOĞLU, Prof. Dr. Gökhan KİPER, Prof. Dr. Levent ÇETİN, and Assoc. Prof. Dr. Ahmet İlkay IŞIKAY for sharing with me their precious time and the valuable critics on my thesis.

I would like to acknowledge the financial support provided by The Scientific and Technological Research Council of Turkey (TUBITAK) through the project "NeuRobo-Scope - Robot Assisted Endoscope Control that can be Controlled by the Surgical Tools" under the grant 115E726 and 100/2000 CoHE (Council of Higher Education, TURKEY) Doctoral Scholarship.

I would like to thank my family for their support, encouragement, and endless love not only during my graduate period but also my life in general.

Thanks to my friends, İbrahim Can GÖRGÜLÜ, Furkan KÜÇÜKOĞLU, Rüstem Can ÖZTÜRK, Tuğrul YILMAZ, Mert YILMAZ, Hazal EMET, Merve ÖZKAHYA, and Murat DEMİREL for their friendship.

ABSTRACT

COMPLIANT CONTROL OF ROBOTIC CO-WORKERS IN SURGICAL APPLICATIONS

In recent years, robots have taken place in surgical operations due to their advantages over humans, such as power, endurance, dexterity, and accuracy. Because of the lack of abilities, such as decision-making, adaptability, and creativity, human surgeons supervise the robots. The robots share the operation places with humans, called co-worker robots. Robots have the power to harm their environment; therefore, robots can generate dangerous situations for surgeons and patients. To deal with the issues, this dissertation aims to design active compliant control algorithms such as impedance control, admittance control, and hybrid position/force control to achieve safe interaction forces in surgical operations by considering the performance. The surgical co-worker robot's type, actuation system, robot dynamics, and environment dynamics are important factors for designing the active compliant controller. Besides these, stability and robustness for safety, and agility and human effort for performance are considered for designing the controller. This dissertation takes into account three interaction scenarios encountered in surgical operations. In these scenarios, it is expected from the co-worker robot that it adapts to the sudden change in its environment dynamics. For instance, safe interaction is desired when the robot interacts with the stiff and soft tissues. To handle the issue, a switching control methodology is presented where the predefined control parameters are switched according to their environments. The methodology is implemented in a novel co-worker robot named NeuRoboScope, designed to assist the endoscopic pituitary gland surgery with the support of The Scientific and Technological Research Council of Turkey (TUBITAK). Moreover, active compliant control algorithms require a motion control algorithm as a low-level controller. In this dissertation, the computed torque method and independent joint controllers with gravity compensation are used as motion control algorithms. The computed torque method requires the dynamic model of the robot. Due to that, the dissertation proposes a simplified dynamic model with a correction coefficient for computational efficiency. ARM Cortex M4 processor runs the computed torque method with the proposed dynamic modeling method at $\approx 500\ Hz$. Also, this dissertation presents an independent joint controller which uses the simplified gravity matrix as a feedforward term for compensating the NeuRoboScope's gravitational effect. The experimental results of both controllers are discussed in this dissertation.

ÖZET

CERRAHİ UYGULAMALARDAKİ ROBOTİK EŞ-ÇALIŞANLARIN UYUMLU DENETİMİ

Robotlar son yıllarda insana göre güç, dayanıklılık, el becerisi ve isabetlilik gibi avantajlarından dolayı cerrahi operasyonlarda yerini almıştır. Robotlar; yetenek, karar verme, uyarlanabilirlik ve yaratıcılık eksikliklerinden dolayı insanların denetiminde çalışmalıdır. İnsanla birlikte çalışabilen robotlara eş-çalışan robotlar denir. Robotlar çevresine zarar verebilecek kuvvetler uygulayabilir ve bu durum cerrahlar ve hastalar için tehlikeli olabilir. Bu tezin amacı, empedans, admitans ve hibrit pozisyon/kuvvet denetleyicileri gibi aktif uyumlu denetleyici algoritmalarını, operasyon performanslarını göz önünde bulundurarak güvenli etkileşim kuvvetlerine ulaşmak için tasarlamaktır. Aktif uyumlu denetleyicilerin tasarlanmasında cerrahi iş birlikçi robotun tipi, eyleyici ve iletim sistemi, robot dinamikleri ve çevrenin dinamikleri kullanılmaktadır. Bunların yanı sıra, güvenlik için kararlılık ve gürbüzlük, performans için çeviklik ve insan eforu tasarım kriterleri olarak dikkate alınır. Bu tez, cerrahi operasyonlarda karşılaşılabilecek üç etkileşim durumundan bahsedecektir. Bu durumda iş birlikçi robottan, çevre dinamiklerinin ani değişimine uyum sağlaması beklenmektedir. Örneğin, operasyon sırasında robotun sert ve ya yumuşak bir doku ile temas edebilir ve robotun farklı dinamiklere sahip olan bu tip çevrelerle güvenli etkileşim sağlaması arzulanır. Sorunu ele almak için, önceden tanımlanmış denetleyici parametrelerinin ortamlarına göre değiştirildiği bir anahtarlama denetim metodolojisi sunulur. Metodoloji, Türkiye Bilimsel ve Teknolojik Araştırma Kurumu (TÜBİTAK) desteği ile endoskopik hipofiz bezi cerrahisine yardımcı olmak üzere tasarlanan NeuRoboScope adlı yeni bir iş birlikçi robotuna uygulanacaktır. Ayrıca, aktif uyumlu kontrol algoritmaları, düşük seviye olarak hareket denetleyici algoritmasına ihtiyaç duyar. Bu tezde, hareket denetleyeci algoritması olarak hesaplanan tork yöntemi ve bağımsız ortak denetleyeci yöntemi kullanılmıştır. Hesaplanan tork yöntemi, robotun dinamik modeline ihtiyaç duymaktadır. Bundan dolayı tezde hesaplama verimliliği için düzeltme katsayısına sahip basitleştirilmiş bir dinamik modelleme metodu önerilmiştir. ARM Cortex M4, önerilen dinamik modelleme yöntemiyle hesaplanan tork yöntemini yaklaşık $500Hz$'de çalıştırır. Ayrıca bu tez, NeuRoboScope'un yerçekimi etkisini telafi etmek için bir ileri besleme terimi olarak basitleştirilmiş yerçekimi matrisini kullanan bağımsız bir ortak denetleyici sunmaktadır. Bu tezde her iki denetleyicinin deneysel sonuçları tartışılmıştır.

I dedicate this dissertation to my parents.

TABLE OF CONTENTS

LIST OF FIGURES

Figure **Page**

Figure **Page**

Figure **Page**

Figure **Page**

Figure **Page**

Figure **Page**

LIST OF TABLES

Table **Page**

Table **Page**

CHAPTER 1

INTRODUCTION

Surgical operations are classified as open and minimally invasive surgery (MIS). In open surgeries, the tissues located in the operation area are cut by that way, a full view of organs is obtained for the surgeon. In contrast, the medical instruments and a camera named an endoscope are inserted through one or more tiny incisions or natural orifice of the body to view and operate the organs in MIS. Due to minimal incisions, mild pain, fast recovery, minor scars, and minimizing the risk of complications are achieved by MIS when compared to open surgeries (Jaffray, 2005). Despite these pros, the drawbacks of the MIS are the requirement of the specialized instruments & training, restricting the mobility & maneuverability, muscle fatigue, requiring more concentration during surgery, and increasing the surgery duration (Knott, 2013; Hanna and Cuschieri, 2008). The negative sides of MIS are based on the limits of the surgeon's physical capacity; for that reason, the robots have taken part in MIS to improve the efficiency of the surgery. The main reasons for using robots in such areas are better accuracy, higher precision, reliability, and higher endurance (Singh et al., 2013). Despite these advantages, the lack of the robot's abilities, such as decision making, creativity, adaptation, and flexibility, make humans maintain their contributions in the operation areas (Sherwani et al., 2020; Kanik et al., 2021). These reveal the requirement of humans to take place in working places with robots. Robots are capable of working or sharing the operation area with humans are called robotic co-workers. Co-worker robots are used to assist humans for physically and mentally challenging tasks. Since health-related situations can be changed instantly, co-worker robots must work under the supervision of surgeons who adapt to the different conditions quickly. Consequently, using co-worker robots in surgical applications has become necessary. In literature, these robotic systems used in surgery are called robotically-assisted surgical procedures (RASS).

One of the robotic co-worker systems named NeuRoboScope was designed in **Hu**man - **R**obot interaction laboratory (HuR) in Izmir Institute of Technology. The robot was funded by TUBITAK between 2016-2018. The robot aims to assist surgeons in endoscopic pituitary gland surgery procedures. In this type surgeries, the chief surgeon uses different surgical instruments such as an aspirator, curette, drill, and lancet in addition to the endoscope. When two of them are required to be used by a surgeon simultaneously,

the assistant doctor participates in the operation and controls the endoscope according to the chief surgeon's directives. However, the assistant doctor encounters important problems during the surgery. One of the significant problems is the weight of the endoscope, which is heavier than other medical instruments. Physical fatigue has appeared since the doctor holds the endoscope during prolonged operations. Another significant issue is the communication problem between a chief and assistant surgeon. Because of this, the coordination between surgeons is lost, and undesired surgical location is monitored with an endoscope. Also, that results in decreasing the performance of surgery. To deal with these issues, a novel co-worker robot NeuRoboScope shown in Fig. 1.1a was designed to hold and control the endoscope according to the surgeon's commands. The commands are given by using the ring-shaped remote controller, shown in Fig. 1.1b.

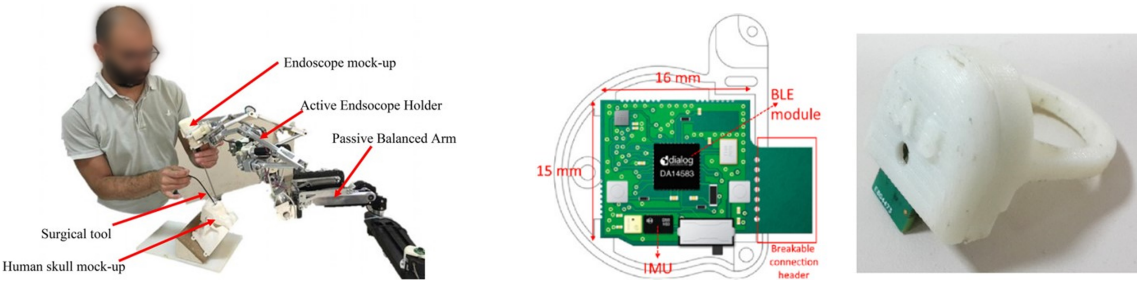

(a) The NeuRoboScope system tested by a surgeon

(b) DA14583 IoT Sensor; used as a remote controller

Figure 1.1. The components of the NeuRoboScope system (Source: Dede et al., 2021)

To achieve high performance in surgery, the NeuRoboScope follows the motion commands with a minimum deflection. In other words, the robot shows stiff behavior. However, the motion of the NeuRoboScope can be constrained by a surgeon, soft tissues, muscles, bones, and medical instruments, as seen in Fig. 1.1a. This unintended collision or contact between the stiff robot and its environment generates unexpected forces which might induce undesired situations such as instability or devastation of its environment. To deal with these issues, the pysical interaction became a significant research area in literature. The studies proposed the passive and active compliant control methods (Howell, 2013; Villani, 2008). The passive compliant control method manipulates mechanical stiffness; however, active compliant control algorithms modify the motion trajectory of the robot to provide safe interaction. Even though basic methodologies have been proposed to achieve the desired passive or active compliance, the design and implementation of the methods in systems having both discrete and continuous behavior, such as surgical

co-worker robots, are still a significant problem in the literature.

1.1. Aim of the Dissertation

The standards of safety characteristics and performance for RASS were published in IEC 80601-2-77 (ISO, 2019) where it is emphasized that the manufacturer must consider the speed of robotically assisted surgical equipment (RASE) inside or outside the patient. Also, the risk assessment of the designer includes the risk of collision between human and robot (UL, 2019). Therefore, the applied interaction forces/torques on the patient and the hand speed of the surgeon during surgery must be measured before designing the compliant controllers. Chapter 2 presents this information for the endoscopic pituitary gland procedure as a preliminary study of this dissertation. By using this information, the desired impedance for the co-worker robot will be calculated. This dissertation only focuses on well-known active compliant control algorithms in terms of impedance control, admittance control, and hybrid position/force control algorithms.

- **The aims of the dissertation are listed as follows;**

(I) The first aim of the dissertation is to determine the appropriate compliant control algorithms according to the type of co-worker robot (types of the surgical co-worker robot will be given in Chapter 2), environment dynamics, and desired interaction with its environments.

(II) Another aim of the thesis is to design the proper well-known active compliant control algorithms to achieve desired interaction between the surgical co-worker robot and its environments by considering the performance metrics.

(III) In surgical operations, the co-worker robot interacts with more than one environment with different dynamics. Therefore, the active compliant control algorithm must be adaptable for different dynamics. However, the traditional algorithms are designed for a specific environment. The dissertation aims to solve this issue.

(IV) The active compliant control algorithms modify the motion trajectory of the robotic co-workers' systems to achieve the desired behavior. Therefore, the precise motion control algorithms must be implemented as low-level controllers. To design most of the motion control algorithms, such as adaptive or computed torque method, the dynamic model of the robot is required. Due to computing the robot dynamics, embedded systems with high computational efforts are required to run these algorithms at high frequencies.

Another goal of this dissertation is to propose a computational efficient computed torque method.

(V) The designed control algorithms are aimed to be implemented in the novel surgical co-worker robot NeuRoboScope.

1.2. Contributions

- **The contributions of the dissertation are listed as follows;**

(I) The first contribution of the dissertation is that the control algorithms are designed and implemented in a novel co-worker robot named NeuRoboScope, which was designed to assist endoscopic pituitary gland surgeries.

(II) Another contribution of the thesis is proposing a computational efficient computed torque method that allows designers to use relatively cheaper processors in robotic surgical applications. The calculation of the NeuRoboScope's dynamics covers the dominant parts of the processor's computational efforts. The terms in the model related to acceleration, velocity, and inertia are analyzed, and the insignificant terms are neglected to simplify the dynamic model. To obtain accurate results, a new correction coefficient formula is proposed.

(III) In this dissertation, three scenarios are designed that are related to the interaction of the surgical co-worker robot. The proper compliant control algorithms are determined for each case and the controllers' parameters are designed and optimized by considering the safety and performance criteria.

(IV) The main contribution of the thesis is presenting a switching methodology for the surgical co-worker robot, which encounters environments having different dynamics. In this methodology, the optimum gains of the active compliant control algorithms are designed for each environment. The gains of the controllers are switched according to the environment. This methodology provides simplification and effectiveness for designing and implementing the controllers.

1.3. Dissertation Outline

The dissertation is outlined as

- **Chapter 2** aims to familiarize the reader with the topics included in the dissertation. Firstly, the surgical robots will be categorized, and the examples for each robotic

type will be mentioned. Then, the concepts used in the dissertation and the compliant control methodologies used in the literature are explained. Moreover, the performance metrics in the literature will be examined for physical human-robot interaction. Consequently, the preliminary studies for the NeuRoboScope will be explained.

- **Chapter 3** presents the derivation of the mathematical models of the NeuRoboScope in terms of kinematics and dynamics. The robot dynamics will be derived by using recursive Newton-Euler formulation, which is a computationally efficient method. The relatively cheaper processor, ARM Cortex M4 cannot run the dynamic model at high frequencies. For that reason, Chapter 3 presents a simplified dynamic model with a new correction coefficient model to obtained to computationally efficient dynamic model.

- In **Chapter 4**, the computed torque method with using the simplified dynamic model and independent joint control method are designed and implemented in the NeuRoboScope. The experimental results of two control methods are presented, and the results are discussed.

- **Chapter 5** discussed the safety and performance criteria.

- **Chapter 6** presents the two interaction scenarios for the teleoperated surgical co-worker robot. The proper controller is chosen for each scenario, and the methodology of finding optimum gains of the active compliant control methods is explained by considering safety and performance criteria. In addition, the switching methodology for surgical co-worker robots is presented for the system having environments that change instantaneously. The experiments of the active compliant control algorithms are done.

- **Chapter 7** presents an interaction scenarios for the "hands-on" controlled surgical co-worker robot. The proper controller is chosen and the optimum gains of the active compliant control method is explained by considering safety and performance criteria. The experimental studies of the active compliant control algorithms are done.

- **Chapter 8** discusses the results and concludes the dissertation.

CHAPTER 2

BACKGROUND

This section aims to review the surgical co-worker robots and give information about stiffness, compliance, impedance, admittance, backdrivability concepts, and methods to reach the desired interaction between the robot and its environment. In addition, the performance metrics will be discussed, and the preliminary studies, such as workspace studies and the tissue modeling, will be explained.

2.1. Surgical Robots

The use of robots has become widespread in surgical applications to deal with the issues mentioned in Chapter 1. According to the level of involvement of surgeons in operation, the autonomous behaviors of robots are varied. Yang et al. (2017) categorized the surgical robots as levels 0 to 5 according to autonomy.

No automation (Level 0) robots follow the given commands by the surgeon. The robots suspense the hand tremor and scale the motion of surgeon, for instance, Da Vinci (Broeders and Ruurda, 2001), Zeus (Beasley, 2012), and SPORT (Gosrisirikul et al., 2018).

Robot assistances (Level 1) are controlled by the surgeon. The robot assists the surgeon by giving feedback and constraining or modifying the surgeon's motion. The robots with level 1 autonomy are tracking the tool (McKenna et al., 2005), sensing the interaction of tissue (Konstantinova et al., 2014), and giving haptic feedback (Konstantinova et al., 2014).

Robots having the **Task automation (Level 2)** perform the tasks in determining conditions by surgeons without being controlled by surgeons. Moreover, these robots also allow surgeons to control themselves, similar to robot assistances. Some of the robots with level 2 automation are robot stitching with a needle (Nageotte et al., 2009), STAR (Leonard et al., 2014), and a robot retracting the tissue (Patil and Alterovitz, 2010).

Robots with **Conditional autonomy (Level 3)** have been capable of updating or designing the new strategy based on the surgeons' operation strategy by utilizing the information from its sensors. The studies on the conditional autonomy of surgical robots

are presented in (Osa et al., 2014; Jackson et al., 2018; Fagogenis et al., 2019).

High autonomy (Level 4) provides the robots to plan the strategy autonomously. Surgeons supervise the robot when it is required. The high autonomous robots in surgical applications are presented in (Hu et al., 2016; Li et al., 2018; Nichols and Okamura, 2013)

At the **Full autonomy(Level 5)** level, robots do not require surgeons to complete surgery; however, no such surgical robot has full autonomy in literature.

The reader can find more details on the autonomy of the surgical robot in (Attanasio et al., 2021).

2.1.1. Surgical Co-worker Robots

This dissertation focuses on the co-worker robots that have level 1 autonomy in which surgeons control the robot during surgery and the robot is capable of perceiving the environment. Gomes (2011) categorized the co-worker robots as teleoperated and "hands-on" controlled robots.

Teleoperation can be described as controlling the action of a system or robot at a distance. A teleoperation system consists of master and slave systems. The master system sends commands, and the slave system performs the action according to them. The surgeon and a remote controller form the master part of robotic surgical operations. The teleoperated robot is the slave part of the system. The teleoperation system is categorized as unilateral and bilateral according to the information transitions between the master and slave systems.

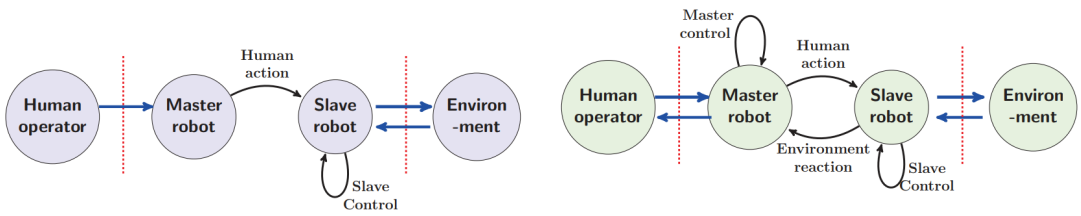

(a) Unilateral teleoperation system (b) Bilateral teleoperation system

Figure 2.1. Unilateral & bilateral teleoperation systems (Source: Albakri, 2015)

As seen in Fig. 2.1, the operator's commands are only transmitted from the master to the slave in unilateral teleoperation; however, the slave does not share the information with the master. In contrast, the slave in bilateral teleoperation informs the master about

the environment by sending the proper position or force data while executing the commands of the master. Sutherland et al. (2013) presented a teleoperated robotic co-worker NeuroArm which the surgeon controls at distance. Two force/torque sensors are attached between the robot and its environment for measuring the interaction forces; therefore, the haptic feedback is provided to the surgeon. In (Schoonmaker and Cao, 2006), a vibrotactile feedback system was proposed for teleoperated surgical robots. The vibrotactile force information is transmitted to the surgeon to sense the softening of the tissues.

"Hands-on" indicates that the operator is a part of the control loop of the system. "Hands-on" controlled surgical co-worker robots have physical interaction with the operator during surgery in contrast to teleoperated robots. Jakopec et al. (2002) presented the Acrobot for knee replacement surgery. The surgeon holds a handle located at the Acrobot's tip to move the robot. While the surgeon moves the robot freely within the predefined safe region, the robot behaves as stiff outside this region. Another "hands-on" controlled surgical co-worker robot, "Steady Hand" for microsurgery, was presented in (Taylor et al., 1999). The surgeon and robot grasp a same medical tool simultaneously, and the robot's sensors measure the surgeon's exerted force. By using this information, the smooth motion of the surgical instrument is obtained.

2.2. Compliant Control

Co-worker robots in surgery share their workspace with bones, muscles, and tender tissues, which are vulnerable when considering the power of the robots. These tissues can be exposed to irreversible damage since the interaction with robots occurs. Also, the surgical instruments handled by surgeons can collide with the co-worker robot, which might induce instability. In literature, compliant control methods were proposed to avoid interaction problems, categorized into passive and active compliant control methods (Khan et al., 2014). Before reviewing the compliant control methods, the basic concepts related to compliant control will be explained next section.

2.2.1. Stiffness, Compliance, Impedance & Admittance

Hooke discovered the linear relation between force and deflection of spring in the 1660s (Moyer, 1977). The ratio of force to deflection is called stiffness, indicating

resistive force in response to deformation (Baumgart, 2000). Stiffness is formulated as:

$$\kappa = -\frac{F}{\Delta x} \tag{2.1}$$

where κ, F and Δx refer to stiffness (N/m), force (N) and deflection (m), respectively.

The stiffness of a robotic system can be calculated by using Hooke's law, and for instance, a single degree of freedom robot is modeled as

$$F_{ext} = f(x, \dot{x}, \ddot{x}) \tag{2.2}$$

where F_{ext} and x are external forces applied under robot manipulator and robot's position, respectively.

The stiffness of that model is obtained as follows;

$$\kappa = \frac{\delta f(x, \dot{x}, \ddot{x})}{\delta x} \tag{2.3}$$

Compliance term is generally defined as the inverse of stiffness in mechanics, shown as $c = \kappa^{-1}$ and this concept can be defined as responses of robots to resistive forces (Vukobratovic and Tuneski, 1994). Compliance is directly proportional to the deflection, as seen in Eq. 2.1. Because of the deflection, compliance has an adverse effect on accuracy. In robotic applications which require high accuracy, such as CNC machines, the desired property is ideally zero compliance (or infinite stiffness) of the system. In real-life implementations, compliance of mechanics cannot be zero, and thus, the studies such as (Ciblak and Lipkin, 1999; Drouet et al., 1998; Howard et al., 1998; Pashkevich et al., 2009; Yi and Freeman, 1993) were done for modeling the mechanical compliance to compensate it. In contrast, this property is beneficial in providing safe interaction. The interaction between the robot and its environment results in external forces that are absorbed by using compliance property; therefore, the robot complies with its environment. The methods for obtaining compliant robots are explained in detail later.

Impedance (Z) term refers to the total resistance encountered by the current when it passes through a circuit, and it makes researchers understand the relationship between voltage (E) and current (i), shown as:

$$Z = \frac{E}{i} \tag{2.4}$$

This mathematical model can be used in mechanical systems for relating force to velocity. For obtaining this, the analogies between mechanical and electronic systems were built by two methods which are force-velocity (direct analogy) and force-current (dual analogy) analogies (Ogata, 2004).

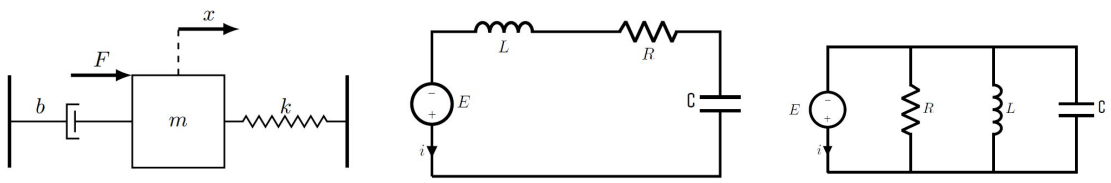

(a) (b) (c)

Figure 2.2. (a) Mass-Spring-Damper system (Source: Burchett, 2005), (b) Serial RLC circuit, (c) Parallel RLC circuit

In the energy domain, power variables such as flow and effort have identical roles. Maxwell proposed the direct analogy where effort variables were chosen as force and voltage; also, velocity and current were chosen as flow (Borutzky, 2009). By that way, the analogy between a parallel mass-spring-damper mechanical system and serial resistor-inductance-capacitance circuit models was introduced. The differential equations of a parallel mechanical system and a serial RLC circuit seen in Fig. 2.2 have the same form, and the analogies of components are shown in Table 2.1.

- The parallel mathematical model of mechanical system;

$$m\frac{\partial^2 x}{\partial t^2} + b\frac{\partial x}{\partial t} + kx = F \tag{2.5}$$

- The mathematical model of serial RLC circuit;

$$L\frac{\partial^2 \mathbb{Q}}{\partial t^2} + R\frac{\partial \mathbb{Q}}{\partial t} + \frac{1}{\mathsf{C}}\mathbb{Q} = V \tag{2.6}$$

Table 2.1. Analogous of the electrical and the mechanical systems: Force - Voltage Analogy

Force/ Torque (F/T)	Voltage (E)
Mass/ Moment of Inertia (m/I)	Inductance (L)
Damping Constant (b)	Resistance (R)
Spring Constant (k)	Reciprocal of Capacitance $(1/\mathsf{C})$
Linear/ Angular Displacement (x/θ)	Charge $(\mathbb{Q})$
Linear/ Angular Velocity $(\dot{x}/\dot{\theta})$	Current (i)

Firestone remarked on the deficiencies of force-velocity analogy in (Firestone, 1933) such as:

- Forces is measured from one node; however, voltage is measured by using two nodes in space. This shows the lack of force-velocity analogy.
- Mechanical elements in parallel are represented with a serial RLC circuit.
- Mechanical impedance in series is calculated as reciprocal of summing reciprocal of mechanical elements' impedances. However, electrical impedance in series is calculated by adding the impedances of electronic components.

To avoid the mentioned deficiencies, Firestone proposed a new analogy between mechanical and electronic systems in 1933, and it is called force-current or dual analogy. According to this method, the models of the parallel mass-spring-damper mechanical system and parallel resistor-inductance-capacitance circuit are analog, as seen in Table 2.2.

- The mathematical model of parallel RLC circuit as seen in Fig. 2.2;

$$\mathbb{C}\frac{\partial^2\Psi}{\partial t^2} + \frac{1}{R}\frac{\partial\Psi}{\partial t} + \frac{1}{L}\Psi = i \tag{2.7}$$

where $E = \frac{\partial\Psi}{\partial t}$ also, Ψ and i refer to flux and current.

Table 2.2. Analogous of the electrical and the mechanical systems: Force - Current Analogy

Force/ Torque (F/T)	Current (i)
Mass/ Moment of Inertia (m/j)	Capacitance $(\mathbb{C})$
Damping Constant (b)	Reciprocal of Resistance $(1/R)$
Spring Constant (k)	Reciprocal of Inductance $(1/L)$
Linear/ Angular Displacement (x/θ)	Magnetic Flux (Ψ)
Linear/ Angular Velocity $(\dot{x}/\dot{\theta})$	Voltage (E)

Mechanical impedance is a way to measure the resistance to motion when exposed to a given force (Sabanovic and Ohnishi, 2011), and this is calculated by using the force-voltage analogy;

$$Z = \frac{F}{\dot{x}} \tag{2.8}$$

Admittance (Y) in mechanics refers to the measurement of motion under applied force, and it is mathematically equal to the inverse of impedance, shown as;

$$Y = \frac{\dot{x}}{F} \tag{2.9}$$

To reach desired physical contact between the robot and its environment, stiffness/compliance or impedance/admittance properties can be regulated. Due to that, these mechanical properties have a significant place on passive and active compliant control methods.

2.2.2. Concept of Backdrivability

Pure backdrivability is obtained by achieving zero impedance; therefore, the backdrivability can be defined as the indicator of the easiness of transmitting applied forces on the output axis to the motion of the input axis (Ishida and Takanishi, 2006). The backdrivability is required when the interaction occurs because it advances safety and adaptability with the environment (Fujimoto et al., 2009). In contrast, applications, that avoid losing power, desire non-backdrivability (Sensinger and Weir, 2005). Actuators without any transmission systems are called "direct-drive" and they have the best backdrivability except for the hydraulic one; in addition, the capstan drive transmission system is proper for use in backdrivable system (Perret and Vercruysse, 2014). Moreover, structurally non-backdrivable systems can be driven backward by active compliant control strategies.

In literature, backdrivability is categorized into acceleration dependent and velocity-dependent (Townsend, 1988). Good acceleration-dependent backdrivability refers to small inertia-induced force. This is provided by minimizing inertia and keeping the transmission ratio relatively small (Najafi and Sepehri, 2008). Also, good velocity-dependent backdrivability implies the small friction-induced force that resists the end-effector motion (Townsend and Salisbury, 1993).

As it is understood, backdrivability is a way to reach desired forces when the interaction occurs. As mentioned previously in the section, desired interaction is also obtained by regulating the compliance property of the robot. Due to these, the backdrivability must not be confused with compliance as discussed in (Calanca, 2014). For example, a non-backdrivable robot with flexible links and a backdrivable robot with stiff links can achieve a similar physical interaction with their environments.

2.2.3. Passive Compliant Control

Passive compliant control is one way to provide safe interaction between a co-worker robot and its environment. In this controller, the interaction forces change the

trajectory of the robot's end-effector due to the inherent compliance of the robot (Villani, 2008). In literature such as (Schiavi et al., 2009; Rice and Schimmels, 2018; Van Ham et al., 2009), the inherent compliance is adjusted actively to achieve desired compliance. This is called passive compliant control. However, these implementations are not compatible with the passive word, which means adapting to situations without excitation. Due to avoid this confusion in the literature, this thesis will be discussed inherent compliance instead of passive compliant control.

2.2.4. Inherent Compliance of Robots - Material

Material is one of the significant concepts to determine the behavior of robots under external forces. In traditional robotics, rigid materials have been used. These robots handle limited tasks with specialized end-effectors, and they are called hard robots (Trivedi et al., 2008). The robots are not suitable for performing tasks such as surgical operations, including unpredictable obstacles. Therefore, soft robots such as an active ankle-foot (AFO)(Blaya and Herr, 2004), second-skin (Goldfield et al., 2012) and PneuNets (Ilievski et al., 2011), have been designed by using soft materials.

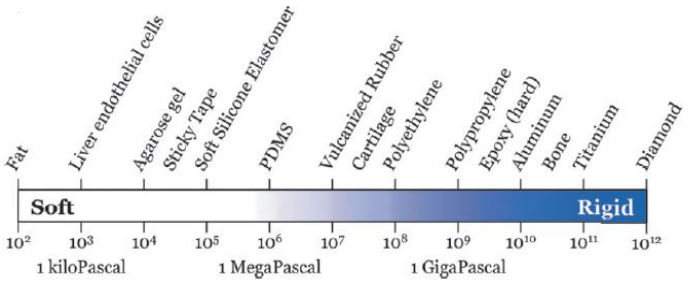

Figure 2.3. Elasticity of the different materials (Source: Majidi, 2014)

The rigidity of the materials is determined with Elastic (Young's) modulus as seen in Fig 2.3. The material is described as hard when Young's modulus of it is greater than 10^9 Pa; moreover, it is identified as soft when Young's modulus is between 10^2 Pa and 10^6 Pa (Majidi, 2014).

2.2.5. Inherent Compliance of Robots - Kinematic Structure

The kinematic structure of a robot is one of the criteria for stiffness, and it is categorized based on the structural topology. Serial and parallel robots, which have forms as an open-loop chain and closed-loop chain, respectively, are the main kinematic structures of robots. Another type of kinematic structure is called a hybrid, and this form includes both open loop and closed loop chains. The characteristic of serial and parallel robots are shown in Table 2.3. For hybrid robots, the mentioned features can be advanced or regressed according to the form of kinematic structure.

Table 2.3. Characteristics of serial and parallel robots (Source: Pandilov and Dukovski, 2014)

Features	Serial Robot	Parallel Robot
Workspace	Large	Small & Complex
Position Error	Accumulates	Averages
Force Error	Averages	Accumulate
Accuracy	Low	High
Speed & Acceleration	Low	High
Stiffness	Low	High
Inertia	Large	Small
Payload/Weight ratio	Low	High

Table 2.3 reflects that parallel robots are more stiffer than serial robots which results in high accuracy and lesser position error. Also, this refers that parallel robots have less compliance when compared with serial robots. As mentioned above, compliance is an important criterion for safe interaction and adapting to the environment. The payload to weight ratio must be underlined. The parallel manipulators can apply the same force as a serial robot to the environment with lighter links which also improves the compliance of robots.

2.2.6. Active Compliant Control

Active compliant control is a methodology to reach desired interaction between a robot and its environment by manipulating the compliance and dynamic of the system (Schumacher et al., 2019). Similar to (Schumacher et al., 2019; Villani, 2008), the active compliant controller can be categorized into the direct and indirect controllers as seen in

Fig. 2.4. In direct-type controllers, desired interaction is obtained by directly controlling the positions or forces. In contrast, indirect type controllers aim to reach target impedance or dynamics rather than tracking the desired force or position references. In the scheme below, the implicit or explicit controller is determined according to the absence or presence of the force sensor, respectively (Poignet and Bayle, 2012).

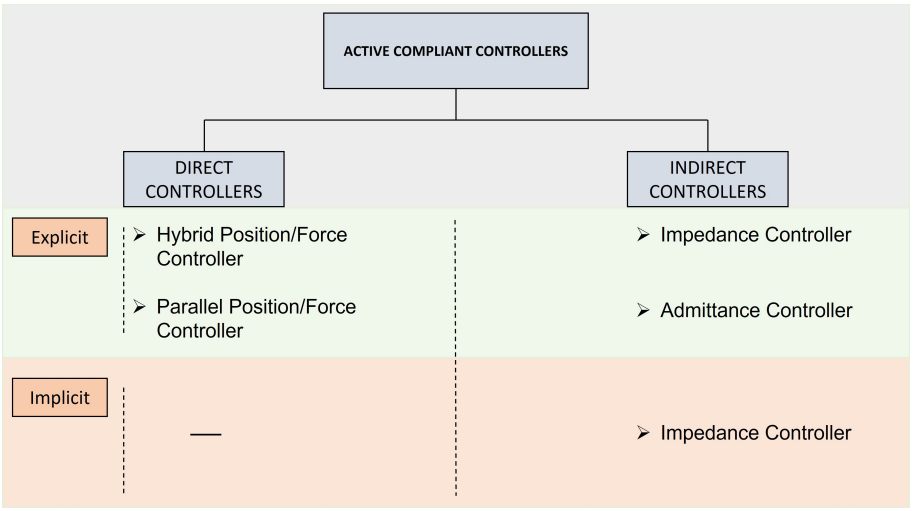

Figure 2.4. Active compliant control scheme

2.2.6.1. Impedance Control

In impedance control, the relationship between motion and exerted force of the robot's end-effector is designed by that way, the desired interaction between the robot and its environment is reached. The main difference between this control algorithm and the traditional one is ensuring to do tasks by achieving the target impedance rather than tracking the given position or force reference. The target impedance is generally chosen as a second-order function that describes a linear mass-spring-damper model.

The first impedance control algorithm proposed by Whitney (1977) is also called accommodation or damping control. In this control approach, the measured force signal F_m is converted to velocity modification signal $\dot{x}_m$ by multiplying the force feedback matrix K_f, which is a diagonal matrix and it determines the behavior of interaction. K_f is a 1×1 matrix since the damping control approaches is implemented to one DOF system in Fig. 2.5 where $\dot{x}_c$, $\dot{x}_d$, e, u, x, T and X_e refer to velocity command, desired velocity, position error, control input, measured position state, torque, and known environment po-

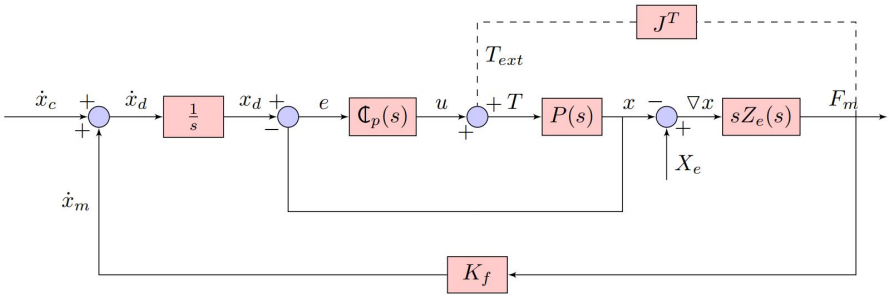

Figure 2.5. Damping control scheme (represents the controller applied to one DOF system)

sition, respectively. Also, the blocks $\mathbb{C}_p(s)$, $P(s)$, $Z_e(s)$ and J^T in the scheme imply the transfer function of the position controller, plant, environment impedance and Jacobian matrix. T_{ext} defines the external torque generated due to interaction. Salisbury (1980) proposed another impedance control called as stiffness control which depends on basic stiffness formulation in Eq. 2.3. In this approach, the difference between position command x_c and actual position is converted to desired force by using a diagonal stiffness matrix K_s. The matrix is a 1×1 in Fig. 2.6 where the desired force trajectory F_d is tracked by a robot. $\mathbb{C}_f$ refers to the force controller.

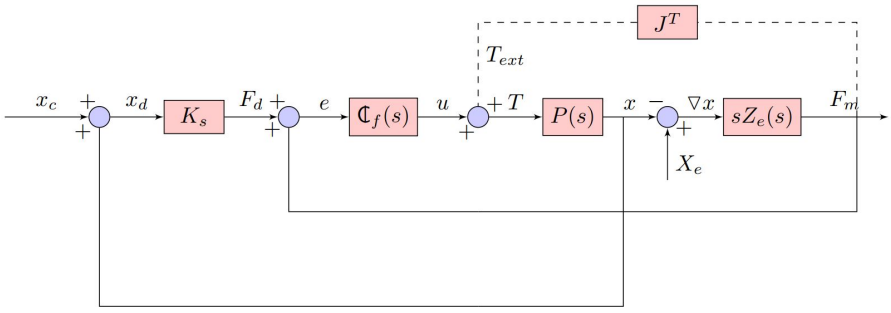

Figure 2.6. Stiffness control scheme (represents the controller applied to one DOF system)

The general and valid definition of impedance control was done by Hogan, and he stated that the robot behaves as impedance if the environment is admittance or vice versa, which is the underlying theory of the impedance control. It is inferred from the theory that the desired interaction can be reached by regulating the impedance of the robot, which controls the position and interaction force of the system simultaneously and

not independently. The explicit impedance controller can be divided into force-based and position-based impedance control (Surdilovic and Vukobratovic, 2002).

In force-based impedance control, the low-level controller cancels non-linearities and tracks the desired impedance. This control approach is sensitive to unknown dynamics. Friction or uncertainties in gears have negative effects on this approach; for that reason, the controller is effective for direct-drive robots. Position-based impedance control modifies the position reference according to the admittance gain $Y(s)$. Position control deals with uncertainties in the model and tracks the position reference as a low-level controller.

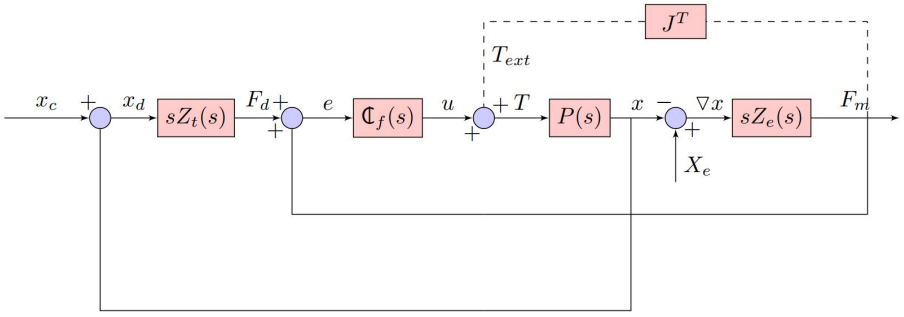

Figure 2.7. Forced-based impedance control scheme (represents the controller applied to one DOF system)

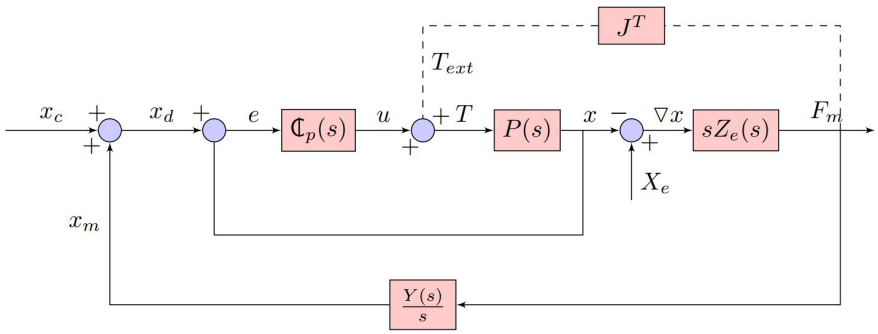

Figure 2.8. Position-based impedance control scheme (represents the controller applied to one DOF system)

Implicit impedance control does not need to measure force information or force feedback. In this control scheme, as presented in Fig. 2.9, the position error is converted to force by impedance gain, and the force is directly applied to the system as a control input. This control method is suitable for backdrivable systems. In contrast, explicit controllers can be implemented both non-backdrivable and backdrivable systems.

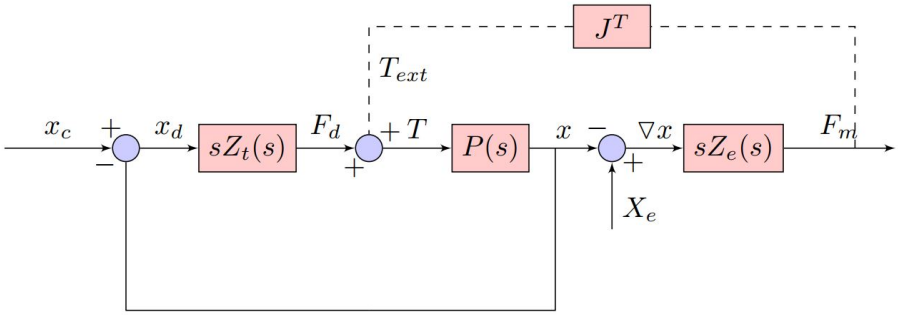

Figure 2.9. Implicit impedance control scheme (represents the controller applied to one DOF system)

2.2.6.2. Admittance Control

The admittance control term was firstly proposed in 1992 and used in (Newman, 1992; Gullapalli et al., 1992; Schimmels and Peshkin, 1994). However, position-based impedance control was named an admittance control in (Keemink et al., 2018). This dissertation uses the admittance term for all types of force to desired motion relationships and impedance term for all types of motion to desired force relationships which are also seen as the main difference between the two control algorithms. Due to that, admittance control can be defined as an opposite or dual of the impedance control. In contrast to impedance control, admittance control has good performance to render stiff walls, not good for rendering low inertia (Keemink et al., 2018), also admittance control makes the systems backdrivable. Similar to impedance control, admittance control aims to reach desired interaction by manipulating the relationship between the force and motion of the system. In the admittance control scheme, as seen in Fig. 2.10, force error is converted to position reference signal by using admittance gain, and the desired force or interaction is reached by tracking the generated position trajectory. Admittance gain is commonly chosen as a second-order function that describes a mass-spring-damper system.

2.2.6.3. Hybrid Position/Force Control

A hybrid position/force control algorithm was firstly presented by Raibert and Craig (1981) and in this control approach, a control strategy proposed by Mason (1981) was used. In this strategy, constrained surfaces were defined as natural constraints. The artificial constraints were designed based on the tasks of the robot and the natural con-

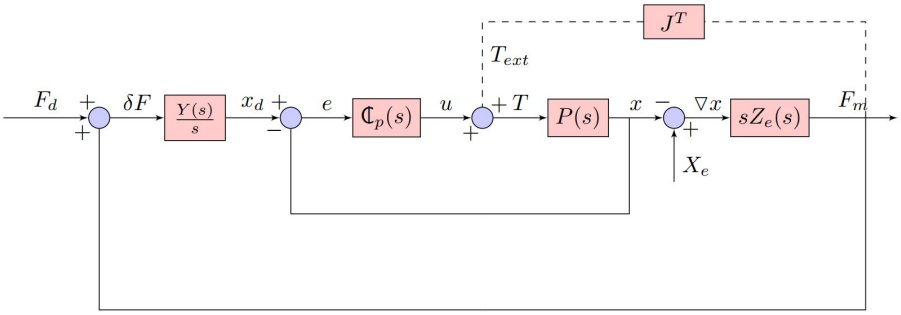

Figure 2.10. Admittance control scheme (represents the controller applied to one DOF system)

straints. Mason stated that the artificial constraints were chosen as orthogonal to the natural constraint according to the proposed strategy. By using obtained artificial constraints, the direction was determined where the force or position controller was applied.

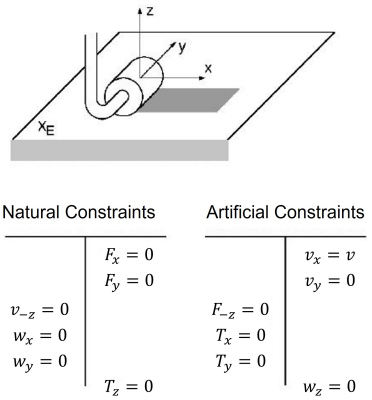

Figure 2.11. The constraints for the surface sliding hybrid position/force control task (Source: Surdilovic and Vukobratovic, 2002)

According to Fig. 2.11, the linear velocity in the x and y-directions and the angular velocity in the z-direction must be controlled. Moreover, the control algorithms for forces in z-direction and torques in x and y-directions must be applied to complete the desired contact task of a robot.

In the hybrid position/force control algorithm shown in Fig. 2.12, force and position are controlled independently. The diagonal $\hat{S}$ and its orthogonal complement $\hat{1} - \hat{S}$ matrices are designed to determine the directions of the implementation of the position control and force control, respectively. $\hat{1}$ refers to an identity matrix. The diagonal elements of these selection matrices consist of 1 or 0 values. For instance, in the force control

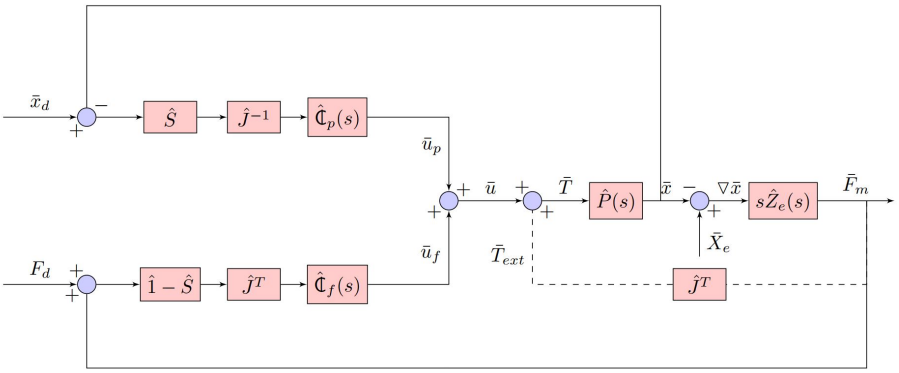

Figure 2.12. Hybrid position/force control scheme is proposed in (Source: Raibert and Craig, 1981).

algorithm, the position-controlled directions are multiplied by zero; therefore, only force control is applied in the determined direction and vice versa. In Fig. 2.12, u_p and u_f refer to position and force control inputs in joint space, respectively.

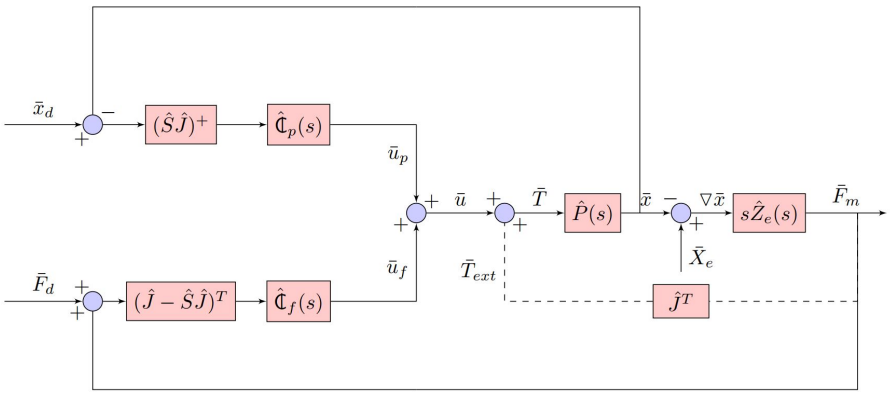

Figure 2.13. Hybrid position/force control scheme is proposed in (Source: Fisher and Mujtaba, 1992).

An and Hollerbach (1987) proved that certain well-known control algorithms, which include hybrid position/force control, are unstable. In (Zhang, 1989), it was shown that this control algorithm behaves as unstable in the certain kinematic configuration of the robots with revolute joints. Instability due to kinematic reasons is called kinematic instability (Zemiti et al., 2006). Fisher proved that the kinematic instability was not an inherent problem of the hybrid position/force control algorithm, and the instability occurred due to the deformation of the Jacobian matrix in Fig. 2.12. Fisher proposed a new hybrid position/force control scheme as seen in Fig. 2.13 where the pseudo inverse

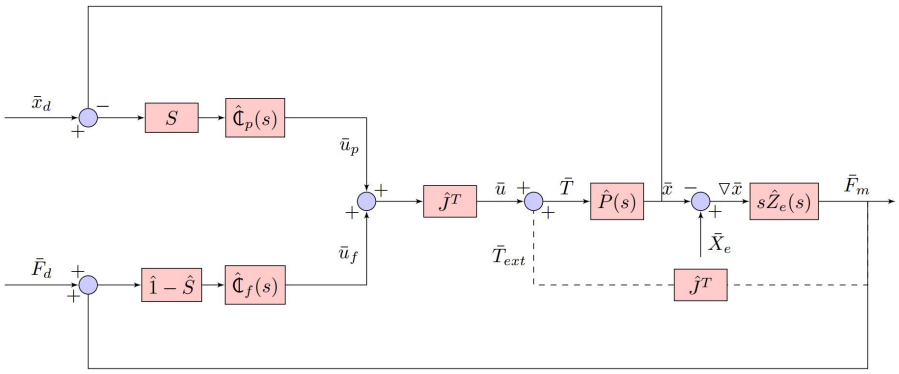

Figure 2.14. Hybrid position/force control scheme is proposed in (Source: Khatib, 1987).

of the multiplication of $\hat{S}$ and $\hat{J}$ was used to avoid the kinematic instability (Fisher and Mujtaba, 1992). This operation is shown as $(\hat{S}\hat{J})^+$ in Fig. 2.13. In addition, the kinematic instability is only observed when force and position values are controlled in joint space; therefore, controlling these parameters in task space is also a solution to eliminate the instability. The control scheme in Fig. 2.14 was proposed by Khatib where the force and position control algorithms are applied in task space(Khatib, 1987) .

In contrast to impedance or admittance control, the hybrid position/force control approach is sensitive to uncertainties of the environment model because the selection matrix $\hat{S}$ is designed according to a particular model. Therefore, matrix $\hat{S}$ must be altered for each specific task. The advantage over impedance control, the force, and position are controlled directly and simultaneously.

2.2.6.4. Parallel Position/Force Control

Chiaverini proposed the parallel position control algorithm (as seen in Fig. 2.15) to reach the desired interaction with controlling force and position directly and robustly (Chiaverini and Sciavicco, 1988). In this approach, position and forces are controlled simultaneously along any degree of freedom; therefore, this control approach does not require a selection matrix S in contrast to the hybrid position/force control approach. Another advantage of that controller is the self-adjustment of minor planning errors, which makes the controller robust. In this approach, position and force controllers are generally chosen as PD and PI, respectively. Due to the integral part, force control is the dominant

controller in the scheme. PD control allows for limited deviation from position trajectory. However, the force controller makes the force error goes to zero.

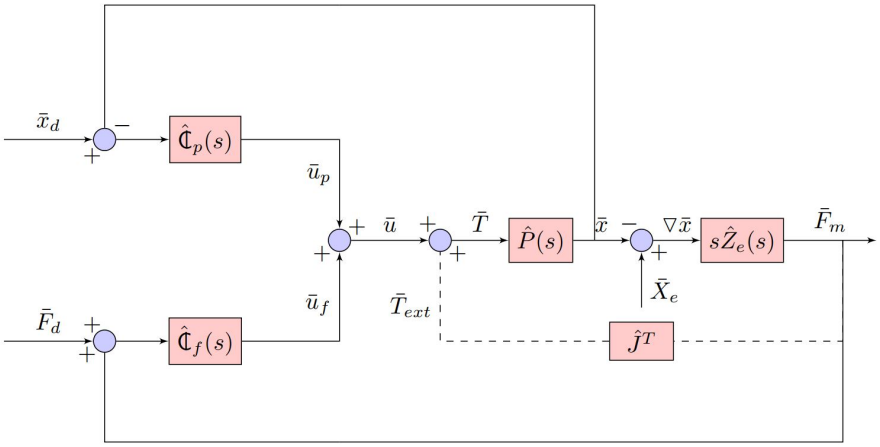

Figure 2.15. Parallel position/force control scheme

2.3. Performance Metrics for Human Robot Interaction

The performance criteria for human-robot interaction (HRI) must be designed in order to improve the efficiency of the tasks performed by humans and robots. In the review done by Murphy and Schreckenghost (2013), the metrics for HRI were investigated into three main groups human, robot, and general system metrics.

Olsen and Godrich proposed Neglect Tolerance (NT), Interaction Effort (IE), Robot Attention Demand (RAD), Free Time (FT) and Fan-out (FO) metrics for HRI (Olsen and Goodrich, 2003; Goodrich and Olsen, 2003). These metrics are designed to evaluate the performance of the robot. The NT metric evaluates how long the robot worked on a task with adequate performance without being guided by a human. The operator first gives a command and then neglects the robot. The robot's performance is expected to decrease without being supervised by a human. Time elapsed between the excitation command and the robot underperforming for completing the task is used as a measurement of NT, which is related to the autonomy of the robot. Another metric is the IE which measures how long the robot and the human interact. Olsen and Goodrich (2003) stated that this criterion is difficult to obtain experimentally, so an estimated value is obtained by using the NT and FO metrics. The RAD metric investigates the ratio of the time that a human interacts with the robot to the total time spent by the human for

completing tasks. Its mathematical representation is shown below.

$$RAD = \frac{IE}{IE + NT} \tag{2.10}$$

The FT metric indicates the time period for not supervising the robot by a human while completing the task. The metric is calculated as follows;

$$FT = 1 - RAD \tag{2.11}$$

The FO metric indicates how many robots a human can interact with simultaneously and effectively while completing a task. Its mathematical formulation is represented as follows;

$$FO = \frac{1}{RAD} \tag{2.12}$$

Saleh and Karray (2010) proposed two important metrics regarding the human part in HRI. These criteria are Human Reliability (HR) and Human Trust (Tr), and these metrics contributed to the development of the RAD and FO metrics mentioned above. While the FO metric specifies the number of robots that humans can interact with simultaneously, it does not include the limit of human capacity. Due to the psychological, physiological, and sociological effects, the performance of humans can be altered. An HR metric ranging from 0 to 1 was designed to indicate the skill of the human. Salah and Karey proposed a model using the fuzzy finite state machine method to experimentally find the predictive value of human reliability. In addition, the FO metric is updated by using the HR metric as;

$$FO = \frac{1}{RAD} HR \tag{2.13}$$

The Tr metric implies the trust of the human in the robot during HRI and is obtained experimentally by using fuzzy finite-state machine methods (Saleh and Karray, 2010). In addition, Salah and Karey proposed a new RAD metric alternative to Eq. 2.10. As mentioned above, the RAD metric measures the ratio of the time that the human interacts with the robot to the total time. The newly proposed RAD metric measures the total time of the human interacting directly with the robot (DIT) and the indirect interaction (IIT) due to human distrust of the robot for working. The new RAD is presented below.

$$RAD = DIT + IIT = DIT + NT(1 - Tr) \tag{2.14}$$

Another metric for the human part in HRI is the human effort (HE). In (Arnold and Lee, 2021), muscle activation for controlling a wearable ankle robot is measured by

using electromyography muscle sensors, and the HE is calculated by normalizing the total muscle activation. On the other hand, Bitz et al. (2020) used a different HE metric for the rehabilitation application. The root means square of the measured force applied by a human is used as HE metric. Moreover, the energy dissipation of human is measured for HE in (Zahedi et al., 2021).

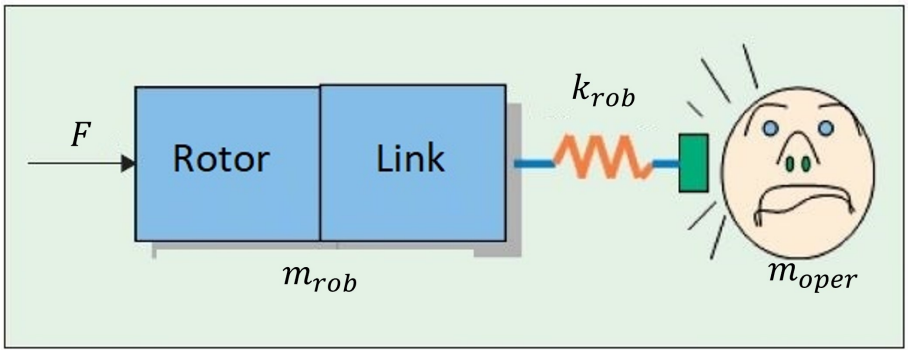

Figure 2.16. Simplified model of collision between human and one degree of freedom (DOF) robot arm (Source: Bicchi and Tonietti, 2004)

The main concern in human-robot interaction is safety. To not harm humans, it is necessary to limit the force that robots can apply. Versace (1971) proposed the HIC metric to measure injury risks and determine the injury limit tolerances for the human head due to impact forces. Bicchi and Tonietti (2004) combined the HIC metric with the equation of motion in their study and generalized the criterion in order to determine the risks of injury due to impact not only for the head but also for the other limbs. For using the one DOF robot arm shown in Fig 2.16, the HIC metric is designed as;

$$HIC = 2(\frac{2}{\pi})^{1.5}(\frac{k_{rob}}{m_{oper}})^{0.75}(\frac{m_{rob}}{m_{rob}+m_{oper}})^{1.75}v^{2.5} \tag{2.15}$$

$$HIC = \varpi(m_{rob}, m_{oper}, k_{rob})v^{2.5} \tag{2.16}$$

where m_{rob} and m_{oper} refer to the robot's total mass and the operator's mass. The robot's stiffness is shown as a spring k_{rob}. $\varpi(m_{rob}, m_{oper}, k_{rob})$ is a function of m_{rob}, m_{oper}, and k_{rob}. Another metric is derived from Eq. 2.16 to obtain the robot's speed for safe interaction with a human. It is calculated as follows;

$$v_{safe} = \frac{HIC_{max}}{\varpi(m_{rob}, m_{oper}, k_{rob})} \tag{2.17}$$

In addition to safety, performance is also a significant criterion for human-robot interaction. To measure the performance of the HRI, the accuracy and agility metrics

stand out. The accuracy metric measures the correctness of the completing work. In (Işıtman et al., 2018; Kanik et al., 2021), the operator was asked to interact with the robot and move the tip of the robot at a specific position. Then the operator was asked to hold the robot in this location for a while. The deflection between the desired position and the tip of the robot is scored inversely, and the accuracy metric is calculated by summing the score. Another performance metric is agility which is related to the speed of task execution. In (Arnold and Lee, 2021), the operator was asked to complete the tasks by cooperating with the robot, and the speed until completing the work was measured. By using maximum and average speed values, the agility was evaluated. Bitz et al. (2020) measured the rise time for motion performed by a human and a robot, and the value was used as an agility metric.

2.4. Preliminary Study - Surgical Workspace Study

The workspace studies for the NeuRoboScope were presented in (Maaroof, 2020) where experiments for measurement of the endoscope motion in pituitary gland surgery were done with the participation of two expert surgeons, Prof. Dr. M.D. Mustafa Berker and Assoc. Prof. Dr. M.D. Ahmet İlkay Isikay from Hacettepe University.

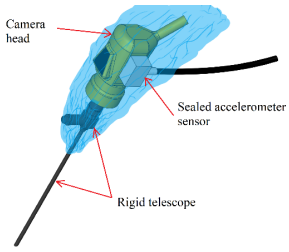

(a) Setup composed of an endoscope and angle measurement sensor

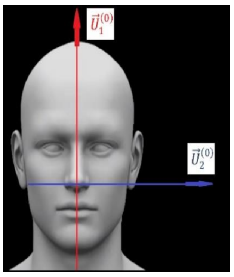

(b) The global reference frame with respect to the head of cadaver

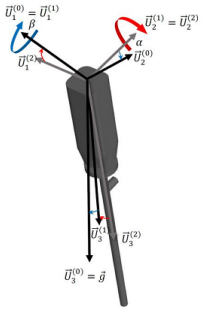

(c) The transformation between frames

Figure 2.17. The experimental setup and defined reference frames for the setup which used in workspace studies for the NeuRoboScope (Source: Maaroof, 2020)

For performing the experiments, a setup in Fig. 2.17a was designed by using an endoscope (constituted by TH100 IMAGE1 S™ H3- Z camera head and rigid telescope with a view angle of 30° by KARL STORZ) and a 3 - axis linear accelerometer. The

frames $\mathbf{F}_0$ & $\mathbf{F}_2$ attached to accelerometer and endoscope, respectively which are presented in 2.17c. The experiments are done by inserting the designed setup through the nasal cavity of a human and achieving the pituitary gland. From the results of the experiments, the maximum rotation angles around $\bar{U}_1^{(0)}$ and $\bar{U}_2^{(1)}$ were measured as 21° and 33° respectively. Moreover, the maximum angular speed was approximately measured as 55.5 $^\circ/\mathrm{s}$ $(= 0.9687\frac{rad.}{s})$ however, the surgeon rarely achieved this speed in the surgical application. For that reason, the speed data measured in the experimental scenario in which the endoscope was rotated around the nasal cavity by the surgeon were used in addition to the maximum measured speed. The maximum angular speed of this experiment was measured as 8 $^\circ/\mathrm{s}$, which is considered a trusted outcome for designing the controller. Also, the translational speed through the nasal cavity was derived as $18.5\frac{mm}{s}$.

2.5. Preliminary Study - Soft Tissue Modeling

In pituitary gland surgery, the medical instruments generally contact with soft tissues on the tip of the nose and nasal concha. Also, it is known that the medical instruments do not interact with any part of the brain during endoscopic pituitary gland surgery, although the location of the pituitary gland is closed to the brain. The soft tissues on the tip of the nose and nasal concha were modeled in (Işıtman et al., 2019) within the scope of the NeuRoboScope project.

Table 2.4. The RMSE torque values of analytical tissue models for tip of the nose (Source: Işıtman et al., 2019)

		Experiments: Tip of the Nose				
			RMSE (Nm)			
Models		Avg. Coeff.	#1	#2	#3	#4
Kelvin Boltzmann	k_2 k_1 b	0.972 0.233 23.631	**0.0216**	0.0165	**0.0062**	0.0111
Kelvin Voight	k b	0.205 0.341	0.0235	0.0156	**0.0062**	0.0108
Elastic	k	0.207	0.0237	0.0155	**0.0062**	0.0114
Maxwel	k b	1.129 120.233	0.0217	0.0135	0.0068	0.0099
Hunt Crossley	ϱ λ	0.280 15.328	0.0264	**0.0132**	0.0064	**0.0096**

To model the soft tissues, the simple, computationally fast, well-known methods are preferred: elastic, Kelvin-Voight, Maxwell, and Kelvin-Boltzmann as linear models (Misra et al., 2008; Liu et al., 2012) and Hunt-Crossley as a non-linear model (Pappalardo et al., 2016). In the elastic model, the relation between reaction force and deformation of tissue is modeled as spring. This relation is modeled as a combination of spring and damper components in other linear models, as seen in Fig.2.18. $F(t)$, $\dot{F}(t)$ and $x(t)$ refer to reaction force, derivative of $F(t)$ and deformation of tissue, respectively.

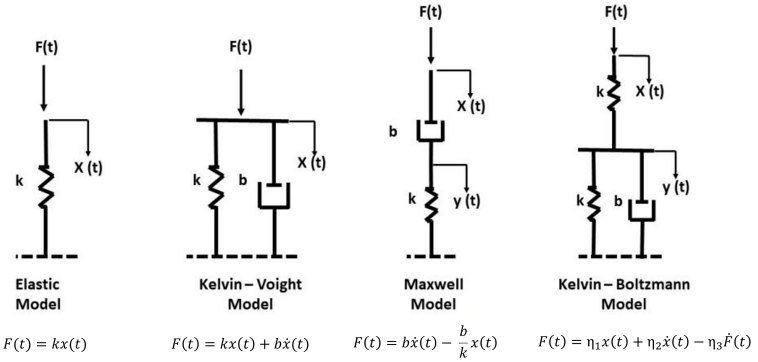

Figure 2.18. Generally used analytical linear tissue models (Source: Işıtman et al., 2019)

The gains of Kelvin-Boltzmans are $\eta_1 = \frac{k_1 k_2}{k1+k2}$, $\eta_2 = \frac{bk_2}{k1+k2}$ and $\eta_3 = \frac{b}{k1+k2}$ where k_1 and k_2 are spring constants and b is damper constant. Also, Hunt-Crossley model is shown as;

$$F(t) = \varrho x^{\wp}(t) + \lambda x^{\wp}(t)\dot{x}(t) \tag{2.18}$$

where ϱ and λ are coefficients and $\wp$ is a scalar between 1.1 to 1.3 which is chosen as 1.2 in the study.

For modeling the tissues encountered in pituitary gland surgery, such as nose tip and nasal concha, Işıtman et al. (2019) proposed a mobile measurement device, which allowed a user to measure the reaction moments and angular deformation of tissues. A freshly frozen cadaver head was prepared, and it started to be thawed 48 hours before starting the experiments. By using them, the moment and angular deformation values of tissues were measured. Four experiments for the tip of the nose and five experiments for the nasal concha were done. For each experiment, the parameters of models were identified, and it is observed that the obtained parameters of each experiment are close to each other. For this reason, the average of the parameters was calculated and used in the models. Their performance was evaluated using RMSE (root mean square error) values between measured reaction torques and obtained torques from the analytical tissue

Table 2.5. The RMSE torque values of analytical tissue models for the nasal concha (Source: Işıtman et al., 2019)

		Experiments: Nasal Concha					
			RMSE (Nm)				
Models		Avg. Coeff.	#1	#2	#3	#4	#5
Kelvin Boltzmann	k_2 k_1 b	3.303 0.479 30.456	**0.0157**	0.0085	0.0128	**0.0055**	0.0080
Kelvin Voight	k b	0.574 0.957	0.0198	0.0114	0.0106	0.0064	0.0072
Elastic	k	0.589	0.0206	0.0110	**0.0104**	0.0066	0.0068
Maxwel	k b	3.476 137.860	0.0334	0.0111	0.0107	0.0083	0.0098
Hunt Crossley	ϱ λ	1.054 15.158	0.0237	**0.0050**	0.0117	0.0068	**0.0048**

models. By that way, the results are presented in Table. 2.4 and 2.5 where the best solution is presented as bold and according to results, worst performances are shown by Maxwell when modeling the tip of the nose and Kelvin-Voight when the nasal concha is modeled. In addition, the elastic model shows the best solution in the third experiment for both tissues. Obviously, the Kelvin - Boltzmann, and Hunt-Crossley have the best performance for modeling the tissues.

Within the scope of the same study, Işıtman (2018) stated that the maximum forces and moments for the tissues were measured as $\approx 2N$ and $\approx 0.3Nm$ and the values by multiplying the safety factor were used in the design of the NeuRoboScope.

CHAPTER 3

MATHEMATICAL MODELING OF THE NEUROBOSCOPE

The NeuRoboScope robot consists of two parts labeled as active and passive. The active part of the robot is a parallel manipulator (PM) with a remote center of motion (RCM) mechanism that restricts the robot's motion around or through a point which is called a pivot point in this dissertation. The kinematic structure of the active part is selected as 2URRR-URR. The robot aims to carry and move the endoscope according to the surgeon's commands. This chapter presents the derivation of the direct kinematics, inverse kinematics, and the Jacobian matrix of the active part. Reader can find more details in the derivation of the kinematics in (Yaşır et al., 2020).

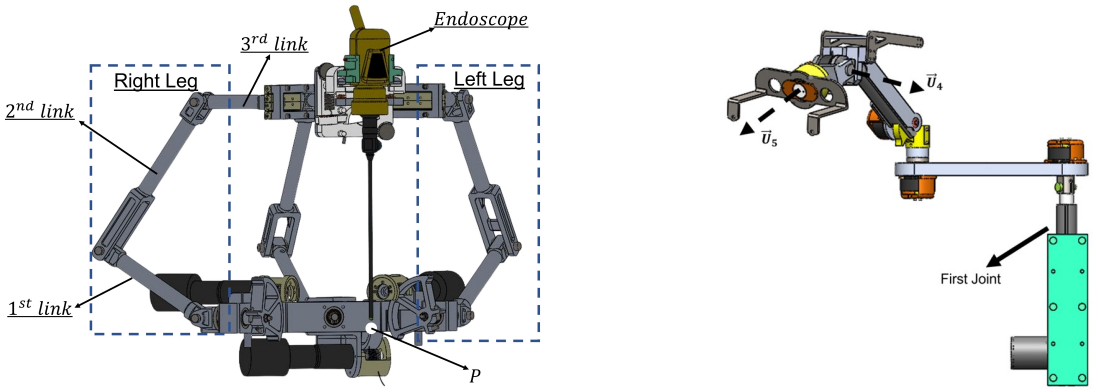

(a) Active Part (b) Passive Part

Figure 3.1. The active part of the NeuRoboScope is presented at the left of the image, where p refers to the pivot point. The passive part of the NeuRoboScope is presented on the right of the image, and the axis of the joints responsible for the passive robot's orientation is shown.

The passive part of the NeuRoboScope is a serial PRRRRR manipulator whose end-effector is connected to the active part's base. The passive part carries and sets the initial location of the active part in the operation area. It is constituted by five revolute joints and a prismatic joint. A prismatic actuator actuates the first joint to regulate the altitude of the active part's base with respect to the operating table at the beginning of the surgery. Each revolute joint contains the brakes. The manipulator is backdrivable and

statically balanced when the brakes are off-states. Moreover, the angular position sensors are attached to each joint to calculate the position and orientation of the base of the active part. The orientation data of the tip of the passive part is only used in the control studies, and this data is calculated by measuring the rotation angles around $\vec{U}_4$ and $\vec{U}_5$. Moreover, the rotation around $\vec{U}_4$ provides the active part to reach the entire workspace, while the rotation around $\vec{U}_5$ brings the ergonomic usage to the surgeon. This allows for neglecting the rotation around $\vec{U}_5$ for simplification. Also, the derivation of the complete kinematic equation of the passive part is not presented in this dissertation since the rotation angle around $\vec{U}_4$ is sufficient to be used in the design of the control algorithms.

3.1. Kinematics of the NeuRoboScope

The active part is a three DOF PM constituted by URRR sides legs and a URR middle leg as seen in Fig. 3.2.

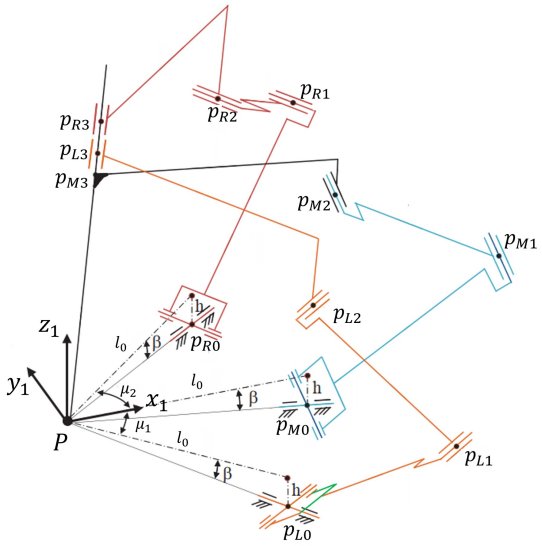

Figure 3.2. Kinematic diagram of the active part (Source: Yaşır, 2018)

The kinematic diagram is simplified in Fig. 3.3 using a plane defined by $\overrightarrow{PP_{L0}}$ and $\overrightarrow{PP_{L3}}$, a plane defined by $\overrightarrow{PP_{R0}}$ and $\overrightarrow{PP_{R3}}$ and a plane defined by $\overrightarrow{PP_{M0}}$ and $\overrightarrow{PP_{M3}}$. These planes are intersected in a vector $\vec{W}$ that implies the endoscope. As mentioned in Yaşır (2018), the motion of the robot in task space is defined as ϕ that represents an angle of $\vec{W}$ with respect to the x_1z_1 plane (corresponding to the yaw motion) and ψ that represents an angle of $\vec{W}$ with respect to the y_1z_1 plane (corresponding to the pitch motion) and a translation position d through $\vec{W}$.

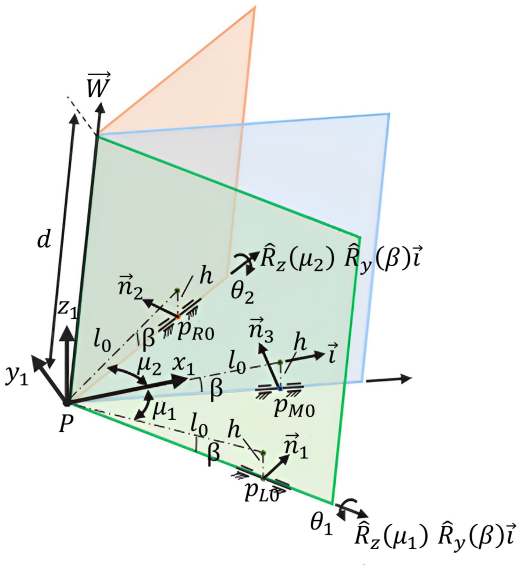

Figure 3.3. Simplified kinematic diagram of the active part (Source: Yaşır, 2018)

To obtain best force transmission characteristic of the robot, μ_1, μ_2 and β are chosen as $45°$, $-45°$, and $0°$ respectively. l_0 is selected as $200\ mm$.

The direct kinematic, inverse kinematic and Jacobian matrix of the manipulator are derived in (Yaşır, 2018) where generalized coordinates in task space are ϕ, ψ, and d and generalized coordinates in joint space are θ_1, θ_2 and θ_3. Firstly, the $\vec{n}_1$ and $\vec{n}_2$ are calculated from Fig. 3.3 and these are represented below in column matrix resolved in Frame $\mathbf{F}_1$, defined in Fig. 3.5.

$$\bar{n}_1 = \begin{bmatrix} c(\frac{\pi}{4}) & -s(\frac{\pi}{4}) & 0 \\ s(\frac{\pi}{4}) & c(\frac{\pi}{4}) & 0 \\ 0 & 0 & 1 \end{bmatrix} \begin{bmatrix} 1 & 0 & 0 \\ 0 & c(\theta_1) & -s(\theta_1) \\ 0 & s(\theta_1) & c(\theta_1) \end{bmatrix} \begin{bmatrix} 0 \\ 1 \\ 0 \end{bmatrix} = \begin{bmatrix} -c(\theta_1)/\sqrt{2} \\ c(\theta_1)/\sqrt{2} \\ s(\theta_1) \end{bmatrix} \tag{3.1}$$

where c and s are abbreviations for cosine and sine, respectively.

$$\bar{n}_2 = \begin{bmatrix} c(-\frac{\pi}{4}) & -s(-\frac{\pi}{4}) & 0 \\ s(-\frac{\pi}{4}) & c(-\frac{\pi}{4}) & 0 \\ 0 & 0 & 1 \end{bmatrix} \begin{bmatrix} 1 & 0 & 0 \\ 0 & c(\theta_2) & -s(\theta_2) \\ 0 & s(\theta_2) & c(\theta_2) \end{bmatrix} \begin{bmatrix} 0 \\ 1 \\ 0 \end{bmatrix} = \begin{bmatrix} c(\theta_2)/\sqrt{2} \\ c(\theta_2)/\sqrt{2} \\ s(\theta_2) \end{bmatrix} \tag{3.2}$$

The unit vector $\vec{W}$ is derived by using geometry and it is represented below in column matrix resolved in Frame $\mathbf{F}_1$.

$$\bar{W} = \begin{bmatrix} s(\psi) \\ -s(\phi) \\ \sqrt{1 - s(\psi)^2 - s(\phi)^2} \end{bmatrix} \tag{3.3}$$

$\vec{W}$ is also derived by using $\vec{n}_1$ and $\vec{n}_2$;

$$\vec{W} = \frac{\vec{n}_1 \times \vec{n}_2}{|\vec{n}_1 \times \vec{n}_2|} \tag{3.4}$$

From Eq. 3.3 & 3.4, ϕ and ψ are calculated as follows;

$$\phi = \text{asin}\left(\frac{s(\theta_2 + \theta_1)}{\sqrt{2}|\vec{n_1} \times \vec{n_2}|} \right) \tag{3.5}$$

$$\psi = \text{asin}\left(\frac{s(\theta_2 - \theta_1)}{\sqrt{2}|\vec{n_1} \times \vec{n_2}|} \right) \tag{3.6}$$

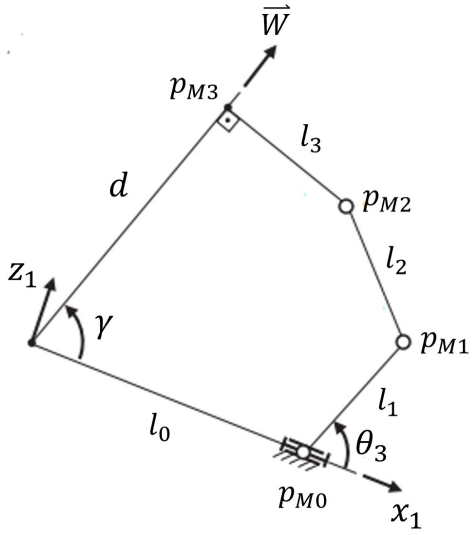

Figure 3.4. A view of plane defined by x_1 and $\vec{W}$

By solving the kinematics of the slider-crank mechanism in Fig. 3.4, the d is derived as;

$$d = l_0 c(\gamma) + l_1 c(\theta_3 - \gamma) + \sqrt{l_2^2 - (l_3 - l_0 s(\gamma) + l_1 s(\theta_3 - \gamma))^2} \tag{3.7}$$

where $\gamma = \frac{\pi}{2} - \psi$.

Therefore, the direct kinematics equations are obtained as presented in Eq. 3.5 to 3.7.

By using the relations $\vec{W}.\vec{n}_1 = 0$ and $\vec{W}.\vec{n}_2 = 0$ where $\vec{W}$ is orthogonal to $\vec{n}_1$ and $\vec{n}_2$, the inverse kinematic equations are calculated as follows;

$$\theta_1 = \operatorname{atan}\left(\frac{s(\phi)c(\frac{\pi}{4}) - s(\psi)s(\frac{\pi}{4})}{\sqrt{1 - s(\psi)^2 - s(\phi)^2}}\right) \tag{3.8}$$

$$\theta_2 = \operatorname{atan}\left(\frac{s(\phi)c(\frac{\pi}{4}) + s(\psi)s(\frac{\pi}{4})}{\sqrt{1 - s(\psi)^2 - s(\phi)^2}}\right) \tag{3.9}$$

θ_3 is found by inverse kinematic of the slider-crank mechanism in Fig. 3.4.

$$\theta_3 = \operatorname{atan}2(\Lambda, \chi) - \operatorname{acos}\left(\frac{\Upsilon}{\mho}\right) \tag{3.10}$$

where $\Lambda = 2l_1(dc(\gamma) + l_3 s(\gamma) - l_0)$, $\chi = 2l_1(ds(\gamma) - l_3 c(\gamma))$, $\mho = \sqrt{\Lambda^2 + \chi^2}$, $\Upsilon = (dc(\gamma) + l_3 s(\gamma) - l_0)^2 + (ds(\gamma) - l_3 c(\gamma))^2 + l_1^2 - l_2^2$.

Also, the velocity relation between joint and task space variables is obtained by using the equations below.

$$f_1(\theta_1, \theta_2, \phi, \psi) = \sqrt{1 - s(\psi)^2 - s(\phi)^2}\, s(\theta_2 - \theta_1) - \sqrt{2} s(\psi) c(\theta_1) c(\theta_2) = 0 \tag{3.11}$$

$$f_2(\theta_1, \theta_2, \phi, \psi) = \sqrt{1 - s(\psi)^2 - s(\phi)^2}\, s(\theta_2 + \theta_1) - \sqrt{2} s(\phi) c(\theta_1) c(\theta_2) = 0 \tag{3.12}$$

$$f_3(d, \phi, \psi, \theta_3) = d^2 - f_{3a} + f_{3b} + f_{3c} - l_2^2 = 0 \tag{3.13}$$

where $f_{3a} = 2d(l_0 c(\gamma) + l_1 c(\theta_3 - \gamma))$, $f_{3b} = (l_0 c(\gamma) + l_1 c(\theta_3 - \gamma))^2$, and $f_{3c} = (l_3 - l_0 s(\gamma) + l_1 s(\theta_3 - \gamma))^2$.

$$\begin{bmatrix} \dot{\phi} \\ \dot{\psi} \\ \dot{d} \end{bmatrix} = \hat{J}_n \begin{bmatrix} \dot{\theta}_1 \\ \dot{\theta}_2 \\ \dot{\theta}_3 \end{bmatrix}, \tag{3.14}$$

where $\hat{J}_n = \begin{bmatrix} -\frac{\delta f_1}{\delta \phi} & -\frac{\delta f_1}{\delta \psi} & 0 \\ -\frac{\delta f_2}{\delta \phi} & -\frac{\delta f_2}{\delta \psi} & 0 \\ -\frac{\delta f_3}{\delta \phi} & -\frac{\delta f_3}{\delta \psi} & -\frac{\delta f_3}{\delta d} \end{bmatrix}^{-1} \begin{bmatrix} \frac{\delta f_1}{\delta \theta_1} & \frac{\delta f_1}{\delta \theta_2} & 0 \\ \frac{\delta f_2}{\delta \theta_1} & \frac{\delta f_2}{\delta \theta_2} & 0 \\ 0 & 0 & \frac{\delta f_3}{\delta \theta_3} \end{bmatrix}$

The first joint of the passive part moves along z_0-direction in Fig. 3.5 where the frames $\mathbf{F}_0$, $\mathbf{F}_1$, and $\mathbf{F}_2$ are defined. $\mathbf{F}_0$ is a fixed frame attached to the base of the passive

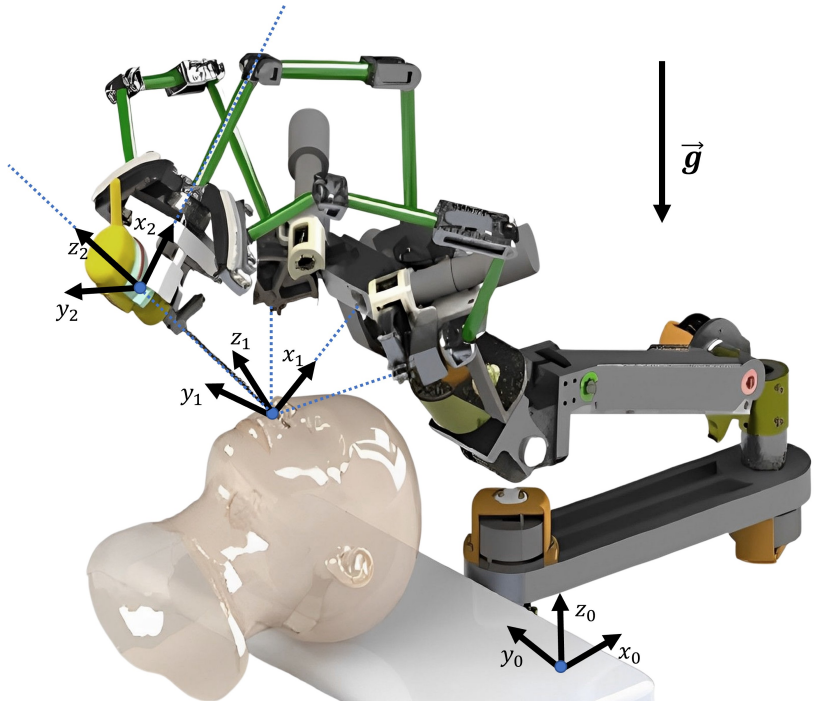

Figure 3.5. Defined coordinate frames of the NeuRoboScope

system. Frame $\mathbf{F}_1$ is attached to the active system's base that is coincident with the end-effector of the passive system. Frame $\mathbf{F}_2$ is attached to the endoscope, located at the end-effector of the active part. The rotation between $\mathbf{F}_1$ to $\mathbf{F}_2$ is defined as below where $\mathbf{F}_a$ is an arbitrary frame. $\vec{U}_x^{(1)}$ refers to unit vector along x_1 defined in $\mathbf{F}_1$ and $\vec{U}_y^{(1)}$ refers to unit vector along y_1 defined in $\mathbf{F}_1$. Also, y_a is coincident with y_2. θ_x and θ_y are rotation angles. The rotation matrix with respect to fixed frame $\mathbf{F}_1$ is obtained as $\hat{R}_1^2 = \hat{R}_x(\theta_x)\hat{R}_y(\theta_y)$. $\hat{R}_x$ and $\hat{R}_y$ are rotation matrices for x axis and y axis, respectively.

$$\mathbf{F_1} \xrightarrow[\theta_x]{\vec{U}_x^{(1)}} \mathbf{F_a} \xrightarrow[\theta_y]{\vec{U}_y^{(1)}} \mathbf{F_2}$$

In Eq. 2.1, $\bar{W}^{(1)}$ and $\bar{W}^{(2)}$ are defined in $\mathbf{F}_1$ and $\mathbf{F}_2$, respectively. $\bar{W}^2 = \begin{bmatrix} 0 & 0 & 1 \end{bmatrix}^T$ therefore, the relation is obtained as

$$\bar{W}^{(1)} = \hat{R}_2^1 \bar{W}^{(2)} \tag{3.15}$$

where $\bar{W}$ refers to matrix form of $\vec{W}$. By using the Eq. 3.3 & 3.15 , the angles θ_x and θ_y is derived from angles ϕ and ψ;

$$\theta_x = \phi \tag{3.16a}$$

$$\theta_y = \text{asin}\left(\frac{s(\psi)}{c(\phi)}\right) \tag{3.16b}$$

By taking the derivative of Eq. 3.16, the relation in velocity level is obtained:

$$\begin{bmatrix} \dot{\theta}_x \\ \dot{\theta}_y \\ \dot{d} \end{bmatrix} = \hat{J}_{xy} \begin{bmatrix} \dot{\phi} \\ \dot{\psi} \\ \dot{d} \end{bmatrix} \tag{3.17}$$

where $\hat{J}_{xy} = \begin{bmatrix} \frac{\sin(\phi)\sin(\psi)}{\cos(\phi)^2\sqrt{1-(\frac{sin(\psi)}{cos(\phi)})^2}} & \frac{\cos(\psi)}{\cos(\phi)\sqrt{1-(\frac{sin(\psi)}{cos(\phi)})^2}} & 0 \\ 0 & 1 & 0 \\ 0 & 0 & 1 \end{bmatrix}$ and $\hat{J} = \hat{J}_{xy}\hat{J}_n$.

The Jacobian matrix $\hat{J}$ and rotation matrices $\hat{R}_1^2$ have a significant role in the calculation of the dynamics of the robot.

3.2. Dynamic Modeling of the NeuRoboScope

The active part's dynamic model is derived using the recursive Newton-Euler approach, which has relatively low computational complexity. The orientation of the passive manipulator only affects the rotation of the gravitational acceleration in the dynamics. The rigid body dynamic model can be described as;

$$\bar{T} = \hat{M}(\bar{q}_a)\ddot{\bar{q}}_a + \hat{V}_m(\bar{q}_a, \dot{\bar{q}}_a)\dot{\bar{q}}_a + \bar{G}(\bar{q}_a) + \hat{F}_v\dot{\bar{q}}_a + \hat{F}_d sgn(\dot{\bar{q}}_a) + \bar{T}_d \tag{3.18}$$

where $\hat{M}(\bar{q}_a) \in \hat{\mathbb{R}}^{3\times3}$, $\hat{V}_m(\bar{q}_a, \dot{\bar{q}}_a) \in \hat{\mathbb{R}}^{3\times3}$, $\bar{G}(\bar{q}_a) \in \bar{\mathbb{R}}^3$, $\hat{F}_v \in \hat{\mathbb{R}}^{3\times3}$ refer to mass matrix, Coriolis and centrifugal matrix, gravitational torque vector, and viscous friction coefficient matrix. The external disturbance torque vector $\bar{T}_d \in \bar{\mathbb{R}}^3$ is assumed to be bounded in the $\infty-$norm. $\bar{q}_a$ refers to the generalized coordinate and $\bar{q}_a = \begin{bmatrix} \dot{\theta}_1 & \dot{\theta}_2 & \dot{\theta}_3 \end{bmatrix}^T$.

According to the recursive Newton-Euler approach, the links' velocity and acceleration of the center of mass (CoM) are calculated.

For prismatic joints;

$$\vec{w}_{\text{i}}^{(\text{i})} = \vec{w}_{\text{i}-1}^{(\text{i})} \tag{3.19}$$

$$\vec{v}_{\text{i}}^{(\text{i})} = \vec{v}_{\text{i}-1}^{(\text{i})} + \vec{w}_{\text{i}-1}^{(\text{i})} \times \vec{r}_{\text{i}}^{(\text{i})} + \dot{\vec{q}}_{\text{i}}^{(\text{i})}\vec{U}_{\text{i}}^{(\text{i})} \tag{3.20}$$

$$\vec{\alpha}_{\text{i}}^{(\text{i})} = \vec{\alpha}_{\text{i}-1}^{(\text{i})} \tag{3.21}$$

$$\vec{a}_{\mathrm{i}}^{(\mathrm{i})} = \vec{a}_{\mathrm{i-1}}^{(\mathrm{i})} + \vec{\alpha}_{\mathrm{i-1}}^{(\mathrm{i})} \times \vec{r}_{\mathrm{i}}^{(\mathrm{i})} + \ddot{\vec{q}}_{\mathrm{i}}^{(\mathrm{i})} \vec{U}_{\mathrm{i}}^{(\mathrm{i})} + \vec{w}_{\mathrm{i-1}}^{(\mathrm{i})} \times (\vec{w}_{\mathrm{i-1}}^{(\mathrm{i})} \times \vec{r}_{\mathrm{i}}^{(\mathrm{i})}) + 2\vec{w}_{\mathrm{i-1}}^{(\mathrm{i})} \times \dot{\vec{q}}_{\mathrm{i}}^{(\mathrm{i})} \vec{U}_{\mathrm{i}}^{(\mathrm{i})} \quad (3.22)$$

For revolute joints;

$$\vec{w}_{\mathrm{i}}^{(\mathrm{i})} = \vec{w}_{\mathrm{i-1}}^{(\mathrm{i})} + \dot{\vec{q}}_{\mathrm{i}}^{(\mathrm{i})} \vec{u}_{\mathrm{i}}^{(\mathrm{i})} \quad (3.23)$$

$$\vec{v}_{\mathrm{i}}^{(\mathrm{i})} = \vec{v}_{\mathrm{i-1}}^{(\mathrm{i})} + \vec{w}_{\mathrm{i-1}}^{(\mathrm{i})} \times \vec{r}_{\mathrm{i}}^{(\mathrm{i})} + \dot{\vec{q}}_{\mathrm{i}}^{(\mathrm{i})} \vec{U}_{\mathrm{i}}^{(\mathrm{i})} \times \vec{\ell}_{\mathrm{i}}^{(\mathrm{i})} \quad (3.24)$$

$$\vec{\alpha}_{\mathrm{i}}^{(\mathrm{i})} = \vec{\alpha}_{\mathrm{i-1}}^{(\mathrm{i})} + \dot{\vec{q}}_{\mathrm{i}}^{(\mathrm{i})} \vec{U}_{\mathrm{i}}^{(\mathrm{i})} + \vec{w}_{\mathrm{i-1}}^{(\mathrm{i})} \times \dot{\vec{q}}_{\mathrm{i}}^{(\mathrm{i})} \vec{U}_{\mathrm{i}}^{(\mathrm{i})} \quad (3.25)$$

$$\vec{a}_{\mathrm{i}}^{(\mathrm{i})} = \vec{a}_{\mathrm{i-1}}^{(\mathrm{i})} + \vec{\alpha}_{\mathrm{i-1}}^{(\mathrm{i})} \times \vec{r}_{\mathrm{i}}^{(\mathrm{i})} + \ddot{\vec{q}}_{\mathrm{i}}^{(\mathrm{i})} \vec{U}_{\mathrm{i}}^{(\mathrm{i})} \times \vec{\ell}_{\mathrm{i}}^{(\mathrm{i})} + (\dot{\vec{q}}_{\mathrm{i}}^{(\mathrm{i})} \vec{U}_{\mathrm{i}}^{(\mathrm{i})} \times \vec{\ell}_{\mathrm{i}}^{(\mathrm{i})}) + a_{ic} \quad (3.26)$$

where $a_{ic} = 2\vec{w}_{\mathrm{i-1}}^{(\mathrm{i})} \times (\dot{\vec{q}}_{\mathrm{i}}^{(\mathrm{i})} \vec{U}_{\mathrm{i}}^{(\mathrm{i})} \times \vec{\ell}_{\mathrm{i}}^{(\mathrm{i})}) + \vec{w}_{\mathrm{i-1}}^{(\mathrm{i})} \times (\vec{w}_{\mathrm{i-1}}^{(\mathrm{i})} \times \vec{r}_{\mathrm{i}}^{(\mathrm{i})})$

- $\vec{(.)}_{\mathrm{n}}^{\mathrm{m}}$ means that a vector, defined in mth frame, belongs the nth link.
- $\vec{U}_{\mathrm{i}}$: A unit vector is defined as ith joint axis.
- $\vec{w}_{\mathrm{i}}$: A angular velocity vector of the center of mass of the ith links.
- $\vec{v}_{\mathrm{i}}$: A linear velocity vector of the center of mass of the ith links.
- $\vec{\alpha}_{\mathrm{i}}$: A angular acceleration vector of the center of mass of the ith links.
- $\vec{a}_{\mathrm{i}}$: A linear acceleration vector of the center of mass of the ith links.
- $\vec{\ell}_{\mathrm{i}}$: A vector is defined from the ith joint to the center of mass of the ith links.
- $\vec{r}_{\mathrm{i}}$: A vector is defined from the center of mass of the i $-$ 1th links to center of mass of the ith links.

The calculation of velocity and acceleration of links is initially started with the link which is connected to the base of the robot. Then the inner links' motion is calculated by using previous links' computed velocity and acceleration data. In contrast, the force and torque of the robot's end-effector is firstly calculated, then the applied force/torque on CoM of inner links and joints are calculated recursively. The free-body diagram of the inner link of serial linkage and the tree-linkage handle are shown in Fig. 3.6.

In Fig. 3.6a, the inner link of the serial linkage is labeled as link i-1, which is connected with the outboard and inboard joint. $F_{\mathrm{i-1}}^{O}$ and $T_{\mathrm{i-1}}^{O}$ refers to force and torque applied through outboard joint, in addition $F_{\mathrm{i-1}}^{I}$ and $T_{\mathrm{i-1}}^{I}$ are force and torque applied through inboard joint. $\vec{g}$ refers to the gravity vector. By using the Newton-Euler method, the equation of motion is obtained as;

$$\bar{F}_{\mathrm{i-1}}^{I} + \bar{F}_{\mathrm{i-1}}^{O} = \hat{M}_{\mathrm{i-1}} \bar{a}_{\mathrm{i-1}} - m_{i-1} \bar{g} \quad (3.27a)$$

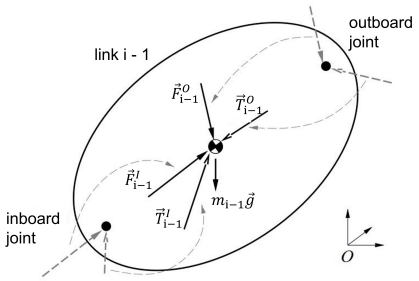

(a) The free-body diagram of inner link of serial linkage

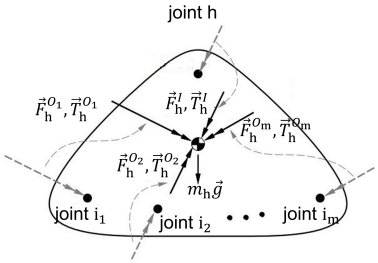

(b) The free-body diagram of inner link of tree linkage

Figure 3.6. The free-body diagram of links of parallel manipulator (Source: Mirtich, 1996)

.

$$\bar{T}^{I}_{i-1} + \bar{T}^{O}_{i-1} = \hat{I}_{i-1}\bar{\alpha}_{i-1} + \tilde{w}_{i-1}\hat{I}_{i-1}\bar{w}_{i-1} \tag{3.27b}$$

where

- $\tilde{w}_{i-1}$ is skew symmetric matrix of $\bar{w}_{i-1}$,
- $\bar{w}_{i-1}$, $\bar{a}_{i-1}$, and $\bar{\alpha}_{i-1}$ refers to the matrix form of $\vec{w}^{(i-1)}_{i-1}$, $\vec{a}^{(i-1)}_{i-1}$, and $\vec{\alpha}^{(i-1)}_{i-1}$ respectively,
- $\hat{M}_{i-1}$ refers to mass matrix of the link $i-1$ and $\hat{M} = m_{i-1}\hat{1}$ where m_{i-1} is mass of the link $i-1$,
- $\hat{I}_{i-1}$ refers to inertia matrix of link,
- $\bar{F}^{O}_{i-1}$ = -$\bar{F}^{I}_{i}$.

In Fig. 3.6b, the end-effector of a parallel robot is labeled as link h, which is connected to m outboard joints and an inboard joint, labeled as joint h. The equation of motion for the end-effector of the robot is obtained as follows;

$$\bar{F}^{I}_{h} + \sum_{j=1}^{m} \bar{f}^{O_j}_{h} = \hat{M}_h\bar{a}_h - m_h\bar{g} \tag{3.28a}$$

$$\bar{T}^{I}_{h} + \sum_{j=1}^{m} \bar{T}^{O_j}_{h} = \hat{I}_h\bar{\alpha}_h + \tilde{w}_h\hat{I}_h\bar{w}_h \tag{3.28b}$$

For the NeuRoboScope robot, the robot's dynamic model is calculated by using the above equations, and the results are verified using the Simscape Multibody Matlab/Simulink. For the simulation study, the trajectory obtained from the workspace studies of the NeuRoboScope is used, and the trajectory is shown in Fig. 3.7. The results

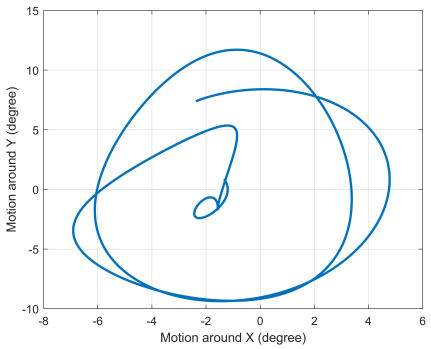

(a) The angle trajectory around $x^{(1)}$ and $y^{(1)}$ axis

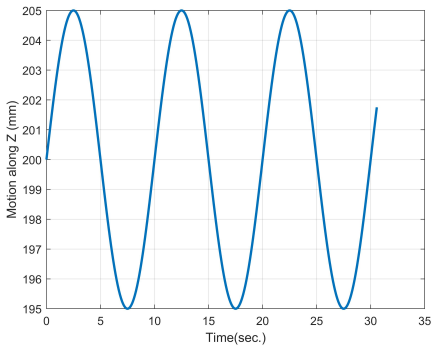

(b) The motion trajectory along $z^{(2)}$ axis

Figure 3.7. The motion trajectory for simulations

are derived by calculating the difference between the torques obtained from the Simscape Multibody model and the analytical dynamic model. The error is divided by torques from the Simscape Multibody model and multiplied by 100. The results are 0.0014%, 0.0018% and $2.6251 \times 10^{-5}\%$ for T_1, T_2 and T_3 respectively which show the correctness of the derived dynamic model of the NeuRoboScope.

Table 3.1. The inertial parameters of the NeuRoboScope

Leg	Links	Link Length (mm)	Location of CoM (mm)	Mass (gr)
Left	1^{st}	135	75.6	73.3
	2^{nd}	195	107.4	115.8
	3^{rd}	200	65.6	111.3
Right	1^{st}	135	75.8	74.3
	2^{nd}	195	107.2	116.1
	3^{rd}	200	75.4	112.1
Middle	1^{st}	135	44.82	159.7
	2^{nd}	195	111.5	93.6
	3^{rd}	200	114.2	361.9
Mobile platform		250	36.7	797.2

In Table 3.1, mobile platform contains the telescope, endoscope, endoscope holder, and F/T sensor and the mobile platform's mass refers to total mass of these components. Location of CoM refers to distance between the CoM of links and its joint.

3.3. Simplified Dynamic Modeling of the NeuRoboScope

In the NeuRoboScope system, an ARM Cortex M4 processor is used as the main computer, which has high performance on the robotic application with lower power consumption and cost-efficiency. To enforce the robot tracks the desired trajectory, the system's main computer runs the position controller with the desired high frequency. In this application, the computed torque method is designed as a position controller, which requires the dynamic model of the robot. However, the processor cannot run the derived dynamic equation at the desired high frequencies. To deal with this issue, the effects of the inertia, Coriolis and centrifugal and gravitational forces on the dynamic of the NeuRoboScope are analyzed. To use in this analysis, the maximum angular and translational speed of the end-effector of the robot are derived as $0.9687\frac{rad.}{s}$ and $18.5\frac{mm}{s}$ from the workspace studies in Section 2.4, respectively. Then, the maximum angular and translational accelerations are obtained as $3.5840\frac{rad.}{s^2}$ and $68.4500\frac{mm}{s^2}$. By using the Jacobian matrices in Eq. 3.14 and 3.17, the maximum velocity and acceleration values are obtained as $2.0094\frac{rad.}{s}$ and $7.4172\frac{rad.}{s^2}$ in joint space. In Fig. 3.8, the percentage value of the inertia, Coriolis and centrifugal and gravitational torques of the total torques T_1, T_2 and T_3 are calculated when angle ϕ and ψ increased from -14° to 14° and -19° to 19° by 1°, respectively and d is kept constant at $150\ mm$, $200\ mm$ and $240\ mm$. When the average of the percentages is calculated, it is observed that the gravitational torques, Coriolis and centrifugal torques, and torques due to inertia have 75.5%, 11.5% and 13% of total torques respectively. According to this analysis, it is observed that gravitational torques have a much higher impact on the dynamics of the robot than other terms. Also, the terms based on velocity and acceleration have the approximately same effect on the dynamic of the NeuRoboScope. Due to the inference of the analysis and the workspace studies, it is assumed that maximum velocity will not be reached during the surgical operation; therefore, the Coriolis and centrifugal torques can be neglected. Moreover, It is observed that the mobile platform's mass dominates the robot's mass compared to the other links of the robot in Table 3.1. Therefore, the assumptions below are made to simplify the dynamic model of the NeuRoboScope.

- The links and joints of the manipulator are rigid.
- The frictions are neglected due to relatively high reduction ratio $(1 : 905)$ in the NeuRoboScope's actuation system.
- Masses of the links of the legs and all actuators are neglected except the mobile

platform's mass.

- Moment of inertia values of the right, left and middle links and actuators attached to right and left links are neglected.
- Coriolis and centrifigual terms in the rigid body dynamics are neglected.

According to these assumptions, the joint space rigid body dynamic model is derived in Eq. 3.29 where $\bar{T}$, $\hat{M}_s$ and $\bar{G}_s$ are defined as generalized torque column matrix, simplified mass matrix and simplified gravitational torque column matrix, respectively.

$$\bar{T} = \hat{M}_s(\bar{q}_a)\ddot{\bar{q}}_a + \bar{G}_s(\bar{q}_a) \tag{3.29}$$

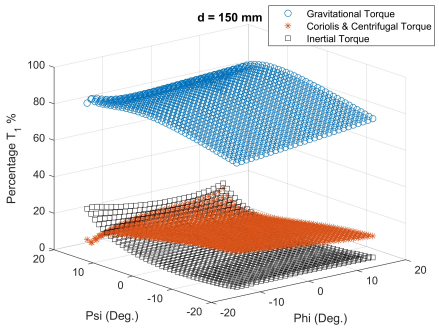

(a) Percentage of T_1, $d = 150$

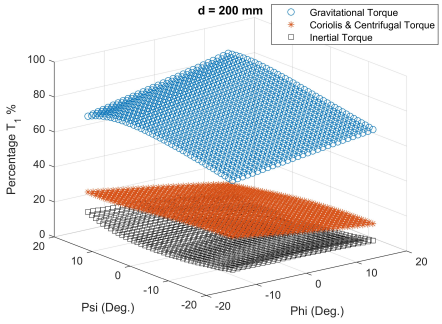

(b) Percentage of T_2, $d = 150$

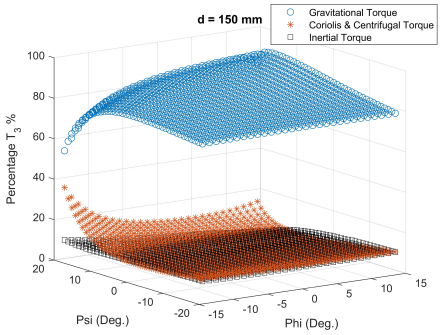

(c) Percentage of T_2, $d = 150$

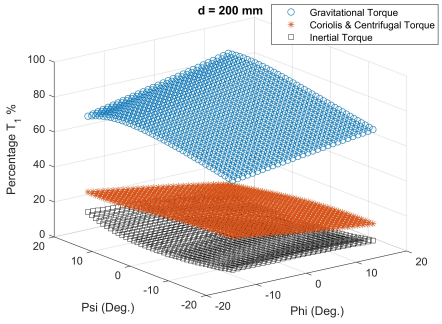

(d) Percentage of T_1, $d = 200$

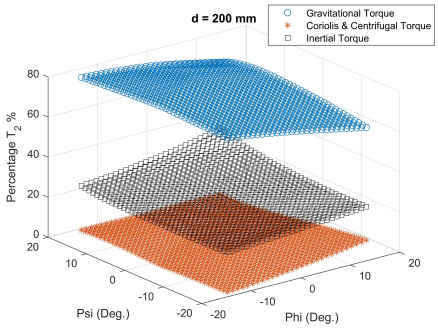

(e) Percentage of T_2, $d = 200$

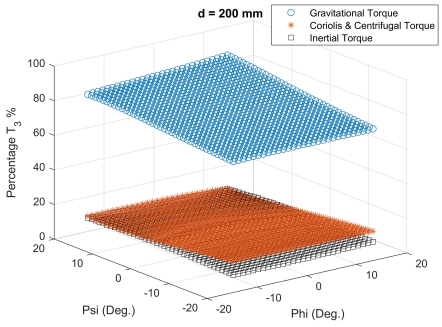

(f) Percentage of T_3, $d = 200$

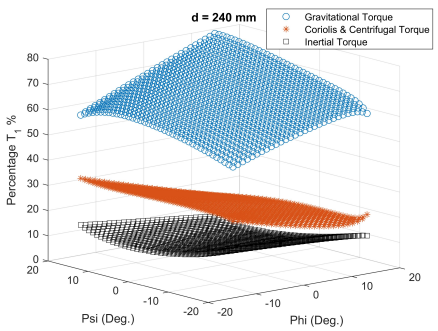

(g) Percentage of T_1, $d = 240$

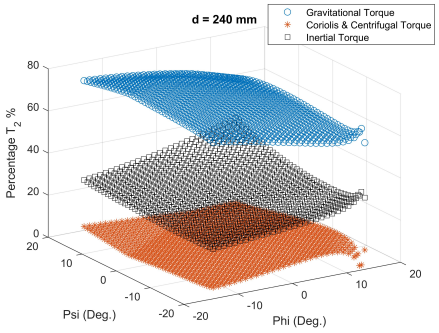

(h) Percentage of T_2, $d = 240$

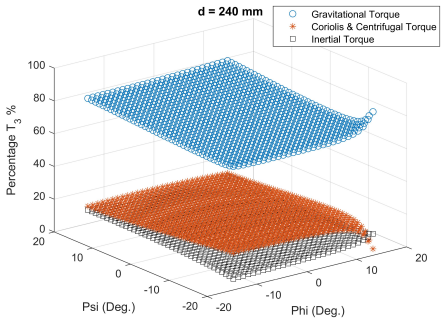

(i) Percentage of T_3, $d = 240$

Figure 3.8. The percentage value of the inertial, Coriolis and centrifugal and gravitational torques of the total torques T_1, T_2 and T_3 when $d = 150, 200, 240$

3.3.1. Calculation of the Simplified Inertia Matrix

Eq. 3.30 represents the kinetic equation forumula where KE refers to kinetic energy and describes the relation between kinetic energy and mass matrix.

$$KE = \frac{1}{2}\dot{\bar{q}}_a^T \hat{M}_s \dot{\bar{q}}_a \tag{3.30}$$

According to the mentioned assumptions, the kinetic energy of the robot depends on the angular and linear velocity of the mobile platform and the angular velocity of an actuator located at the bottom of the middle leg. This actuator's linear and angular motions are kinematically constrained except for rotation around the x-direction. For this reason, the kinetic energy calculation of this actuator includes only the angular velocity around the x-direction. The derivation of kinetic energy is mentioned below, where the inertia matrix of the actuator $\hat{I}_{act}$ is defined as a rotation in x-direction around the pivot point. Due to that, elements of $\hat{I}_{act}$ get zero values except first one. Non-zero element of $\hat{I}_{act}$ is $14.81 \times 10^{-7}\ kgm^2$.

$$KE = \frac{1}{2}\bar{V}_{end}^{T} m_{end} \bar{V}_{end} + \frac{1}{2}\bar{W}_{end}^{T} (\hat{R}_1^2)^T \hat{I}_{end} (\hat{R}_1^2) \bar{W}_{end} + \frac{1}{2}\bar{W}_{act}^{T} \hat{I}_{act} \bar{W}_{act} \tag{3.31}$$

where m_{end}, $\hat{I}_{end}$ and $\bar{V}_{end}$ refer to mass, inertia matrix and linear velocity at the center of motion of the mobile platform. $\hat{I}_{end}$ and $\bar{V}_{end}$ are defined in $\mathbf{F}_2$ and $\mathbf{F}_1$, respectively.

$$\bar{V}_{end} = \frac{d(\hat{R}_2^1 \bar{L}_{end})}{dt} \rightarrow \bar{V}_{end} = \hat{\mathbf{J}}_v \begin{bmatrix} \dot{\phi} \\ \dot{\psi} \\ \dot{d} \end{bmatrix} \tag{3.32}$$

where $\bar{L}_{end}$ indicates the CoM of the mobile platform, also, $\hat{\mathbf{J}}_v$ is a matrix to derive linear velocities of the mobile platform from the velocities of task space variables.

The angular velocity column matrices; $\bar{W}_{end}$ and $\bar{W}_{act}$ in Eq. 3.31 are equal to $\begin{bmatrix} \dot{\theta}_x & \dot{\theta}_y & 0 \end{bmatrix}^T$. To obtain the velocities in terms as a function of generalized coordinates, a Jacobian $\hat{\mathbf{J}}_w$ matrix is used as seen below.

$$\begin{bmatrix} \dot{\theta}_x \\ \dot{\theta}_y \\ 0 \end{bmatrix} = \hat{\mathbf{J}}_w \begin{bmatrix} \dot{\theta}_1 \\ \dot{\theta}_2 \\ \dot{\theta}_3 \end{bmatrix} \tag{3.33}$$

By using Eq. 3.31 - 3.33, the kinetic energy is obtained as

$$KE = \frac{1}{2} \begin{bmatrix} \dot{\theta}_1 \\ \dot{\theta}_2 \\ \dot{\theta}_3 \end{bmatrix}^T (\hat{\mathbf{J}}_n^T (\hat{\mathbf{J}}_v)^T m_{end} \hat{\mathbf{J}}_v \hat{\mathbf{J}}_n + \hat{\mathbf{J}}_w^T ((\hat{R}_2^1) \hat{I}_{end} (\hat{R}_2^1)^T + \hat{I}_{act}) \hat{\mathbf{J}}_w) \begin{bmatrix} \dot{\theta}_1 \\ \dot{\theta}_2 \\ \dot{\theta}_3 \end{bmatrix} \tag{3.34}$$

From Eq. 3.30 and 3.34, the inertia matrix is obtained as;

$$M = \hat{\mathbf{J}}_n^T (\hat{\mathbf{J}}_v)^T m_{end} \hat{\mathbf{J}}_v \hat{\mathbf{J}}_n + \hat{\mathbf{J}}_w^T ((\hat{R}_2^1) \hat{I}_{end} (\hat{R}_2^1)^T + \hat{I}_{act}) \hat{\mathbf{J}}_w \tag{3.35}$$

3.3.2. Calculation of the Simplified Gravity Matrix

According to the mentioned assumptions, the gravity matrix is calculated by using the weight of the mobile platform. The virtual work method is used to obtain the effects

of the mobile platform's mass on dynamics by a function of generalized coordinates. This equation is derived as follows;

$$\bar{T}^T \begin{bmatrix} \delta\theta_1 \\ \delta\theta_2 \\ \delta\theta_3 \end{bmatrix} + \bar{F}^T \begin{bmatrix} \delta\theta_x \\ \delta\theta_y \\ \delta d \end{bmatrix} = 0 \tag{3.36}$$

where forces or torques induced by the weight of the mobile platform form the column matrix $\bar{F}$. $\bar{T}$ refers to the generalized torque column matrix. By using Eq. 3.36, the gravity matrix is derived as;

$$\bar{G}_s(q) = -\hat{\mathbf{J}}^T \bar{F} \tag{3.37}$$

3.3.3. Verification of the Simplified Dynamic Model

The simplified dynamic model is verified with simulation studies involving three different scenarios. These studies investigate the error between torques obtained from the proposed simplified dynamic model and a dynamic model, which is designed by using the Simscape Multibody library in Matlab/Simulink. These scenarios are

1. Designing the multibody model according to the assumptions applied to the simplified dynamic model and comparing the torque values.

2. Adding correct inertia of the links and actuators to the multibody model in the first scenario and comparing the torques with the simplified dynamic model.

3. Adding correct mass of links and actuators to the multibody model in the second scenario and comparing the torques with the simplified dynamic model.

In all scenarios, simulations are done with Matlab/Simulink R2019b, where solver and step time are chosen as Dormand-Prince and 0.001. Moreover, the orientation due to the passive part is accepted as zero in all simulations. Therefore, the gravity vector is perpendicular to the base of the active part. The references are obtained from workspace studies of NeuRoboScope, shown in Fig. 3.7.

3.3.4. Simulation by Using Multibody Model in Accordance with the Assumptions

For realizing the simulation, the inertia and mass of links and actuators except the middle one are set to zero matrices in the multibody model of NeuRoboScope. Therefore, the multibody model becomes in accordance with the assumptions. This simulation aims to show the consistency between the simplified and multibody dynamics models.

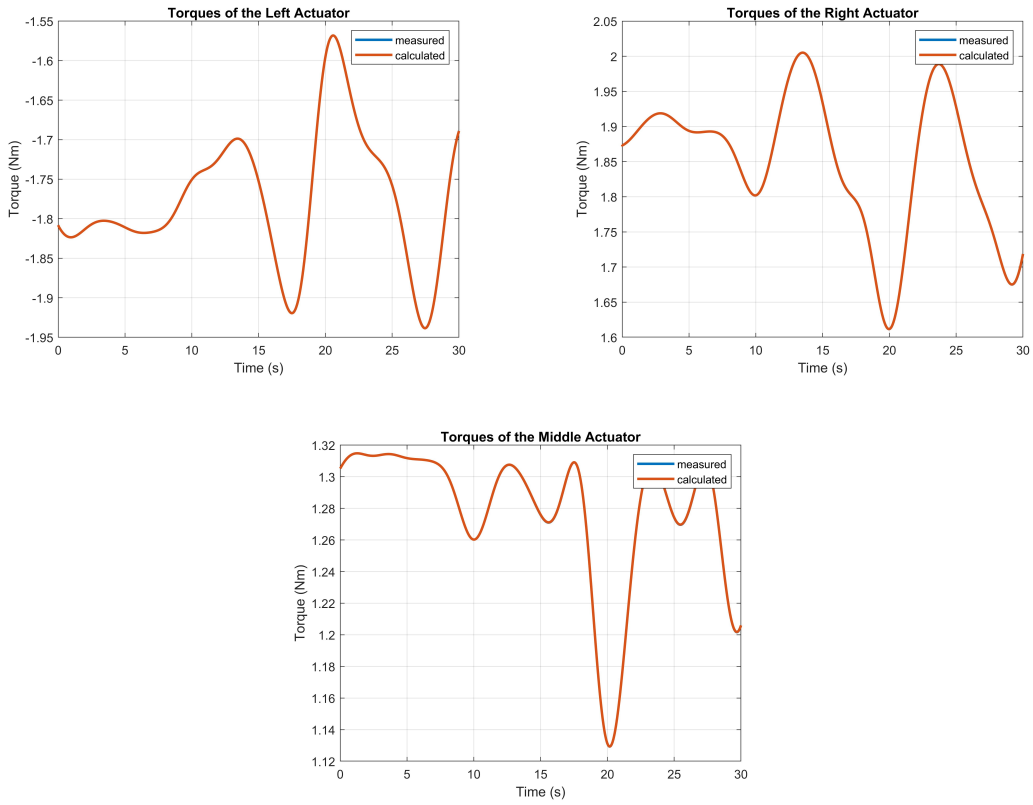

Figure 3.9. Torques of the simplified (calculated) and the multibody dynamic models (measured) designed according to the assumptions

As expected, the torque values of actuators obtained from the simplified and multibody dynamic models are approximately the same as seen in Figure 3.9. This verifies the equations in the proposed dynamic model. The simulation program cannot solve the multibody dynamic model when all inertias are chosen as zero matrices; for this reason, the inertia of particular links are inserted as relatively small values rather than zero values. Due to that, RMS errors (RMSE) are higher than expected, as observed in Table 3.2.

Table 3.2. RMSE between torques of the simplified (calculated) and the multibody dynamic models (measured) designed according to the assumptions

	Left Act.	Right Act.	Middle Act.
RMSE (Nm)	0.0676×10^{-3}	0.1135×10^{-3}	0.0611×10^{-3}

3.3.5. Simulation by Using Multibody Model with Inertia Parameters

In this study, all inertia parameters are inserted into the multibody dynamic model; however, mass of links and actuators are set to zero as in the previous simulation. It is expected that error is increased when compared with the former simulation.

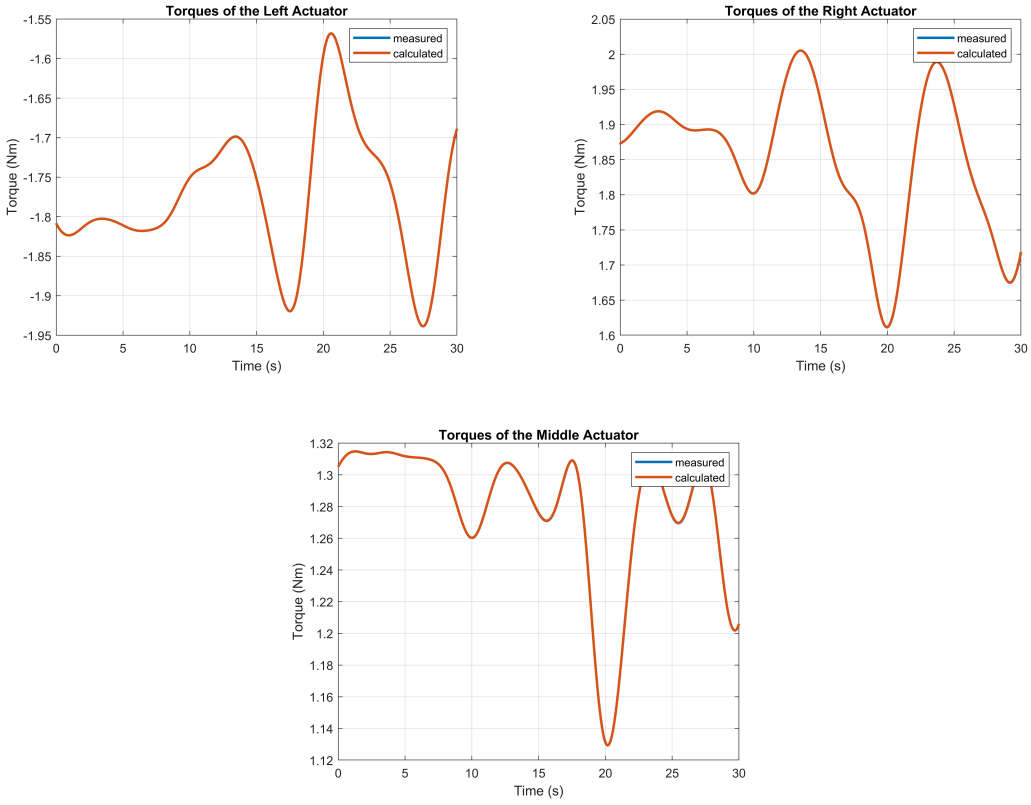

Figure 3.10. Torques of the simplified (calculated) and the multibody dynamic models with inertia parameters (measured)

It is very difficult to make an inference from Figure 3.10, and it is approximately the same as Fig. 3.9. However, Table 3.3 shows that RMSE is increased.

Table 3.3. RMSE between torques of the simplified (calculated) and the multibody dynamic models with inertia parameters (measured)

	Left Act.	Right Act.	Middle Act.
RMSE (Nm)	0.3789×10^{-3}	0.1965×10^{-3}	0.3185×10^{-3}

3.3.6. Simulation by Using Multibody Model with Full Dynamic Parameters

In contrast to the first and second scenarios, all dynamic parameters are inserted into the multibody model. The expectation of results is that the mass parameters of the robot result in higher torques errors when compared with other simulations.

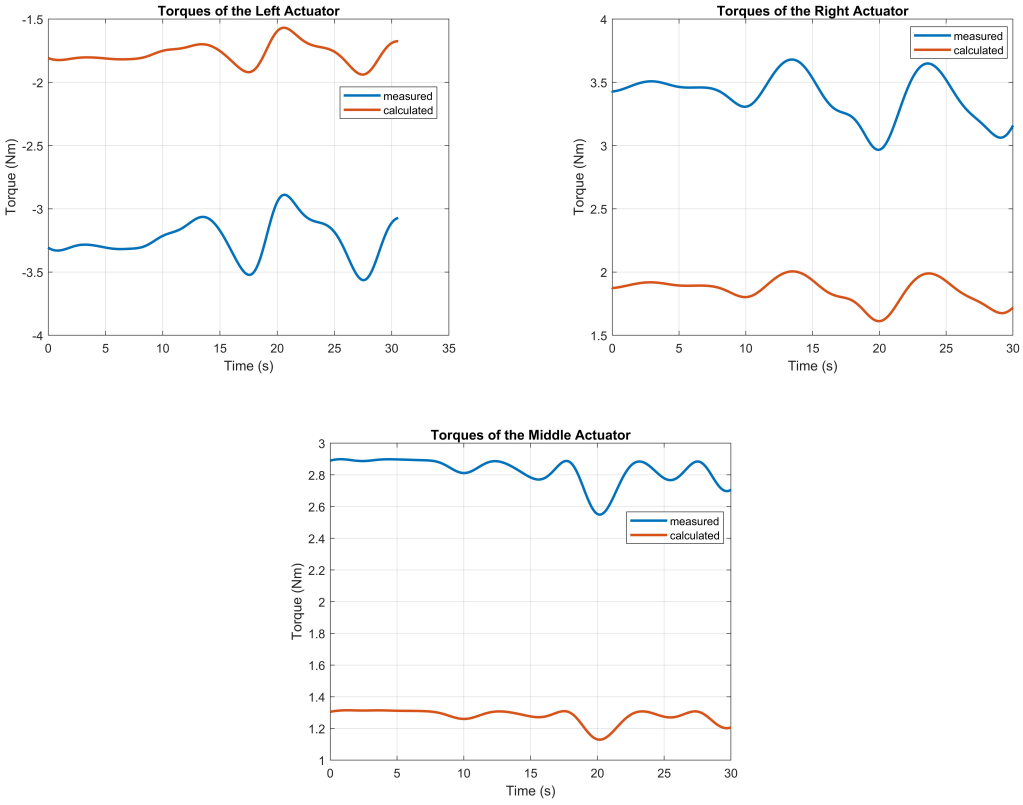

Figure 3.11. RMSE between torques of the simplified (calculated) and the multibody dynamic models with full dynamic parameters

Table 3.4 shows that RMS torque errors have unacceptably high values. Also, Figure 3.11 reflects that the dynamic behaviors of models are the same, and there is a scaling

error. As explained in the next section, a correction factor method for the simplified dynamic is proposed to deal with the error.

Table 3.4. Torques of the simplified (calculated) and the multibody dynamic models with full dynamic parameters (measured)

	Left Act.	Right Act.	Middle Act.
RMSE (Nm)	1.4691	1.5350	1.5475

3.4. Correction Coefficients for the Simplified Dynamic Model

When the studies mentioned above are investigated, high torque errors between the simplified dynamic model and the multibody dynamic model are observed. It means that the simplified dynamic model cannot be a substitute for the full dynamic model. To obtain an acceptable error, studies on the correction coefficient are done. The coefficients $K_{corr,i}$ are obtained as;

$$K_{corr,i} = mean(\frac{T_{\mathrm{i}}^*}{T_{\mathrm{i}}}) \tag{3.38}$$

where i refers to right/left/middle actuators. T_{i}^* and T_{i} are generated torques from the multibody model and simplified dynamic model, respectively.

To obtain optimal coefficients, sixteen different reference trajectories are chosen and four different simulations are done for each trajectory. The obtained averaged coefficients for the reference trajectories are shown in Table 3.5 where it is observed that the values are similar to each other. Therefore, the average of them can be used as a correction coefficient. The simplified dynamic model is modified as below.

$$\bar{T} = \hat{K}_{corr}(\hat{M}(\bar{q})\ddot{\bar{q}} + \bar{G}(\bar{q})) \tag{3.39}$$

where $\hat{K} = \begin{bmatrix} K_{corr,1} & 0 & 0 \\ 0 & K_{corr,2} & 0 \\ 0 & 0 & K_{corr,3} \end{bmatrix}$, $K_{corr,1}$ = 1.8246, $K_{corr,2}$ = 1.8226 and $K_{corr,3}$ = 2.2051.

By using these coefficients, the simplified dynamic model is verified with the multibody dynamic model following the trajectory in Fig. 3.7. The torque errors are observed as shown in Table 3.6;

Table 3.5. Reference inputs of the NeuRoboScope used in the simulations and calculated correction coefficients

Reference (Sin)			Correction Coefficient		
ϕ (rad.)	ψ (rad.)	d (mm)	$K_{corr,1}$	$K_{corr,2}$	$K_{corr,3}$
0	0	150 - 160	1.8318	1.8263	2.2651
0	0.2043	150 - 160	1.8318	1.8259	2.2701
0.1205	0	150 - 160	1.8314	1.8243	2.2664
0.1205	0.2043	150 - 160	1.8315	1.8239	2.2711
Fig. 3.7		150 - 160	1.8280	1.8286	2.2689
0	0	195 - 205	1.8310	1.8257	2.2111
0	0.2043	195 - 205	1.8325	1.8268	2.2120
0.1205	0	195 - 205	1.8299	1.8228	2.2114
0.1205	0.2043	195 - 205	1.8314	1.8239	2.2121
Fig. 3.7		195 - 205	1.8269	1.8292	2.2121
0	0	240 - 250	1.8212	1.8157	2.1845
0	0.2043	240 - 250	1.8226	1.8167	2.1819
0.1205	0	240 - 250	1.8197	1.8115	2.1840
0.1205	0.2043	240 - 250	1.8208	1.8125	2.1813
Fig. 3.7		240 - 250	1.8147	1.8207	2.1834
0.2618	0.3491	150 - 250	1.8311	1.8472	2.2111

Table 3.6. RMSE beween torques of the simplified and the multibody dynamic models with full dynamic parameters

	Left Act.	Right Act.	Middle Act.
RMSE (Nm)	0.0215	0.0206	0.0270

The RMSE of torques in Table 3.6 is acceptable where the maximum torque values are $3.5639\ Nm$, $3.6804\ Nm$ and $2.8990\ Nm$ for the left, right and middle actuators, respectively. Therefore, the simplified dynamic model can be used in the motion control algorithm.

3.5. Correction Coefficients for the Simplified Dynamic Model When the NeuRoboScope's Base Is Rotated

In the former section, the simplified dynamic model with coefficients is derived when the rotation matrix $\hat{R}_0^1$ is equal to the identity matrix. This means that $\mathbf{F}_1$ (base

frame) is coincident with $\mathbf{F}_0$ (world frame) shown in Figure 3.5. The rotation matrix is defined below where the frame is rotated around $\vec{U}_4$ by θ_4.

$$\hat{R}_0^1 = \begin{bmatrix} c(\theta_4) & 0 & -s(\theta_4) \\ 0 & 1 & 0 \\ s(\theta_4) & 0 & c(\theta_4) \end{bmatrix} \tag{3.40}$$

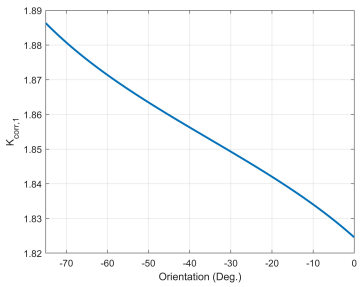

(a) The values of $K_{corr,1}$

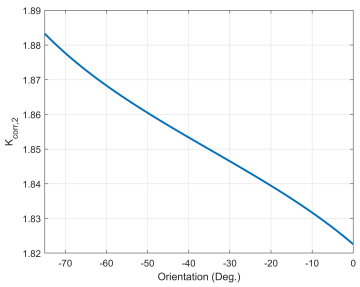

(b) The values of $K_{corr,2}$

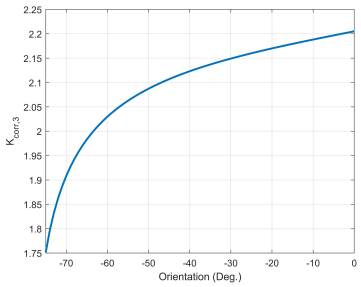

(c) The values of $K_{corr,3}$

Figure 3.12. Coefficient for each θ_4 angle

Table 3.7. The correction coefficients of the simplified dynamic models and the simulation results when $\theta_4 = -10°$, $-40°$, and $-70°$

$\theta_4°$	**Correrction Coefficients**			**RMSE (Nm)**			**Maximum Torques (Nm)**		
-	$K_{corr,1}$	$K_{corr,2}$	$K_{corr,3}$	T_1	T_2	T_3	T_1	T_2	T_3
-10	1.83	1.83	2.18	0.0193	0.0192	0.0377	3.8817	3.9943	2.8390
-40	1.85	1.85	2.12	0.0164	0.0154	0.0505	4.2109	4.3234	2.3086
-70	1.88	1.88	1.9	0.0289	0.0268	0.0807	3.6612	3.7174	1.3330

In this study, θ_4 gets values between 0^o to -75^o. In this range, the correction coefficients for the simplified dynamic model are obtained for each value of θ_4 as seen in Fig. 3.12 by applying the same methodology in the previous section.

The simulation studies for the different θ_4 value are done by comparing the torques obtained from the simplified and multibody dynamic models. In this simulation, the trajectory given Fig. 3.7 is followed and the results are presented in Table 3.7 when $\theta_4 = -10^\circ$, -40°, and -70°.

CHAPTER 4

MOTION CONTROL DESIGN & IMPLEMENTATION FOR THE NEUROBOSCOPE

Active compliant control algorithms require a motion controller as a low-level controller. In this dissertation, the design of the position controllers, such as computed torque and independent joint control approaches, is presented and experimentally verified. To apply the computed torque method, the full dynamics of the robot is required; for that reason, the simplified dynamic model with a new correction coefficient method is proposed in the previous section to run the controller at high frequencies in the ARM Cortex M4 processor. The dynamics of the robot's actuators are the key parameter for designing the control parameter. Therefore, the dynamics of NeuRoboScope's actuation systems are derived before designing the motion controller.

4.1. Actuator Dynamics

The electromechanical model of the actuation system has an important role in the design of the controller. For that reason, this section aims to derive the actuation system's mathematical model. The model of the DC motor is presented in Fig. 4.1. When Kirchoff's law is applied to the armature circuit, the mathematical model is calculated as;

$$E_A(t) = Ri(t) - L\frac{di(t)}{dt} - E_B(t) \tag{4.1}$$

where $E_A(t)$, $i(t)$, R, L and $E_B(t)$ refer to applied driving voltage, current, resistor, inductance and back emf voltage, respectively.

In steady-state, $\frac{di(t)}{dt} = 0$ therefore, the Eq. 4.1 is modified as;

$$E_A = Ri - E_B \tag{4.2}$$

The dynamics of the dc motor's mechanical part is derived as;

$$T - b_r\dot{\theta}_r = I_r\ddot{\theta}_r \tag{4.3}$$

where T, I_r, and b_r refer to the rotor's torque, inertia, and viscous friction coefficient. θ_r

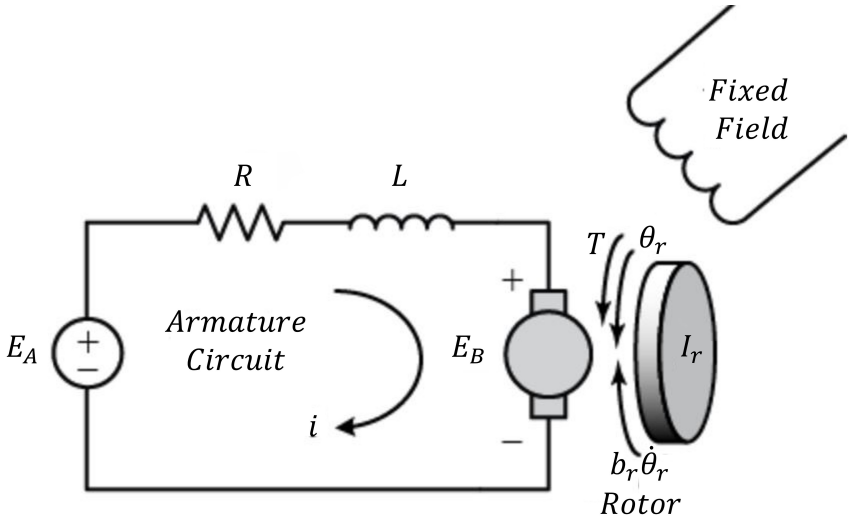

Figure 4.1. The model of the DC motor

is rotor rotation angle. By using the motor torque constant K_T and back emf constant K_B, the relations are obtained as follows.

$$T = K_T i \tag{4.4a}$$

$$E_B = K_B \dot{\theta}_r \tag{4.4b}$$

By using these relations, the Eq. 4.2 is modified as;

$$T = \frac{K_T}{R} E_A - \frac{K_T K_B}{R} \dot{\theta}_r \tag{4.5}$$

By taking Laplace of Eq. 4.5 and 4.3, the relation between E_A and $\dot{\theta}_r$ is obtained as follows.

$$\frac{\dot{\theta}_r(s)}{E_A(s)} = \frac{K_m}{(\tau_m s + 1)} \tag{4.6}$$

where motor gain $K_m = \frac{K_T}{Rb_r + K_T K_B}$ and motor time constant $\tau_m = \frac{RI_r}{Rb_r + K_T K_B}$.

In the NeuRoboScope system, three identical actuator systems, shown in Fig. 4.2 are used. These systems are constituted by a dc motor (Maxon RE 25 Ø25 mm, Graphite Brushes, 20 Watt), a planetary gearhead with a reduction ratio 181:1 (Maxon GP 26 A Ø26 mm), a capstan drive mechanism with a reduction ratio 5:1, a magnetic brake (Maxon Brake AB 28) and a magnetic encoder (MagAlpha MA707 Absolute Encoder).

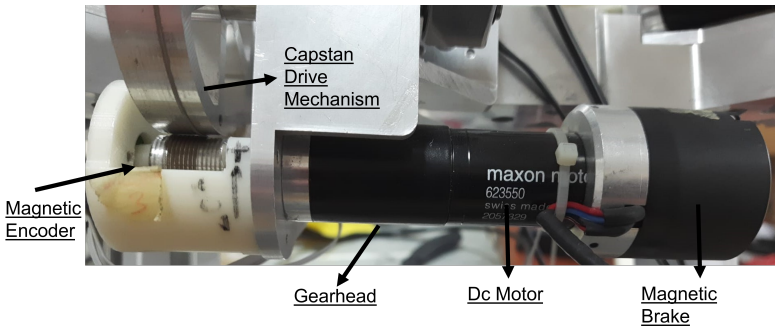

Figure 4.2. Actuation system of the NeuRoboScope

The dynamic studies explained in the previous section include the inertia of the capstan drive mechanism. Due to that, its inertial parameters are neglected in this study. The information about inertia, efficiency, motor torque constant, and motor back emf constant from the datasheets of the motor and gearhead are presented in Table 4.1. However, the datasheets do not include information about dry and viscous friction. Also, the resistor's value is changed according to external effects such as temperature. To find out the actuation system's unknown parameters, the actuation system's model is obtained experimentally. To perform this experiment, Escon $36/2$ motor driver is used and the operation mode is chosen as an open-loop speed controller. In this mode, the input is the velocity set value in rpm (shown as $\eth$), and the motor driver converts the set velocity to voltage value. Also, this mode has $(i \times R)$ compensation; however, the feature of the driver is disabled during the experiments.

Table 4.1. Inertial parameters of the NeuRoboScope's actuation system consisting of the DC motor and its gearhead

	Inertia (gcm^2)	Max. Efficiency $(\%)$	K_T $(\frac{Nm}{A})$	K_B $(\frac{V}{rad/s})$
Motor	14.5	-	0.0115	0.0115
Gearhead	0.31	70	-	-

In experiments, the input is given as a sinusoidal wave with different frequencies, and the actuation system's response is measured using the encoder. As seen in Fig. 4.2, the encoder measures the rotation angle of the gearhead instead of the motor. The relation between the rotation angle of the motor (θ_r) and the measured rotation angle (θ_m) is shown in Eq. 4.7 where N is the reduction ratio.

$$\theta_r = N\theta_m \tag{4.7}$$

Therefore, the Eq. 4.6 is modified as;

$$\frac{\dot{\theta}_m(s)}{\eth(s)} = \frac{K_m^*}{(\tau_m s + 1)} \tag{4.8}$$

where $K_m^* = \frac{K_m 30}{N\pi K_B}$.

In the experimental study, the effect of dry friction is considered, and it is modeled as Coulomb friction in the unit of the actuator's input that is rpm. The value is measured as $276.575\ rpm$ experimentally.

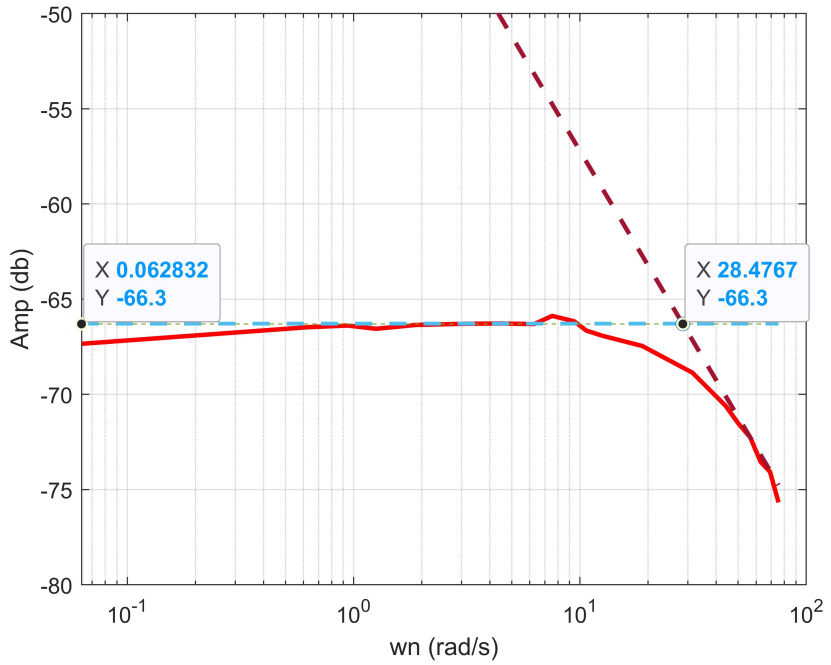

Figure 4.3. The frequency response of the actuation system of the NeuRoboScope

In order to realize frequency response analysis, the measured dry friction is added as feedforward and the output velocity is calculated by taking the derivative of the measured position from the encoder with respect to time. In Fig. 4.3 , the frequency response of the system is plotted. The natural frequency ω_n is calculated as $28.4767\ \frac{rad}{s}$ that is equal to $\frac{1}{\tau_m}$ in Eq. 4.8, therefore, $\tau_m = 0.0351\ s$. Also, $20\log_{10}(K_m^*) = -66.3\ db$ and $K_m^* = 4.8417 \times 10^{-4}$. The transfer function between $\dot{\theta}_m$ and $\eth$ is obtained as;

$$\frac{\dot{\theta}_m(s)}{\eth(s)} = \frac{4.8417 \times 10^{-4}}{(0.0351 s + 1)} \tag{4.9}$$

The inertia of actuation system I_r is calculated as $14.81\ gcm^2$. From the ratio of $\frac{K_m^*}{T_m}$, the resistor of armature R is calculated as $3.7754\ ohm$.

From (Braun;, 2012), the speed torque gradient $\frac{\Delta\eth}{\Delta T}$ is calculated as

$$\frac{\Delta\eth}{\Delta T} = \frac{30}{pi}\frac{R}{K_T^2} \tag{4.10}$$

For the actuator of the NeuRoboScope system, $\frac{\Delta\eth}{\Delta T} = 2.7261 \times 10^5$.

4.2. Computed Torque Design & Experimental Results

A computed torque approach with a simplified dynamic model is proposed to control the position. To design the controller, the error is defined as below.

$$\bar{e} = \bar{q}_a^{des} - \bar{q}_a \tag{4.11}$$

where $\bar{q}_a^{des}$ is desired generalized coordinate column matrix. $\bar{e}$ refers to position error column matrix.

To reach desired behaviour of the position error, K_p and K_d get proper value in Eq.4.12.

$$\ddot{\bar{e}} + \hat{K}_d\dot{\bar{e}} + \hat{K}_p\bar{e} = 0 \tag{4.12}$$

where $\hat{K}_d = K_d\hat{1}$ and $\hat{K}_p = K_p\hat{1}$.

The characteristic equation of the second-order system is shown as follows;

$$s^2 + 2\zeta\omega_n s + \omega_n^2 = 0 \tag{4.13}$$

The performance criteria of the behavior of the error are based on the capability of the actuation system. In previous section, motor time constant τ_m is calculate as 0.0351 s. The performance criteria are defined as follows;

$$\zeta = 0.707 \tag{4.14a}$$

$$4\tau_m = \frac{4}{\zeta\omega_n} = 0.1404s \tag{4.14b}$$

$$w_n = 40.2971 \tag{4.14c}$$

Therefore, the controller coefficients are determined as

$$K_p = \omega_n^2 = 1623.85 \tag{4.15a}$$

$$K_d = 2\zeta\omega_n = 56.9801 \tag{4.15b}$$

To design of computed torque controller, the Eq. 4.12 is modified as;

$$\bar{a}_q = \ddot{\bar{q}}_a + \hat{K}_d\dot{\bar{e}} + \hat{K}_p\bar{e} \tag{4.16}$$

A computed torque controller by using the simplified dynamic is designed below where $\bar{u}$ refers to control input.

$$\bar{u} = \hat{K}_{corr}(\hat{M}_s(\bar{q}_a)\bar{a}_q + \bar{G}_s(\bar{q}_a)) \tag{4.17}$$

As mentioned above, the rotation angle of the gearhead is measured by the encoder. The input of actuation is velocity set value $\eth$. The total reduction ratio is 905:1 (gearhead reduction ratio (181:1) + capstan drive mechanism reduction ratio (5:1)). The Eq. 4.17 is modified as;

$$\bar{\eth} = \frac{\Delta\eth}{\Delta T}\left(\frac{\hat{K}_{corr}\hat{M}_s(\bar{q}_a)}{(905)(5)}\bar{a}_q + \frac{\hat{K}_{corr}\bar{G}_s(\bar{q}_a)}{905}\right) \tag{4.18}$$

To evaluate the performance of the design controller, experimental studies are done where reference trajectories of the end-effector motion $(\phi^{des}, \psi^{des}, d^{des})$ of the NeuRoboScope are given. By using inverse kinematic, the reference for joint angles $(\theta_1^{des}, \theta_2^{des}, \theta_3^{des})$ are calculated. In this experiment, the base of robot is rotated -28.5° around $\vec{U}_4$ therefore, the $\hat{K}_{corr}$ from Fig. 3.12 is calculated as;

$$\hat{K}_{corr} = \begin{bmatrix} 1.848 & 00 & \\ 0 & 1.845 & 0 \\ 0 & 0 & 2.152 \end{bmatrix} \tag{4.19}$$

4.2.1. Experimental Setup

The experimental setup is constituted of three Escon 36/2 Servo Controller to drive the actuation system, a STM32 Discovery board, including an ARM Cortex M4 processor and the NeuRoboScope as shown in Fig. 4.4.

The reference of the NeuRoboScope is generated in the STM32 Discovery board, which receives the angular data from the encoders by SPI communication. The board runs the control algorithms at $500\ Hz$ and the control inputs are converted to the PWM signals, which sends to ESCON 36/2 Servo Controller. Therefore, the servo controllers regulate the voltage values for driving the actuators of the NeuRoboScope robot.

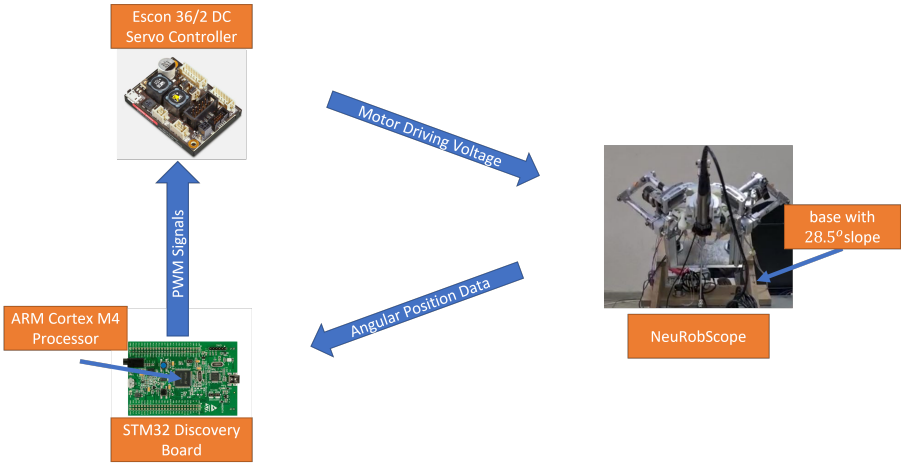

Figure 4.4. Experimental setup for the motion control studies

4.2.2. First Experiment: Changing in d with Kept ϕ and ψ Constant

In the first scenario, initial values are given as $0°$, $0°$ and $200\ mm$ for ϕ, ψ and d respectively. The references are given as;

$$\phi^{des} = 0° \tag{4.20a}$$

$$\psi^{des} = 0° \tag{4.20b}$$

$$d^{des} = \begin{cases} 200\ mm & t < 10\ s \\ 200 + 50sin(2\pi 0.1(t-10))\ mm & t \geq 10\ s \end{cases} \tag{4.20c}$$

where t refers to the time in seconds and the reference is given as the initial condition for 10 seconds. The RMSE between the reference and measured data is presented in Table 4.2.

Table 4.2. RMSE between the reference and measured data of ϕ, ψ and d when changing in d with kept ϕ and ψ constant

	ϕ	ψ	d
RMSE	$0.0515°$	$0.1080°$	$0.2417\ mm$

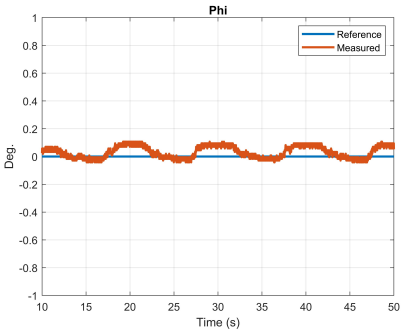

(a) Reference and measured value of ϕ

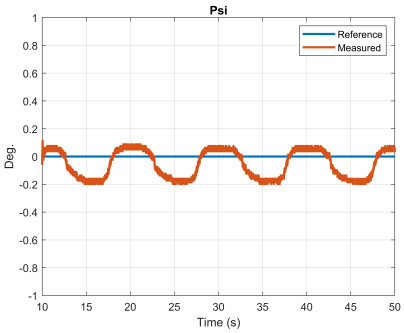

(b) Reference and measured value of ψ

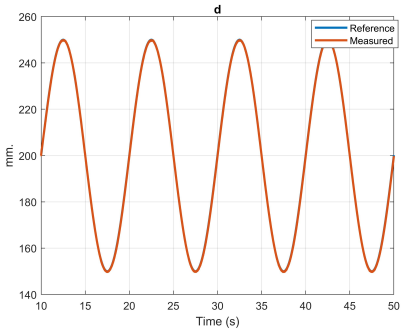

(c) Reference and measured value of d

Figure 4.5. The reference and measured values of ϕ, ψ and d

4.2.3. Second Experiment: Changing in ϕ with Kept ψ and d Constant

In the second scenario, initial values are given as $0°$, $0°$ and $150\ mm$ for ϕ, ψ and d respectively. The references are given as;

$$\phi^{des} = \begin{cases} 0° & t < 10\ s \\ 15sin(2\pi 0.1(t-10))° & t \geq 10\ s \end{cases} \tag{4.21a}$$

$$\psi^{des} = 0° \tag{4.21b}$$

$$d^{des} = 150\ mm \tag{4.21c}$$

where t refers to the time in seconds and the reference is given as the initial condition for 10 seconds. The RMSE between the reference and measured data is presented in Table 4.3.

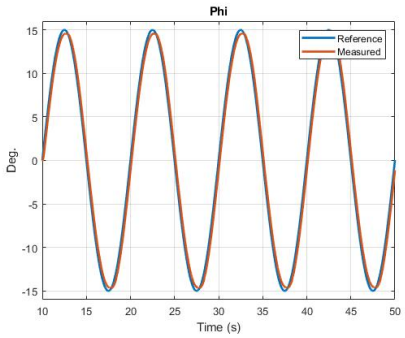

(a) Reference and measured value of ϕ

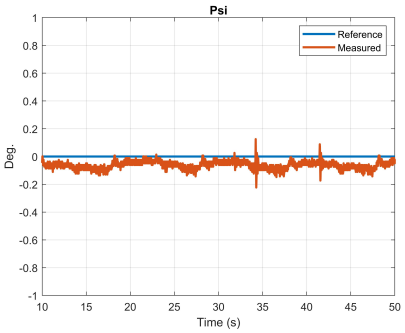

(b) Reference and measured value of ψ

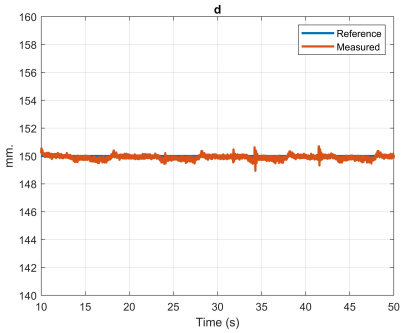

(c) Reference and measured value of d

Figure 4.6. The reference and measured values of ϕ, ψ and d

Table 4.3. RMSE between the reference and measured data of ϕ, ψ and d when changing in ϕ with kept ψ and d constant

	ϕ	ψ	d
RMSE	$0.8216°$	$0.0626°$	$0.1783\ mm$

4.2.4. Third Experiment: Changing in ψ with Kept ϕ and d Constant

In the third scenario, initial values are given as $0°$, $0°$ and $150\ mm$ for ϕ, ψ and d respectively. The references are given as;

$$\phi^{des} = 0 \tag{4.22a}$$

$$\psi^{des} = \begin{cases} 0° & t < 10\ s \\ 20sin(2\pi 0.1(t-10))° & t \geq 10\ s \end{cases} \tag{4.22b}$$

$$d^{des} = 150\ mm \tag{4.22c}$$

where t refers to the time in seconds and the reference is given as the initial condition for

10 seconds. The RMSE between the reference and measured data is presented in Table 4.4.

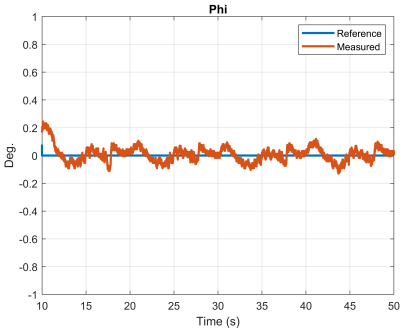

(a) Reference and measured value of ϕ

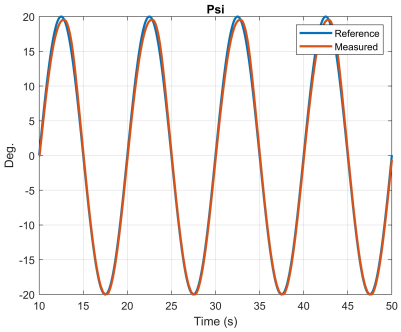

(b) Reference and measured value of ψ

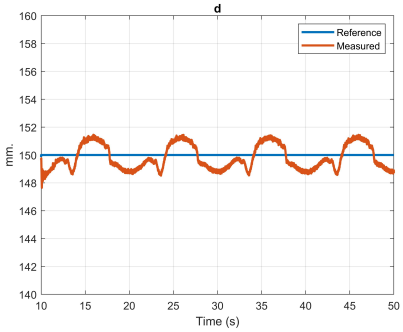

(c) Reference and measured value of d

Figure 4.7. The reference and measured values of ϕ, ψ and d

Table 4.4. RMSE between the reference and measured data of ϕ, ψ and d when changing in ψ with kept ϕ and d constant

	ϕ	ψ	d
RMSE	$0.0511°$	$0.7248°$	$0.8359\ mm$

4.2.5. Discussion

This study implements a computed torque method with the simplified dynamic model to the NeuRoboScope. In the first experiment, while the sinus wave is given as a reference for d, ϕ and ψ are kept constant, but the tracking error of the ϕ is higher than the error of the ψ. In the third experiment, where the sinus wave is given as a reference

for ψ, the tracking error of the d is affected by ψ motion. This situation is understandable because it is known that d is dependent on θ_3 and γ from kinematic studies and γ is a function of ψ. The controller includes the inertia matrix to minimize the effects of these motions. However, higher tracking errors than expected are encountered in the experiments. In the second experiment, the tracking error of the ψ and d get lower values when compared with other experiments. The inference from these experiments is that the simplified inertia matrix cannot mimic the actual inertia matrix of the system perfectly, however, the performance can be acceptable for the NeuRoboScope system when observed the RMSEs in Table 4.2 - 4.4.

4.3. Independent Joint Controller with the Active Gravity Compensation Design & Experimental Results

The mechanical dynamics of a DC motor in Eq. 4.3 can be written with adding the inertia of the load can be rewritten as;

$$T - b\dot{\theta}_r = (I_r + \frac{I_L}{N^2})\ddot{\theta}_r \tag{4.23}$$

When N gets a higher value, the term $\frac{I_L}{N^2}$ gets a relatively lower value. In the NeuRoboScope system, the reduction ratio is equal to 905, which means that the inertia's effect on the dynamics is relatively lower when compared with the actuator's dynamic. In the NeuRoboScope system, it is known from Chapter 3 that the inertia of the mobile platform has a dominant effect on the NeuRoboScope's dynamics when compared with the links' inertia for that reason, the mobile platform's inertia is used as I_L in Eq. 4.23. The inertia of the mobile platform around the rotation axis of θ_1, θ_2, and θ_3 shown in Fig. 3.3 and 3.4 are obtained by using the Solidworks CAD model and the gets approximately same as $0.055\ kgm^2$ for each axis. Since the $\frac{I_L}{N^2}$ ($\frac{0.055}{905^2} \approxeq 6.7 \times 10^{-8} kgm^2$) is approximately 4% of the inertia of the actuation system ($= 14.81 \times 10^{-7} kgm^2$). Therefore, the inertia of the NeuRoboScope can be neglected. According to this assumption, the Eq. 4.18 is modified as follows.

$$\bar{\eth} = \frac{\Delta\eth}{\Delta T}(\bar{u} + \frac{\hat{K}_{corr}\bar{G}_s(\bar{q}_a)}{905}) \tag{4.24}$$

The relation between $\eth$ and $\bar{q}_a$ is required to design a position controller. The transfer function of actuator in Eq. 4.9 is modified as

$$\frac{\theta_m(s)}{\eth(s)} = \frac{4.8417 \times 10^{-4}}{(0.0351s + 1)} \tag{4.25}$$

There is no zero in the transfer function and the poles are

$$s_1 = 0 \tag{4.26a}$$

$$s_2 = -28.4767 \tag{4.26b}$$

The performance criteria are defined in Eq. 4.14 where $\zeta = 0.707$ and $w_n = 40.2971 \frac{rad}{s}$. According to the criteria, the desired roots of system are;

$$s^*_{1,2} = -w_n\zeta \pm w_n\sqrt{1-\zeta^2}1i \tag{4.27a}$$

$$s^*_{1,2} = -28.4900 \pm 28.49861i \tag{4.27b}$$

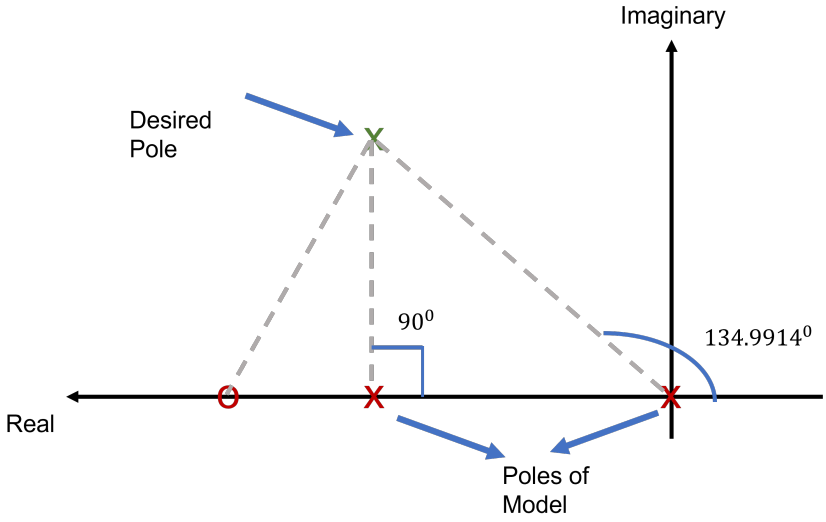

Figure 4.8. The angles between the desired poles and system poles

To reach desired criteria, a PD controller is designed as;

$$\sum < Z - \sum < P = -180^0 \tag{4.28}$$

where $< Z$ and $< P$ refer to the angle of zeros and poles. By using the relation, the angle of zero is obtained as 44.9914^0 and located at 56.9706. Therefore, the transfer function is obtained as follows;

$$G(s) = K\frac{4.8417e-04(s+56.9706)}{(0.0351s+1)} \tag{4.29}$$

From the root locus of $G(s)$ in Fig. 4.9, K is determined as 2060; therefore, the controller in the Laplace domain can be shown as;

$$\mathbb{C}(s) = 2060(s+56.9706) \tag{4.30}$$

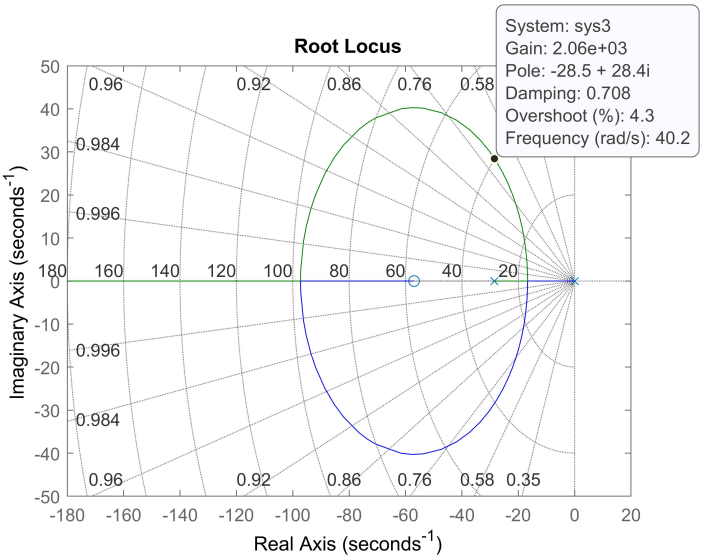

Figure 4.9. Root-locus of the open-loop model of the actuation system

$\bar{u}$ in Eq . 4.32 is designed as;

$$\bar{u} = \hat{K}_p \bar{e} + \hat{K}_d \dot{\bar{e}} \tag{4.31}$$

where $K_p = 117359.43$ and $K_d = 2060$.

The controller is designed as;

$$\bar{\eth} = \frac{\Delta \eth}{\Delta T}(\hat{K}_p \bar{e} + \hat{K}_d \dot{\bar{e}} + \frac{\hat{K}_{corr} \bar{G}_s(\bar{q}_a)}{905}) \tag{4.32}$$

4.3.1. First Experiment: Changing in d with Kept ϕ and ψ Constant

In the first scenario, initial values are given as $0°$, $0°$ and $200\ mm$ for ϕ, ψ and d, respectively. The references are given as;

$$\phi^{des} = 0° \tag{4.33a}$$

$$\psi^{des} = 0° \tag{4.33b}$$

$$d^{des} = \begin{cases} 200\ mm & t < 10\ s \\ 200 + 50sin(0.0571(t-10))\ mm & t \geq 10\ s \end{cases} \tag{4.33c}$$

where t refers to the time in seconds and the reference is given as the initial condition for 10 seconds. The root mean square of the error between the reference and measured data is presented in Table 4.5.

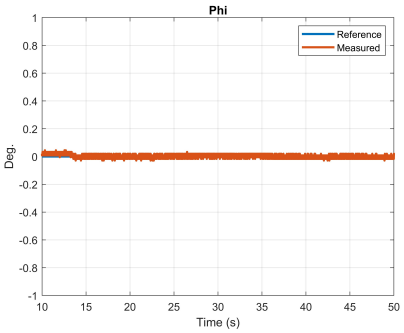

(a) Reference and measured value of ϕ

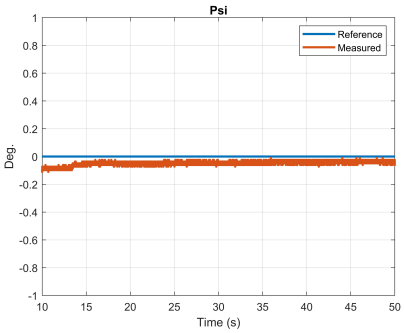

(b) Reference and measured value of ψ

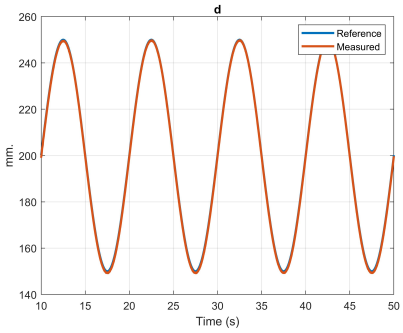

(c) Reference and measured value of d

Figure 4.10. The reference and measured values of ϕ, ψ and d

Table 4.5. RMSE between the reference and measured data of ϕ, ψ and d when changing in d with kept ϕ and ψ constant

	ϕ	ψ	d
RMSE	$0.0124°$	$0.0555°$	$0.5122\ mm$

4.3.2. Second Experiment: Changing in ϕ with Kept ψ and d Constant

In the second scenario, initial values are given as $0°$, $0°$ and $150\ mm$ for ϕ, ψ and d, respectively. The references are given as;

$$\phi^{des} = \begin{cases} 0° & t < 10\ s \\ 15sin(2\pi 0.1(t-10))° & t \geq 10\ s \end{cases} \tag{4.34a}$$

$$\psi^{des} = 0° \tag{4.34b}$$

$$d^{des} = 150\ mm \tag{4.34c}$$

where t refers to the time in seconds and the reference is given as the initial condition for 10 seconds. The root mean square of the error between the reference and measured data is presented in Table 4.6.

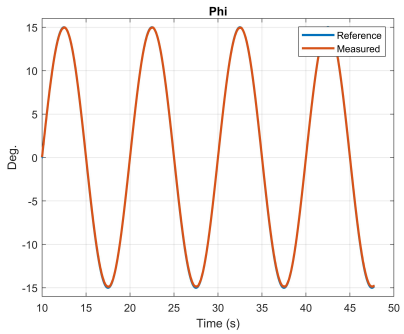

(a) Reference and measured value of ϕ

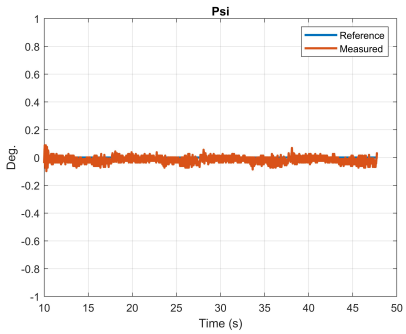

(b) Reference and measured value of ψ

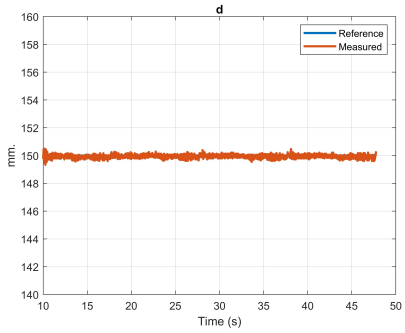

(c) Reference and measured value of d

Figure 4.11. The reference and measured values of ϕ, ψ and d

Table 4.6. RMSE between the reference and measured data of ϕ, ψ and d when changing in ϕ with kept ψ and d constant

	ϕ	ψ	d
RMSE	$0.0624°$	$0.0279°$	$0.1261\ mm$

4.3.3. Third Experiment: Changing in ψ with Kept ϕ and d Constant

In the third scenario, initial values are given as $0°$, $0°$ and $150\ mm$ for ϕ, ψ and d, respectively. The references are given as;

$$\phi^{des} = 0 \tag{4.35a}$$

$$\psi^{des} = \begin{cases} 0° & t < 10\ s \\ 20sin(2\pi 0.1(t-10))° & t \geq 10\ s \end{cases} \tag{4.35b}$$

$$d^{des} = 150\ mm \tag{4.35c}$$

where t refers to the time in seconds and the reference is given as the initial condition for 10 seconds. The RMSE between the reference and measured data is presented in Table 4.7.

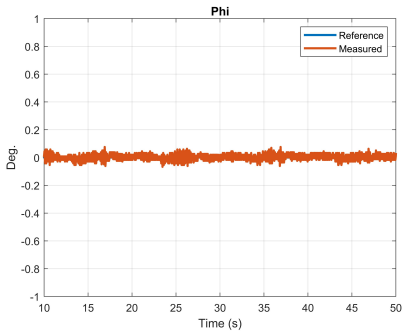

(a) Reference and measured value of ϕ

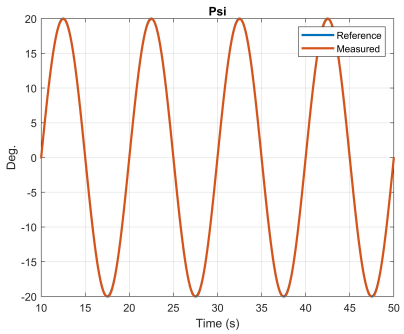

(b) Reference and measured value of ψ

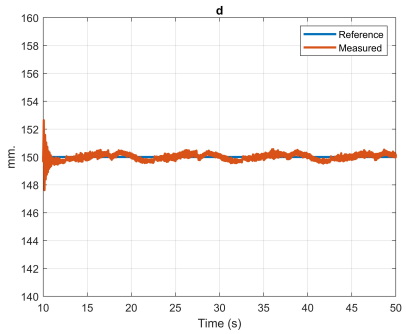

(c) Reference and measured value of d

Figure 4.12. The reference and measured values of ϕ, ψ and d

Table 4.7. RMSE between the reference and measured data of ϕ, ψ and d when changing in ψ with kept ϕ and d constant

	ϕ	ψ	d
RMSE	0.0157°	0.0488°	0.2224mm

4.3.4. Discussion

The purpose of this study is to imply that the inertia matrix of the robot can be neglected if the system has a high reduction ratio in the actuation system. In the NeuRoboScope system, the reduction ratio is $905:1$. It can be claimed that the motor's inertia has a dominant effect on the system dynamic over the inertia of NeuRoboScope. According to this assumption, the inertia of NeuRoboScope is neglected. An independent joint controller with feedforward gravitational torques is designed and the same experiments are performed to compare with the computed torque approach. This controller deals with the issue discussed in Section 4.2.5. Also, when the tracking errors are compared with the previous controller, it is observed that the independent joint controller with the gravity compensation has better performance.

4.4. Independent Joint Controller with the Passive Gravity Compensation Design & Experimental Results

In the previous section, the gravitational effect of the NeuRoboScope on the actuation system is modeled and added to the independent joint controller as a feedforward term in Eq. 4.32 for active compensation of the gravitational effect. Aldanmaz et al. (2023) implemented a hybrid method using springs and counter-masses to balance the NeuRoboScope, represented in Fig. 4.13 where m_a and G_a, m_b and G_b, and m_c and G_c refer to masses and CoM of 1^{st}, 2^{nd}, and 3^{rd} links of the NeuRoboScope's legs, respectively. During this study, $\delta = 28.5^{\circ}$ and η is changed between -64.11° and 89.63°. By using this method, the effect of gravity on the actuation system is compensated passively.

The NeuRoboScope's end-effector and the mobile platform's mass constitute the payload, and the middle leg is not used in static balancing of the payload due to avoid the collision between the links. Therefore, the payload is equally distributed to side legs as m_p ($= 442.8\ gr$), and the payload's CoM is shown as G_p. For balancing the moment on point C due to m_p and m_c, a counter-mass M_c is attached to 3^{rd} link where the CoM of M_c is located at B_c. Another counter-mass M_b having CoM on B_b is attached to 2^{nd} link to balance the moment on point A due to mass m_p, m_c, M_c, and m_b. Therefore, the CoM of the total leg's mass is relocated to point B_a that is on the 1^{st} link. Therefore, the complex balancing problem of the leg and payload is reduced to a basic problem, as observed in Fig. 4.14. As a result, the moment on point A_0 due to M_a is balanced by

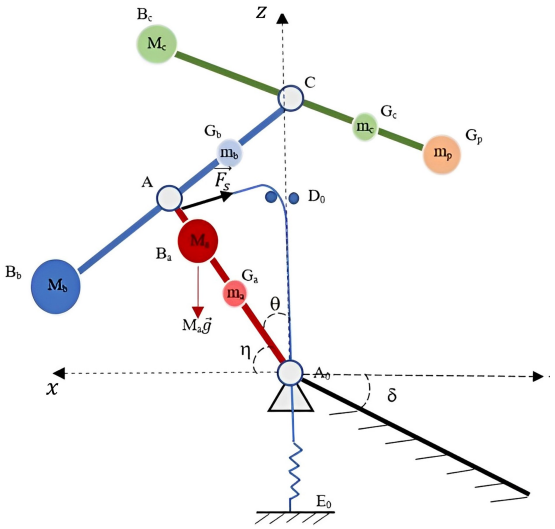

Figure 4.13. Diagram for static balancing of a leg of the NeuRoboScope with two counter-masses and a spring (Source: Aldanmaz et al., 2023)

using a spring; therefore, the leg's total mass is balanced. The counter-masses and spring calculations can be found in (Aldanmaz et al., 2023) where $\|AA_0\|$, $\|CA\|$, and $\|G_pC\|$ refer to the length of the 1^{st}, 2^{nd}, and 3^{rd} links respectively. $\|G_aA_0\|$, $\|G_bA\|$, and $\|G_cC\|$ refer to distance between CoM of 1^{st}, 2^{nd}, and 3^{rd} links and their joints. Table 1 presents the numerical value of these parameters. For statically balancing the NeuRoboScope, $\|B_aA_0\|$, $\|B_bA\|$, and $\|B_cC\|$ are calculated as $\approx 113.5\ mm$, $\approx 220\ mm$, and $\approx 115\ mm$ for both left and right legs. M_a, M_b, and M_c are designed as $\approx 2887.9\ gr$, $\approx 1301.1\ gr$, and $\approx 843.5\ gr$ for left leg and $\approx 2892\ gr$, $\approx 1302.4\ gr$, and $\approx 844.1\ gr$ for right leg, respectively. In addition, the spring constant, $\|A_0C_A\|$, and $\|A_0D_0\|$ are calculated as $1.8041\ \frac{N}{mm}$, $\approx 26.13\ mm$, and $80.22\ mm$ for balancing left leg and $1.5919\ \frac{N}{mm}$, $\approx 26.66\ mm$, and $80.22\ mm$ for balancing right leg.

By using a hybrid balancing methodology, the gravity compensation of the NeuRoboScope is provided passively. The NeuRoboScope's motion controller represented in Eq. 4.32 includes the feedforward term for compensating the gravitational effect of the NeuRoboScope on the actuators; however, this term is not required when implemented in the statically balanced NeuRoboScope. Therefore, the motion controller is modified as represented in Eq. 4.36 where $K_p = 117359.43$ and $K_d = 2060$.

$$\bar{\eth} = \frac{\Delta\eth}{\Delta T}(\hat{K}_p\bar{e} + \hat{K}_d\dot{\bar{e}}) \tag{4.36}$$

During experimental studies, it is observed that the added balancing elements limit

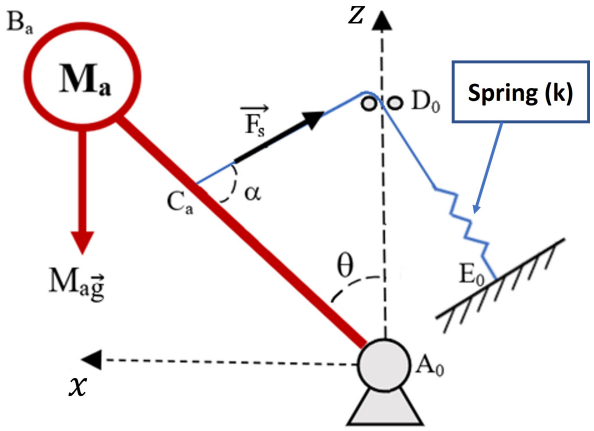

Figure 4.14. Diagram of a basic 1 DOF gravity equilibrator (Source: Aldanmaz et al., 2023)

the robots' workspace. In addition, the cable used for connecting the springs to links gets damage when the robot moves at relatively higher speeds. Therefore, the reference trajectories used in previous experimental control studies are changed in this section.

4.4.1. First Experiment: Changing in d with Kept ϕ and ψ Constant

In the first scenario, initial values are given as $0°$, $0°$ and $200\ mm$ for ϕ, ψ and d, respectively. The references are given as;

$$\phi^{des} = 0° \tag{4.37a}$$

$$\psi^{des} = 0° \tag{4.37b}$$

$$d^{des} = \begin{cases} 200\ mm & t < 10\ s \\ 200 + 50sin(0.0571(t-10))\ mm & t \geq 10\ s \end{cases} \tag{4.37c}$$

where t refers to the time in seconds and the reference is given as the initial condition for 10 seconds. The root mean square of the error between the reference and measured data is presented in Table 4.8.

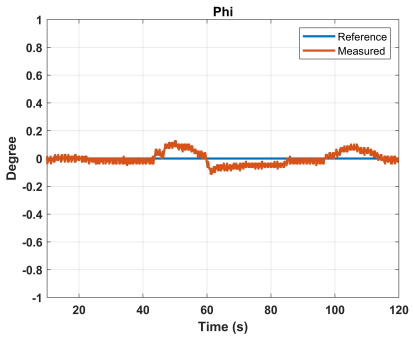

(a) Reference and measured value of ϕ

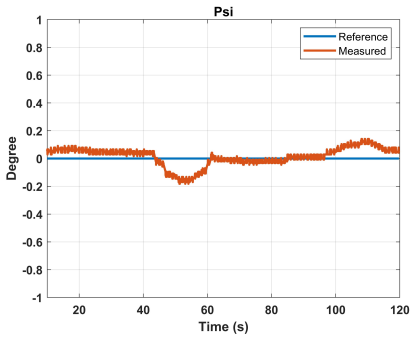

(b) Reference and measured value of ψ

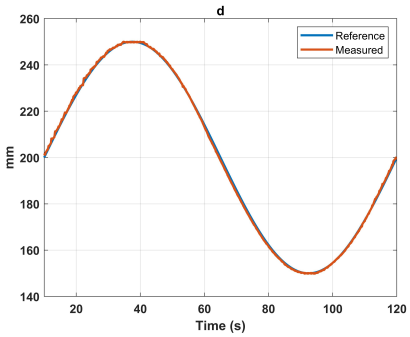

(c) Reference and measured value of d

Figure 4.15. The reference and measured values of ϕ, ψ and d

Table 4.8. RMSE between the reference and measured data of ϕ, ψ and d when changing in d with kept ϕ and ψ constant

	ϕ	ψ	d
RMSE	$0.0449°$	$0.0680°$	$0.6263\ mm$

4.4.2. Second Experiment: Changing in ϕ with Kept ψ and d Constant

In the second scenario, initial values are given as $0°$, $0°$ and $200\ mm$ for ϕ, ψ and d, respectively. The references are given as;

$$\phi^{des} = \begin{cases} 0° & t < 10\ s \\ 15sin(0.0571(t-10))° & t \geq 10\ s \end{cases} \tag{4.38a}$$

$$\psi^{des} = 0° \tag{4.38b}$$

$$d^{des} = 200\ mm \tag{4.38c}$$

where t refers to the time in seconds and the reference is given as the initial condition for 10 seconds. The root mean square of the error between the reference and measured data is presented in Table 4.9.

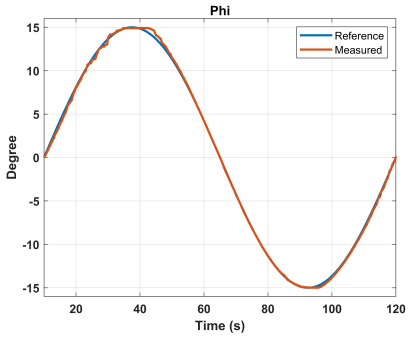

(a) Reference and measured value of ϕ

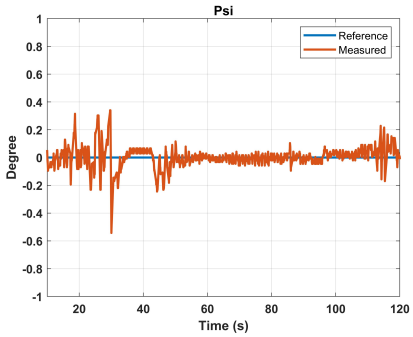

(b) Reference and measured value of ψ

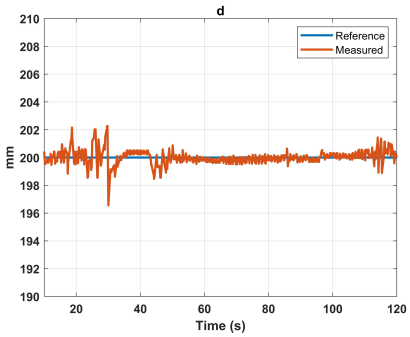

(c) Reference and measured value of d

Figure 4.16. The reference and measured values of ϕ, ψ and d

Table 4.9. RMSE between the reference and measured data of ϕ, ψ and d when changing in ϕ with kept ψ and d constant

	ϕ	ψ	d
RMSE	$0.2139°$	$0.0782°$	$0.5086\ mm$

4.4.3. Third Experiment: Changing in ψ with Kept ϕ and d Constant

In the third scenario, initial values are given as $0°$, $0°$ and $150\ mm$ for ϕ, ψ and d, respectively. The references are given as;

$$\phi^{des} = 0 \tag{4.39a}$$

$$\psi^{des} = \begin{cases} 0° & t < 10\ s \\ 20sin(0.0571(t-10))° & t \geq 10\ s \end{cases} \tag{4.39b}$$

$$d^{des} = 200\ mm \tag{4.39c}$$

where t refers to the time in seconds and the reference is given as the initial condition for 10 seconds. The RMSE between the reference and measured data is presented in Table 4.10.

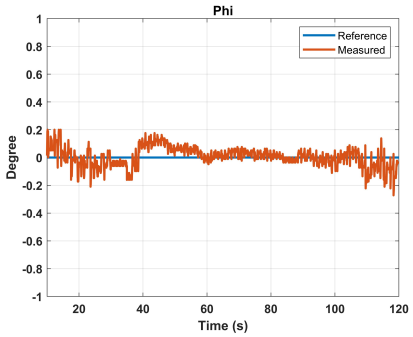

(a) Reference and measured value of ϕ

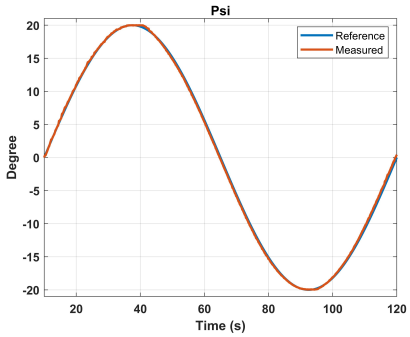

(b) Reference and measured value of ψ

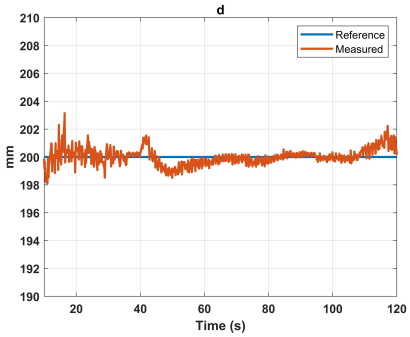

(c) Reference and measured value of d

Figure 4.17. The reference and measured values of ϕ, ψ and d

Table 4.10. RMSE between the reference and measured data of ϕ, ψ and d when changing in ψ with kept ϕ and d constant

	ϕ	ψ	d
RMSE	0.0690°	0.2347°	0.5827mm

4.4.4. Discussion

Fig. 3.8 shows that the terms related to gravity dominate NeuRoboScope's dynamics. Moreover, the speed and acceleration-related terms of the dynamics have relatively lower effects when compared with the actuator's dynamics. Due to that, the motion controller in Section 4.3 is designed concerning the gravity terms in the NeuRoboScope's dynamics. In this section, the study aims to control the motion of the statically balanced NeuRoboScope, where the gravitational effect is compensated passively. Therefore, the motion controller in Eq. 4.32 is modified as represented in Eq. 4.36, which is experimentally implemented in the statically balanced NeuRoboScope. The results show that the position errors are increased when compared with the results presented in Section 4.3. Adding the counter-masses increases the total mass of the NeuRoboScope, and the effect of the speed and acceleration-related terms on the dynamics is increased. However, the robot follows the trajectory with relatively lower acceleration and speed to avoid damaging the cable used for connecting the springs to links. Due to that, the effect of adding the counter-masses on the controller's performance is neglected. In (Aldanmaz et al., 2023), the experimental results show that the gravitational effect of the NeuRoboScope cannot be perfectly compensated in the experimental studies. As a result, the non-compensated gravitational effect on the dynamics decreases the controller's performance when compared to the experimental results in Section 4.3.

CHAPTER 5

DESIGN CRITERIA OF THE ACTIVE COMPLIANT CONTROLLERS

Active compliant control algorithms, such as explicit & implicit impedance, admittance, hybrid position/force, and parallel position/force control methodologies, make the robot achieve the desired interaction with its environments by regulating the impedance properties or following the desired both position and force trajectories. These traditional compliant control algorithms are well-known and easy to implement. However, the algorithms might fail to be used in the applications such as surgical operations where the robot contacts environments having different dynamics, such as soft tissues, bones, and relatively stiffer surgical tools held by surgeons, as shown in Fig. 5.1. This statement implies that the environment's dynamics in surgical operation can be changed instantaneously and shows discrete behavior while the robot dynamics have continuous behavior. In literature, this type of system is called a hybrid dynamical system constituted by discrete and continuous states.

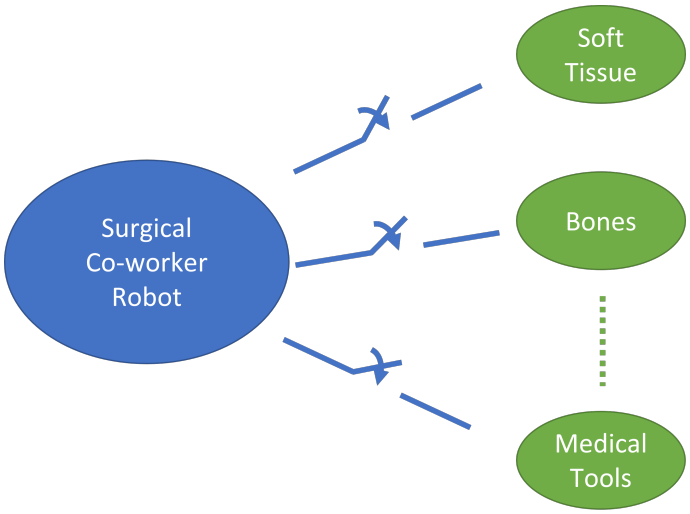

Figure 5.1. Hybrid dynamical surgical system

The situations encountered by surgical co-worker robots that affect the operations' safety and performance are outlined below.

- **Free Motion** $\Longleftrightarrow$ **Constrained Motion**

Robot collides/loses its interaction with the stiff/compliant environment while moving in free/constrained space.

- **Collision State $\longrightarrow$ Contact State**

  Robot maintains the interaction with the environment after collision.

- **Compliant Environment $\Longleftrightarrow$ Stiff Environment**

  Robot collides with soft and stiff environments.

The adaptive compliant control algorithms are presented in the literature to deal with the issues; however, the design complexity of the algorithms is increased. Instead, this dissertation aims to implement switching control methods to obtain the desired interaction between the robot and its environment. The switching method is a well-known algorithm for hybrid dynamical systems. However, the method has not been implemented in surgical robotic applications by guaranteeing safety in the literature. In this methodology, the proper active compliant control algorithms are designed for each environment separately, and the predesigned controller parameters are switched according to desired interaction. Before designing the active compliant control algorithms, the interaction scenarios for the surgical co-worker robots must be determined.

In Chapter 2, the co-worker robot is categorized as teleoperated and "hands-on" controlled robot. Teleoperated surgical co-worker robots are controlled at a distance by a surgeon. Therefore, the robot interacts with only soft /stiff tissues. Moreover, there are situations where teleoperated surgical co-worker robots and surgeons share the same operation area. In these cases, the robot may interact with surgical tools held by the surgeon. "Hands-on" controlled co-worker robots are controlled by physical interaction, so interaction with the surgeon's hand is expected. In this dissertation, the algorithms will be implemented in the NeuRoboScope, which is a teleoperated co-worker robot used in pituitary gland surgery. In addition, the force/torque sensor located at the NeuRoboScope's tip allows the robot to operate as a "hands-on" controlled robot. To evaluate the safety and performance of the robot, the design criteria of the active compliant controller are determined below.

5.1. Design Criteria of the Active Compliant Controllers

The safety and performance criteria are the main design requirements of the active compliant controller implemented in the surgical robotic. This dissertation concerns

stability and robustness as safety criteria, also agility and human - effort as performance criteria.

5.1.1. Safety Criterion - Stability

The linear dynamic model of the NeuRoboScope is derived by implementing the motion control algorithms mentioned in Chapter 4 where the robot's stability in free space is guaranteed by choosing the proper controller gains. Moreover, the dynamics of the environment have an important effect on the stability when the interaction between the robot and the environment occurs. The soft tissues are effectively modeled by linear approaches such as elastic, Kelvin-Voight, and Kelvin-Boltzmann, as explained in Chapter 2 where the active compliant control methods also have linear behavior. By using this information, the system's dynamics in constraint space can be modeled linearly, where the location of the system's poles determines the stability. The system's poles can be located in the LHS of the s-plane for achieving stability by choosing the proper gains of the active compliant control methods.

This dissertation aims to implement active compliant control algorithms for obtaining safe interaction. During the operation, the robot can encounter different environments; therefore, different controller parameters can be required to reach the desired interaction between the surgical robot and its environment. In this dissertation, the active compliant controllers' parameters are switched according to the desired interaction. Although each controller's parameters guarantee stability, the stability can be lost when switching between controllers' parameters occurs. The stability of switched systems is investigated under the switching in terms of arbitrary and constrained switching (Liberzon, 2003). Arbitrary switching refers to unpredictable switching between the systems in contrast to constrained switching, which is predictable switching between the systems, such as sequential, state-dependent, or slow switching. In the scope of the dissertation, the switching between the systems occurs unpredictably; for that reason, the stability of the linear system under arbitrary switching is investigated by using the common Lyapunov function.

5.1.1.1. Common Lyapunov Function

The state space representation of the linear time invariant switched systems can be defined as below;

$$\dot{\chi} = A_\sigma \chi + B_\sigma \varsigma \tag{5.1}$$

$$Y = C\chi \tag{5.2}$$

where χ, Y, and ς represent the system's states, outputs, and inputs, respectively. A_σ, B_σ, and C are the system's state, input, and output matrices where $\sigma : 1, 2, 3...m$ refers to switching signal. Moreover, it is assumed that A_σ for each σ is $Hurwitz$ matrix.

(i) **The conditions of the stability of the switched systems;**

(1) The piece-wise continuous input signal ς is bounded for each σ.

(2) The system, represented in Eq. 5.1 & 5.2, is uniformly exponentially stable for each σ when ς is $\hat{0}$.

(3) The system, represented in Eq. 5.1 & 5.2, is BIBO stable only if (2) and (3) are satisfied.

It is assumed that ς is bounded in all cases in this study. Therefore, the uniformly exponential stability of the unforced system can be analyzed. The states of an unforced system are represented below.

$$\dot{\chi} = A_\sigma \chi \tag{5.3}$$

(ii) **The criteria for exponential stability in the sense of Lyapunov are;**

(1) $V(0) = 0$

(2) $V(\chi) > 0$ where $\chi \neq 0$

(3) $\dot{V}(\chi) = -\eta V(\chi)$

Assumed that system q is switched to system p at an arbitrary time t and the switching signals for these systems are defined below.

$$q = \sigma(t^-) \tag{5.4}$$

$$p = \sigma(t) \tag{5.5}$$

Lyapunov functions of these systems p and q are derived as;

$$V_q(\chi) = \chi^T Q_q \chi \tag{5.6}$$

$$V_p(\chi) = \chi^T Q_p \chi \tag{5.7}$$

where Q_q and Q_p are positive definite symmetric matrices and the state χ is defined below.

$$\chi(t) = \Gamma(p, q, \chi(t^-)) \tag{5.8}$$

where $\Gamma(p, q, .)$ is a reset function. When a linear reset function exists, the state $\chi(t)$ can be redefined as below.

$$\chi(t) = \Gamma(p, q)\chi(t^-) \tag{5.9}$$

Due to exponential stability,

$$V_p(\chi) \leq V_q(\chi) \tag{5.10}$$

$$\chi^T(t) Q_p \chi(t) \leq \chi^T(t^-) Q_q \chi(t^-) \tag{5.11}$$

$$\chi(t^-)^T \Gamma(p, q)^T Q_p \Gamma(p, q) \chi(t^-) \leq \chi^T(t^-) Q_q \chi(t^-) \tag{5.12}$$

$$\Gamma(p, q)^T Q_p \Gamma(p, q) \leq Q_q \tag{5.13}$$

The Lyapunov functions of each system can be shown as a general form $V_\sigma(\chi)$. According to exponential stability conditions;

$$V_\sigma(0) = 0 \tag{5.14}$$

$$V_\sigma(\chi) = \chi^T Q_\sigma \chi \tag{5.15}$$

where Q_σ defines a positive definite symmetric matrix for each σ

$$\dot{V}_\sigma(\chi) = \dot{\chi}^T Q_\sigma \chi + \chi^T Q_\sigma \dot{\chi} \tag{5.16}$$

$$\dot{V}_\sigma(\chi) = \chi^T (A_\sigma^T Q_\sigma + Q_\sigma A_\sigma) \chi \tag{5.17}$$

From the stability conditions;

$$\dot{V}_\sigma(\chi) \leq \eta V_\sigma(\chi) \tag{5.18}$$

$$A_\sigma^T Q_\sigma + Q_\sigma A_\sigma \leq \eta Q_\sigma \tag{5.19}$$

so;

$$(A_\sigma^T Q_\sigma + Q_\sigma A_\sigma) < 0 \tag{5.20}$$

(iii) **The exponential stability conditions for the switched systems are rewritten;**

(1) Q_σ is a positive definite symmetric matrix for each σ.

(2) $(A_\sigma^T Q_\sigma + Q_\sigma A_\sigma) < 0$.

(3) $\Gamma(p,q)^T Q_p \Gamma(p,q) \leq Q_q$.

The important inferences from the (3) are that

- Asymptotically stable A_σ for each σ is enough for stability if $\Gamma(p,q) = \hat{0}$.
- $Q_p = Q_q = Q$ if $\Gamma(p,q) = \hat{1}$. That means that there should be a common Lyapunov function.

In this study, the states are not desired to change when switching occurs; therefore, $\Gamma(p,q) = \hat{1}$.

(iv) **By using the common Lyapunov function (**$V(\chi) = \chi^T Q \chi$ **), the exponential stability condition is modified as;**

(1) Q is a positive definite symmetric matrix.

(2) $(A_\sigma^T Q + Q A_\sigma) < 0$

Detailed information about the stability of the switched systems can be found in (Hespanha and Morse, 2002). The existence of the common Lyapunov function is mentioned above; however, finding out this function is another critical problem.

- **The Gradient Algorithms for Finding the Common Lyapunov Function**

The inequalities in (2) satisfy inequalities in Eq. 5.21 where Θ is a positive definite symmetric matrix and known; however, Q is unknown.

$$(A_\sigma^T Q + Q A_\sigma) + \Theta \leq 0 \tag{5.21}$$

Liberzon and Tempo (2004) proposed an iterative gradient algorithm to find the common Lyapunov function by solving linear matrix inequalities in Eq. 5.21. The gradient formula is defined below.

$$f(R + \Delta R) \approx f(R) + \langle \delta_r f, \Delta R \rangle \tag{5.22}$$

where f is a designed function for finding a common Lyapunov function, and ΔR is defined as a small perturbation with respect to R. $\langle ., . \rangle$ refers to inner product.

From Eq. 5.22, the $v(Q, A)$ is derived as below.

$$v(Q, A) := f(A^T Q + QA + \Theta) \tag{5.23}$$

The iterative gradient algorithm for finding common Lyapunov function is represented below.

$$Q_{\mathrm{i}+1} = \begin{cases} [Q_{\mathrm{i}} - \mu_{\mathrm{i}} \delta_Q v(Q_{\mathrm{i}}, A_{\sigma(\mathrm{i})})]^+ & v(Q_{\mathrm{i}}, A_{\sigma(\mathrm{i})}) > \hat{0} \\ Q_i & otherwise \end{cases} \tag{5.24}$$

where $[.]^+$ denotes a function that projects the input value into positive semi-definite space by applying eigendecomposition and replacing all negative eigenvalues with zero. In addition, μ_i is step-size and calculated as;

$$\mu_{\mathrm{i}} := \frac{\alpha v(Q_{\mathrm{i}}, A_{\sigma(\mathrm{i})}) + r\|\delta_Q v(Q_{\mathrm{i}}, A_{\sigma(\mathrm{i})}\|}{\|\delta_Q v(Q_{\mathrm{i}}, A_{\sigma(\mathrm{i})})\|^2} \tag{5.25}$$

and $\sigma(i)$ is obtained as;

$$\sigma_{\mathrm{i}} := \mathrm{i} - m\lfloor \frac{\mathrm{i}}{m} \rfloor + 1 \tag{5.26}$$

where i denotes the iteration number, $\lfloor . \rfloor$ is a function to round the input value nearest integer that is less than or equal to it. α gets a value between 0 and 2 ($0 \leq \alpha \leq 2$) and r gets positive value ($r > 0$). Moreover, $\|.\|$ denotes to Frobenius norm.

From (Liberzon and Tempo, 2004), the function $f(R)$ and $\delta_Q v(Q, A)$ are chosen as below.

$$f(R) := \lambda_{max}(R) \tag{5.27}$$

and it is assumed that $\aleph$ is eigenvector corresponding to $\lambda_{max}(R)$.

$$\delta_Q v(Q, A) := A\aleph\aleph^T + \aleph\aleph^T A^T \tag{5.28}$$

In this dissertation, Θ is chosen as $\hat{1}$. The initial value of Q is calculated by using Eq. 5.21, Θ, and A from one of the switched systems. By using the Θ and the initial value of Q, Eq. 5.24 is iteratively solved to find optimum Q matrix. Consequently, the common Lyapunov function ($V(\chi) = \chi^T Q \chi$) is obtained.

5.1.2. Safety Criterion - Robustness

The robot or environment cannot be modeled perfectly for that reason; the controller must be robust to uncertainties in dynamics. As mentioned, the robot interacting

with the environment is modeled linearly in this dissertation. Therefore, robustness is measured with a sensitivity function $L(jw)$.

5.1.3. Performance Criterion - Agility

Speed is one of the most critical factors affecting the completion time of the operation. The surgeon sends commands related to desired speed; however, the active compliant control algorithms decrease the speed of the robot to reach safe interaction. The execution time of tasks is compared to measure agility for a teleoperated surgical robot. The average speed while completing the tasks is compared as an agility metric for a 'hands-on' controlled surgical robot.

5.1.4. Performance Criterion - Human - Effort

During the operation, the surgeon physically interacts with the robot that is in "hands-on" controlled mode to give motion commands. It is desired that surgeons apply relatively small forces to move the robot. The total applied force is used as a metric of human effort. However, the metric is not used when the robot is in teleoperation mode.

5.2. Discussion

This chapter discusses the significant design criteria of the active compliant controllers for surgical co-worker robots. The usage of the mentioned criteria is varied in the controller's design according to the robot's type, environment, and desired interaction. The surgical co-worker robots are categorized as teleoperated and "hands-on" controlled robots, as mentioned in Chapter 2. The NeuRoboScope is capable of operating in both teleoperated and "hands-on" controlled modes. Therefore, the interaction scenarios of NeuRoboScope are studied in this dissertation. When NeuRoboScope is in teleoperated mode, it shares the workspace with the soft tissues on the nasal concha and a medical tool held by the surgeon. During operation, the interaction between the robot and its environment is expected, which might result in a dangerous situation. To avoid this situation, the active compliant controllers are designed considering stability, robustness, and agility. When the robot is in "hands-on" controlled mode, the surgeon moves the NeuRoboScope

Table 5.1. The design criteria of the active compliant controllers for the surgical co-worker robots

Surgical Co-Worker Robots		
Teleoperated Robot		"Hands-on" Controlled Robot
Interacting with the soft tissue.	Interacting with the soft tissue and the medical tool.	Interacting with the surgeon.
Safety Criteria • Stability • Robustness	Safety Criteria • Stability • Robustness	Safety Criteria • Stability • Robustness
Performance Criteria • Agility	Performance Criteria • Agility	Performance Criteria • Agility • Human-effort

with physical interaction in free space. The interaction between the robot and the surgeon is regulated by designing an active compliant controller concerning stability, robustness, agility, and human-effort. This study investigates two interaction scenarios for teleoperated mode and an interaction scenario for "hands-on" controlled mode. Table 5.1 presents the design criteria for different interaction scenarios for both types of the surgical robot.

The design of the active compliant controllers concerning the safety and performance criteria and the experimental results are presented in the next chapters.

CHAPTER 6

DESIGN AND EXPERIMENTAL VERIFICATION OF THE ACTIVE COMPLIANT CONTROLLER FOR TELEOPEARTION MODE

The surgeon commands the teleoperated surgical co-worker robot without the physical interaction of the surgeon with the robot. The robot shares the workspace with soft tissues on the nasal concha and a medical tool held by the surgeon. In this chapter, two interaction scenarios encountered by the NeuRoboScope are investigated. In the first scenario, the NeuRoboScope interacts with only soft tissues, and the active compliant controllers, such as impedance controller and hybrid position/force controller, are designed concerning safety and performance criteria. In the second interaction scenario, the NeuRoboScope interacts with a medical tool held by a surgeon in addition to soft tissues, and an impedance controller is designed concerning the safety criteria. The controllers are implemented in the NeuRoboScope to perform the experimental verification of them. During experimental studies, a soft silicon specimen is used instead of the real soft tissues because of the difficulty of accessing the actual patient tissue. A relatively stiffer silicon specimen is used to imitate the stiff environment, such as a medical tool held by surgeons. The silicon specimens' mathematical model is derived for the controller design. The test setup constituted by NeuRoboScope and silicon specimens is prepared to perform the experiments.

6.1. The Silicon Specimen Modeling

During experimental studies, a soft and stiff silicon specimens are used instead of the real soft tissues and a medical tool held by surgeon, respectively. The linear models in Fig. 2.18, such as elastic, Kelvin-Voight, and Kelvin-Boltzmann, are used to derive an optimum model of these specimens. However, the Maxwell model is not preferred to be used in this study due to the showing the worst performance when modeling the real soft tissues as observed in Section 2.5. The optimum parameters of each model are searched by using a constrained nonlinear minimization method. An experimental setup is prepared

to model the silicon specimens, as shown in Fig. 6.1 where a surface gauge is used for compressing the specimen precisely with the handle. However, the deflection of the specimen is measured by using the encoder (Encoder MILE, 1024 CPT, 2 Channels, with Line Drive). Due to small displacement, the deflection is calculated as a multiplication of the handle's length ($100\ mm$) and measured angle from the encoder. The data from the encoder is read and sent to Simulink/Matlab R2019b by using the STM32F4 Discovery board.

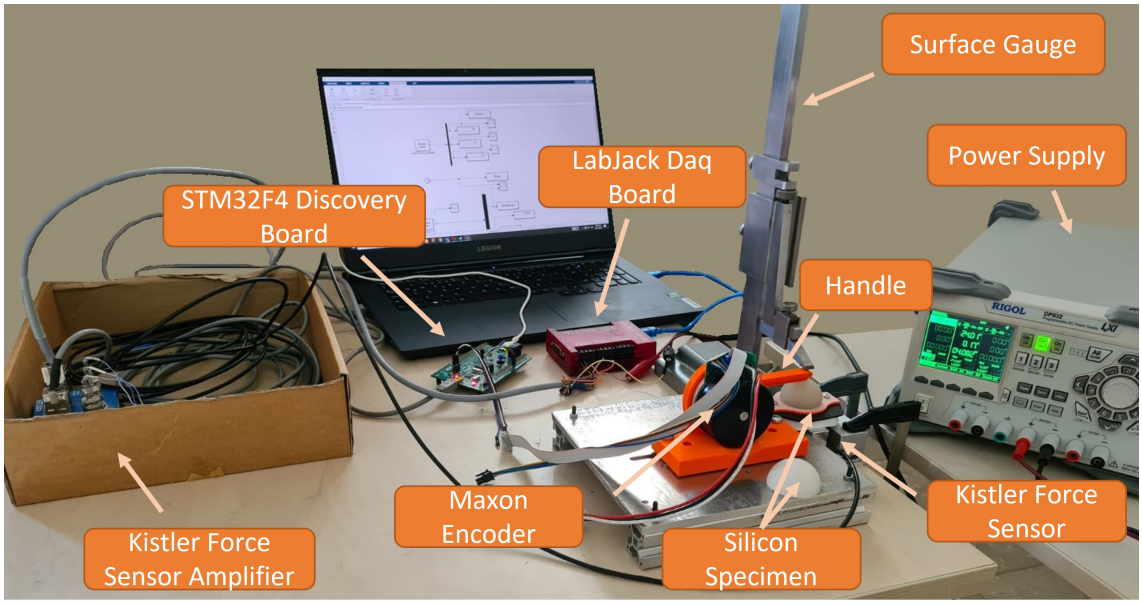

Figure 6.1. The experimental setup for the modeling the silicon specimens

The reaction force is measured by using Kistler 9017b Force Sensor while compressing the specimen. The range of force value is regulated between $-10\ N$ and $10\ N$ and mapped to the voltage between $-10\ V$ and $10\ V$ by using Kistler Amplifier Type 5073A. Labjack data acquisition board (Daq) read the force data as voltage and sent it to Simulink/Matlab R2019b.

Three different experiments are done for the soft and stiff silicon specimens separately. Fig. 6.2 presents measured reaction force and deflection values while compressing the specimens during the experiments. For each experiment done for modeling the soft and the stiff silicon specimens, the optimum parameters of elastic, Kelvin-Voight, and Kelvin-Boltzmann linear models are derived by using the '*fmincon*' solver of optimization toolbox in Matlab R2019b and the RMSE between the measured and calculated force data from experiments and the models are compared.

In the study of modeling the soft silicon specimen, the parameter k in the elastic

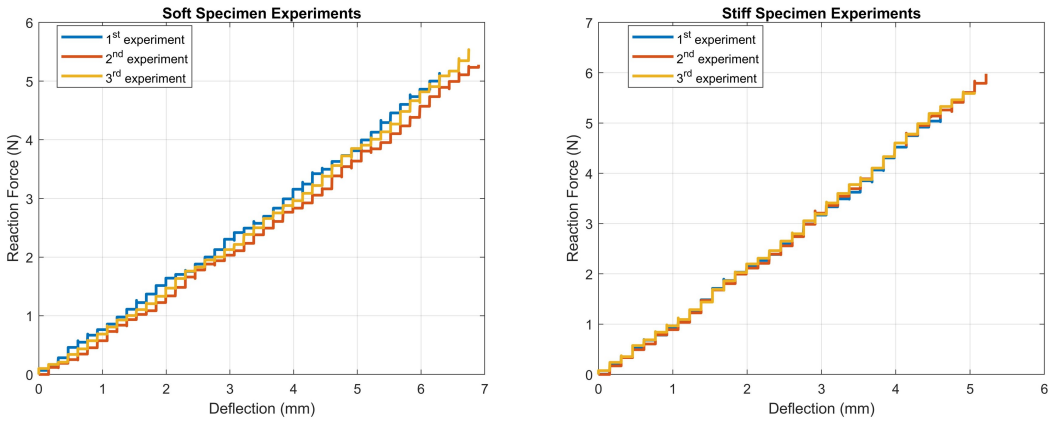

Figure 6.2. The experimental results for modeling the soft and stiff silicon specimens are presented.

models are calculated as 768.17 $\frac{N}{m}$, 720.56 $\frac{N}{m}$, and 752.69 $\frac{N}{m}$ for 1^{st}, 2^{nd}, and 3^{rd} experiments where the RMSE between the measured and calculated force data are $0.0969\ N$, $0.1586\ N$, and $0.1491\ N$, respectively. In the Kelvin-Voight model, the parameters k and b are calculated as 768.17 $\frac{N}{m}$ and $0.0053\ \frac{Ns}{m}$ for 1^{st} experiment where the RMSE between the measured and calculated force is $0.0969\ N$. The parameters k and b are calculated as 721.33 $\frac{N}{m}$ and $0.0067\ \frac{Ns}{m}$ for 2^{nd} experiment where the RMSE between the measured and calculated force is $0.1582\ N$. The parameters k and b are calculated as 752.70 $\frac{N}{m}$ and $0.0062\ \frac{Ns}{m}$ for 3^{rd} experiment where the RMSE between the measured and calculated force is $0.1491\ N$. In the Kelvin-Boltzmann model, parameters η_1, η_2, and η_3 are calculated as 768.17 $\frac{N}{m}$, $0.0053\ \frac{Ns}{m}$, and $4.6 \times 10^{-7}\ s$ for 1^{st} experiment where the RMSE between the measured and calculated force is $0.0969\ N$. The parameters η_1, η_2, and η_3 are calculated as 721.33 $\frac{N}{m}$, $0.0067\ \frac{Ns}{m}$, and $7.6 \times 10^{-7}\ s$ for 2^{nd} experiment where the RMSE between the measured and calculated force is $0.15823\ N$. The parameters η_1, η_2, and η_3 are calculated as 752.70 $\frac{N}{m}$, $0.0062\ \frac{Ns}{m}$, and $9.9 \times 10^{-7}\ s$ for 3^{rd} experiment where the RMSE between the measured and calculated force is $0.1491\ N$.

In the study of modeling the stiff silicon specimen, the parameter k in the elastic models are calculated as 1055.4 $\frac{N}{m}$, 1076.6 $\frac{N}{m}$, and 1079.6 $\frac{N}{m}$ for 1^{st}, 2^{nd}, and 3^{rd} experiments where the RMSE between the measured and calculated force data are $0.2135\ N$, $0.1764\ N$, and $0.1519\ N$, respectively. In the Kelvin-Voight model, parameters k and b are calculated as 1055.4 $\frac{N}{m}$ and $0.0127\ \frac{Ns}{m}$ for 1^{st} experiment where the RMSE between the measured and calculated force is $0.2135\ N$. The parameters k and b are calculated as 1076.6 $\frac{N}{m}$ and $0.0055\ \frac{Ns}{m}$ for 2^{nd} experiment where the RMSE between the measured and calculated force is $0.1764\ N$. The parameters k and b are calculated as 1079.6 $\frac{N}{m}$

and $0.0057\ \frac{Ns}{m}$ for 3^{rd} experiment where the RMSE between the measured and calculated force is $0.1519\ N$. In the Kelvin-Boltzmann model, parameters η_1, η_2, and η_3 are calculated as $1055.4\ \frac{N}{m}$, $0.0101\ \frac{Ns}{m}$, and $3.3 \times 10^{-7}\ s$ for 1^{st} experiment where the RMSE between the measured and calculated force is $0.2135\ N$. The parameters η_1, η_2, and η_3 are calculated as $1077.9\ \frac{N}{m}$, $0.0044\ \frac{Ns}{m}$, and $5.2 \times 10^{-4}\ s$ for 2^{nd} experiment where the RMSE between the measured and calculated force is $0.1760\ N$. The parameters η_1, η_2, and η_3 are calculated as $1080.4\ \frac{N}{m}$, $0.0046\ \frac{Ns}{m}$, and $2.5 \times 10^{-4}\ s$ for 3^{rd} experiment where the RMSE between the measured and calculated force is $0.1517\ N$.

According to the experimental results, the RMSE between the measured and calculated force is approximately the same for each linear model. Moreover, the model parameters are approximately the same when comparing the experiments. In the linear models, the parameters related to the derivative of deflection and reaction forces are close to zero. Therefore, the elastic model is used to model the stiff and soft silicon specimens accurately. The elastic parameters k for soft and stiff specimens are chosen as $747.14\ \frac{N}{m}$ and $1070.5\ \frac{N}{m}$, respectively which are averages of the obtained values in experiments. By using the calculated parameter for soft elastic silicon specimen, the percentage of the maximum errors between the measured and calculated force are approximately 4%, 2%, and 5% of maximum forces for 1^{st}, 2^{nd}, and 3^{rd} experiments where maximum force values are $5.1\ N$, $5.2\ N$, and $5.5\ N$, respectively. By using the calculated parameter for stiff elastic silicon specimen, the percentages of the maximum error between the measured and calculated force are approximately 3%, 5%, and 5% of maximum forces for 1^{st}, 2^{nd}, and 3^{rd} experiments where maximum force values are $5.1\ N$, $5.9\ N$, and $5.6\ N$, respectively.

Tugal et al. (2022) measures the rate-hardness of the pro-surgeons' right hand as $1002 \pm 568\ \frac{N}{m}$. The rate-hardness refers to the resistance of the surgeon's hand to external forces. In surgical applications, the crashing between the surgical co-worker robot and the rigid medical tool held by the surgeon is generally encountered. For performing this scenario, the stiff silicon specimen is used to imitate the rigid tool held by the surgeon because the value of the pro-surgeons' right-hand rate-hardness ($\approx 1002\ \frac{N}{m}$) is close to mechanical impedance of the stiff silicon specimen ($\approx 1070.5\ \frac{N}{m}$).

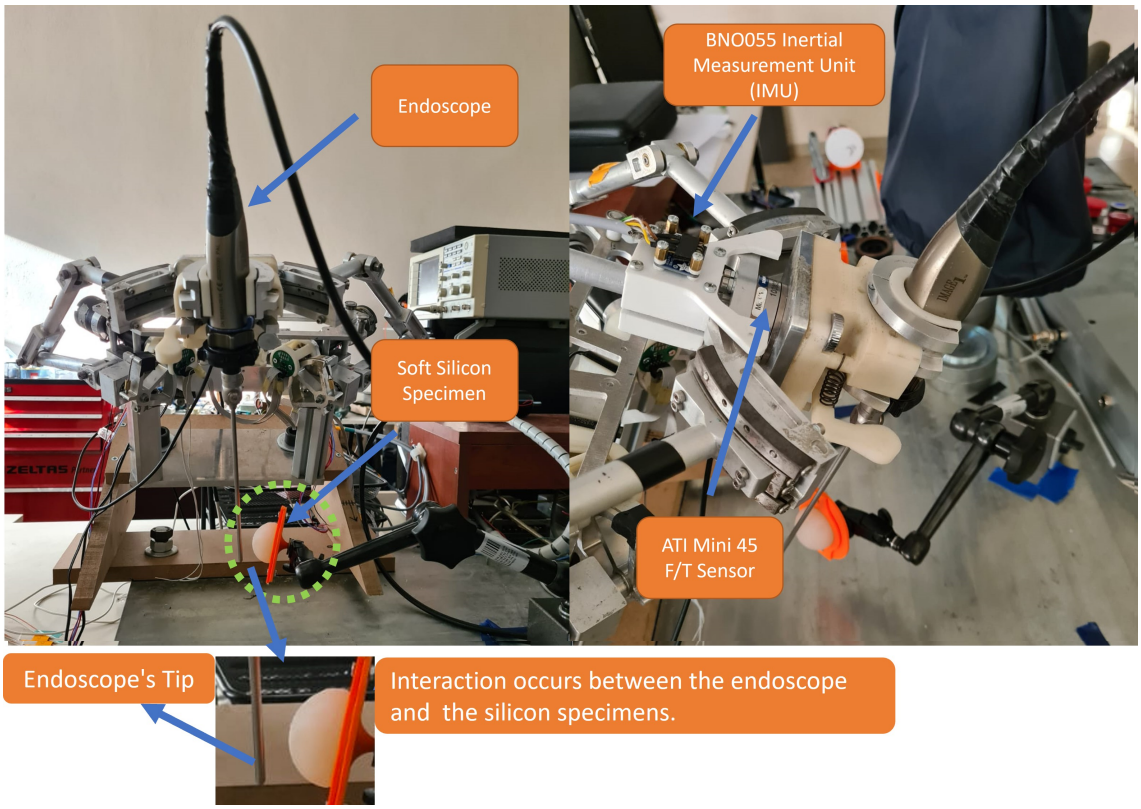

Figure 6.3. The experimental setup for testing active compliant controllers in teleoperation mode

6.2. Experimental Setup for Testing Active Compliant Controller in Teleoperation Mode

The experimental setup is prepared as below where ATI Mini-45 F/T sensor is used to measure the external force and torque data, which is attached to the endoscope. Due to that, the F/T sensor measures the weight of the endoscope when the robot moves in free space, and this value must be biased to measure actual data. In the NeuRoboScope system, the joint clearance is observed; for that reason, the location of the endoscope's center of mass cannot be calculated accurately by using the encoder's data which is connected to actuators. Due to that, an inertial measurement unit (Adafruit BNO055 9-DOF absolute orientation IMU) is used for measuring the orientation. With this information, the force and torque values due to the endoscope's weight are calculated and extracted from F/T sensor data.

The STM32 discovery board runs the motion control algorithm at $500\ Hz$, and the board receives the references of task space variables' positions (ϕ, ψ, d) from a laptop

computer and sent to the measured task space variable's position via USB interface. The data from the BNO055 IMU is read by using an Arduino microcontroller board which sends this data to the laptop computer via a USB interface. Moreover, the laptop computer reads the force and torque data from the ATI Mini-45 F/T sensor via UDP ethernet protocol. The laptop computer runs the proper compliant control algorithms by using the Real-Time library in Simulink/Matlab R2019b. The solver and step time are chosen as $Euler$ and $0.0001s$, respectively.

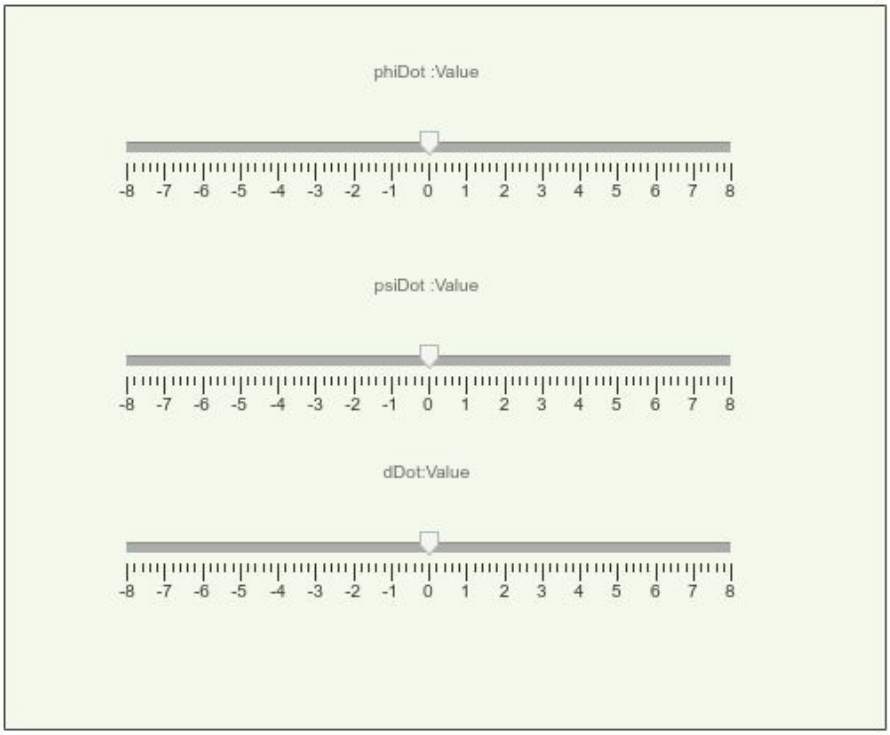

Figure 6.4. The slider block for controlling the velocity references ($\dot{\phi}$, $\dot{\psi}$, $\dot{d}$) by user during experiments

In the real surgical scenario, the surgeon wears a ring-shaped remote controller. The position data of the surgeon's hand is mapped to velocity data and sent to the NeuRoboScope. For imitating this scenario, slider blocks are added to the Simulink project to tune the task space variables' velocity references ($\dot{\phi}_c$, $\dot{\psi}_c$, $\dot{d}_c$) as shown in Fig. 6.4 where the user changes the velocity reference by mouse movement during the experiments. Also, the block allows the user to enter the constant velocity references when required. For instance, the robot follows the trajectory with constant velocity $4\ \frac{deg}{s}$ when the user adjusts and holds the slider block's cursor at 4. By integrating these values, the position references of task space variables are calculated and sent to the STM32 discovery board.

6.3. Experiments for Interacting with Soft Tissue

In this surgical scenario, the surgeon commands the teleoperated co-worker robot without physical interaction. For instance, in the surgery for the pituitary tumors, NeuRoboScope inserts into the surgical workspace through the nasal cavity for monitoring the tumor on the pituitary gland and interacts with the soft tissues of the nasal concha as represented in Fig. 6.5.

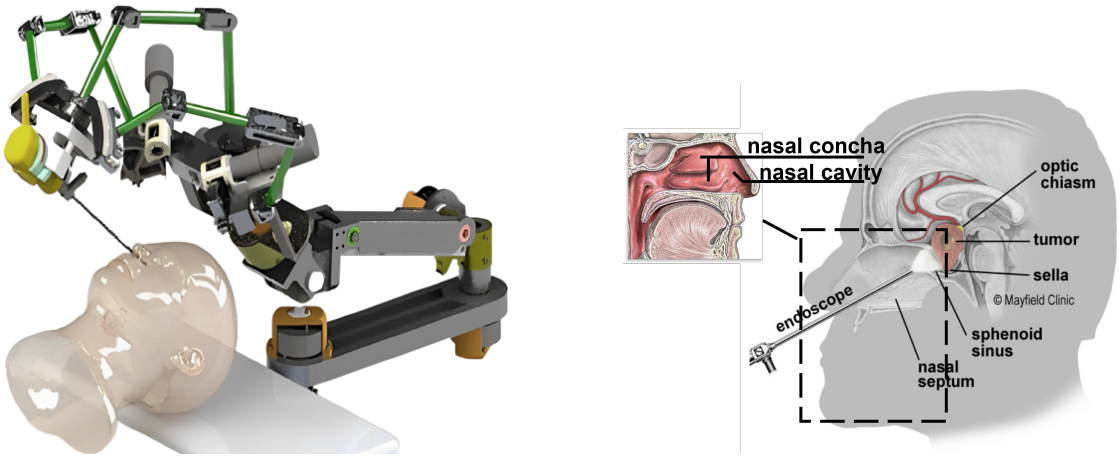

(a) NeuRoboScope during the operation

(b) Endoscope and its environment

Figure 6.5. The surgical robotic operation for removing tumor on the pituitary gland by using the NeuRoboScope

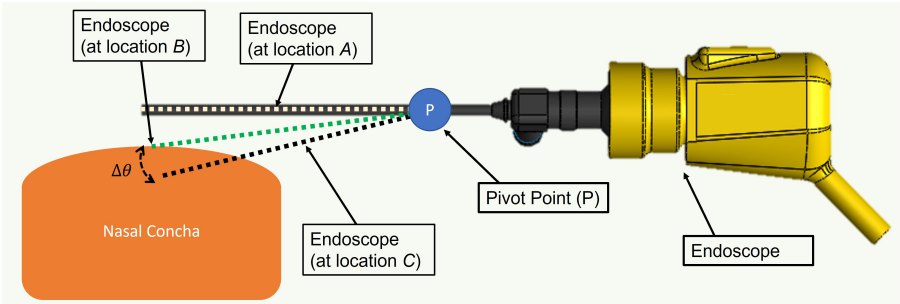

Figure 6.6. The interaction scenario between the endoscope and the soft tissues of the nasal concha

In Fig. 6.6, the interaction scenario between the endoscope and the soft tissues of the nasal concha is presented where the robot moves the endoscope around pivot point P. There is no interaction between the robot and its environment when the endoscope is

located between locations A and B. The interaction initially occurs at location B. It is assumed that the applied interaction torques do not harm the environment when the endoscope is located between the locations B and C. The endoscope applies T_{max} (which refers to the permissible maximum torque value during operation according to the surgeon's experience.) on soft tissues when the endoscope is moved to location C. Moreover, the interaction causes irreversible damage in the soft tissues when the interaction torque value is greater than T_{max}.

The surgeon commands the NeuRoboScope by given speed references $\bar{X}_c = \begin{bmatrix} \dot{\phi}^{des} & \dot{\psi}^{des} & \dot{d}^{des} \end{bmatrix}^T$. The environment cannot constraint the translational motion $\dot{d}$ of the endoscope along the $\vec{W}$ defined in Fig. 3.3 while the rotational motion $\dot{\phi}$ and $\dot{\psi}$ can be constrained by the environment. The given maximum speed value for both $\dot{\phi}^{des}$ and $\dot{\psi}^{des}$ is $\dot{X}_{c,max}$. The surgeon's arbitrary speed command for the NeuRoboScope is presented in Fig. 6.7 where the $\dot{X}_{c,max}$ is reached at t_1 and t_3.

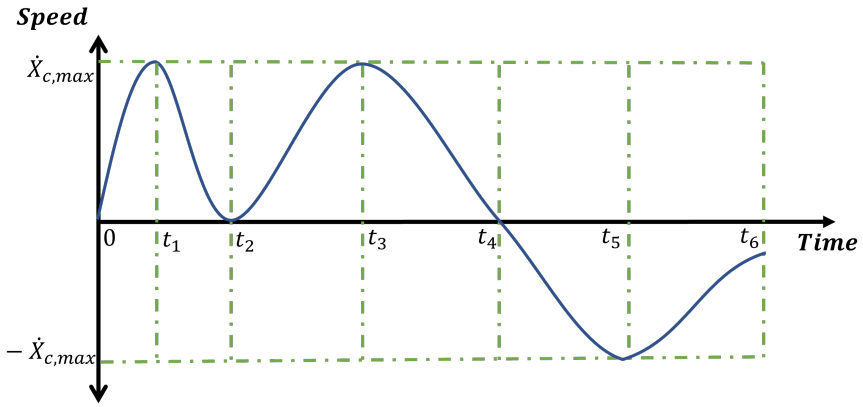

Figure 6.7. The surgeon's arbitrary speed command for the NeuRoboScope

According to the surgeon's arbitrary speed commands in Fig. 6.7, the location of the endoscope is presented in Fig. 6.6 and 6.8. The endoscope moves in free space between 0 and t_2, and during this interval, the interaction torque value equals $0\ Nm$ as observed in Fig. 6.9. The interaction with the soft tissues initially occurs at t_2 where the endoscope moved at location B. The interaction torques between t_2 and t_3 cannot harm the surgical environment. After t_3, where the maximum interaction torque value is reached, the surgeon's speed is still a positive value; however, decreasing. Therefore, the robot maintains the endoscope moving into the soft tissue. This action results in extreme interaction torques, which might harm the soft tissues, and this level of interaction torques is positioned in the hazardous zone in Fig. 6.9. Between t_3 and t_5, the extreme

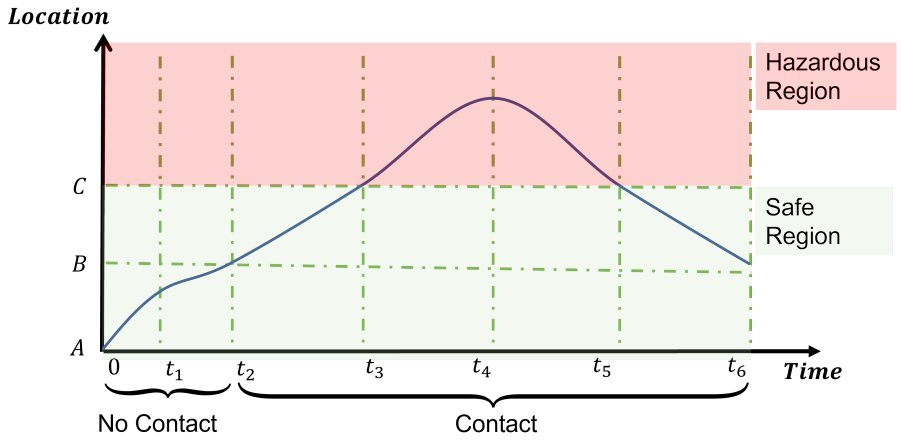

Figure 6.8. The changes in the endoscope's location according to the given surgeon's speed command when the motion controller is only implemented in the NeuRoboScope

interaction torques are applied. The endoscope is moved out of the soft tissue when the speed command given by the surgeon gets a negative value.

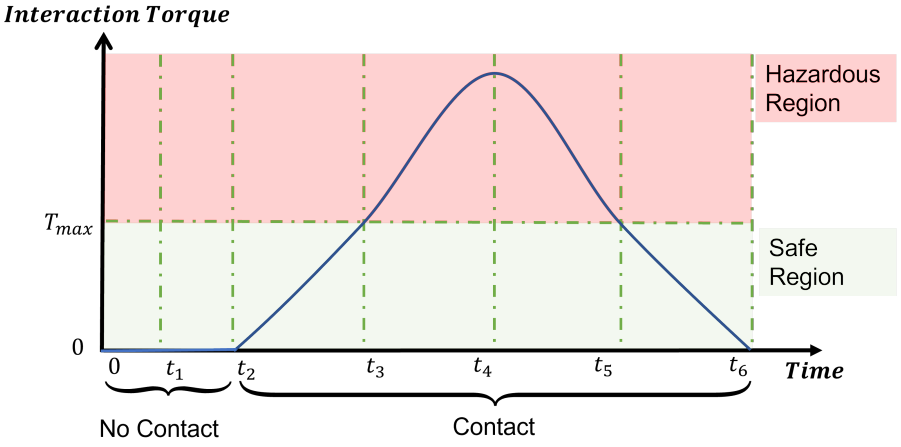

Figure 6.9. The interaction torque between the endoscope and the soft tissues according to the given surgeon's speed command when the motion controller is only implemented in the NeuRoboScope

As observed in Fig. 6.9, the extreme interaction torques between the endoscope and the soft tissues are undesired due to result in a hazardous situation for surgical operation. To avoid the extreme interaction torques, impedance and hybrid position/force controllers are designed and implemented in the NeuRoboScope.

6.3.1. Experiments for Soft Tissue Interaction Using Impedance Controller

To achieve a safe interaction, a compliant control algorithm must be designed. In this scenario, a design criterion of the controller to avoid applying extreme interaction torques is determined as that the surgeon' maximum speed command generates the maximum interaction torque value. This criterion makes the interaction torque not exceed the T_{max}. To realize this criterion, the desired relation between the interaction torques and the surgeon's speed command must be designed. A desired interaction torque profile is designed in Fig. 6.11 corresponding to the surgeon's speed command profile in Fig. 6.7. The surgeon's speed command initially reached a maximum speed at t_1 when the endoscope is located between locations A and B as observed in Fig. 6.10. In this region, there is no contact between the endoscope and the soft tissues; for that reason, the interaction torque is not observed. The contact occurs at t_2, and the surgeon's speed command reaches the $\dot{X}_{c,max}$ at t_4 again while the endoscope has interacted with the soft tissue. At t_4, the maximum speed command $\dot{X}_{c,max}$ generates the maximum interaction torque T_{max}. During contact, the interaction torque is also desired to be $0\ Nm$ when the surgeon's speed command equals $0\ \frac{rad}{s}$.

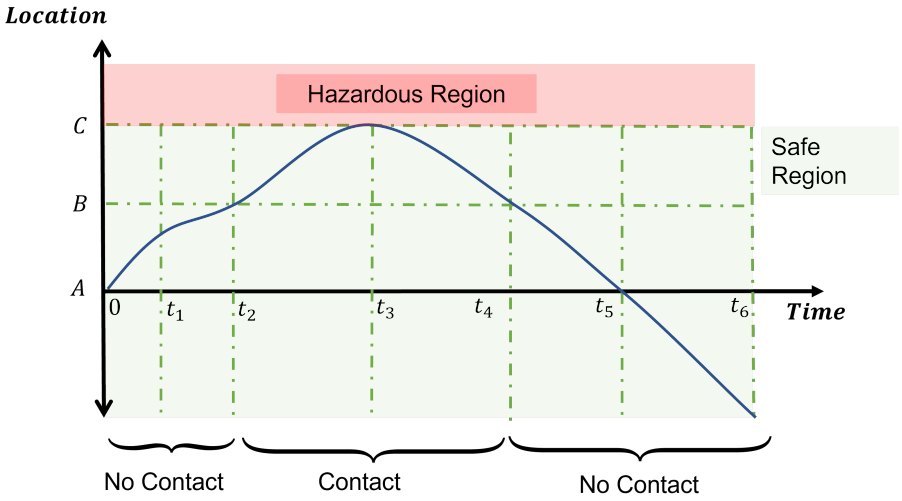

Figure 6.10. The changes in the endoscope's location according to the given surgeon's speed command when an active compliant controller is implemented in the NeuRoboScope

In this scenario, the impedance (the desired relation between torque and the surgeon's speed command) must be regulated to achieve a safe interaction. Also, the sur-

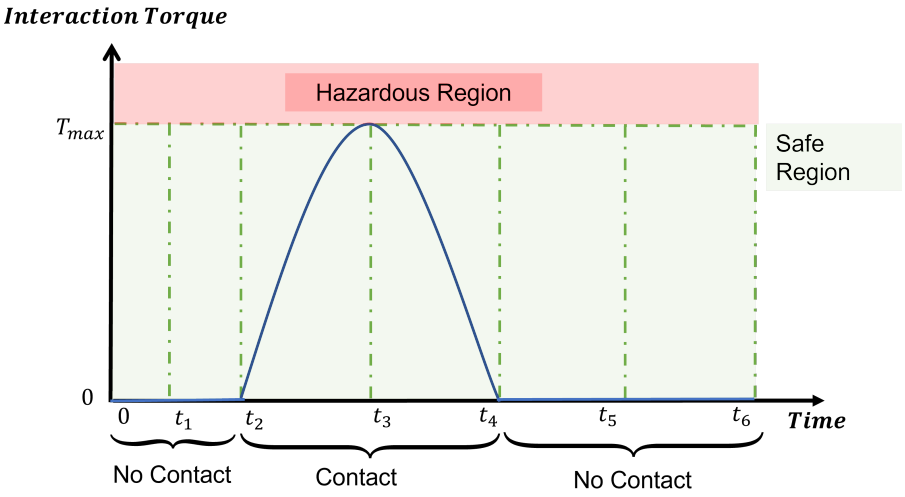

Figure 6.11. The interaction torque between the endoscope and the soft tissues according to the given surgeon's speed command when an active compliant controller is implemented in the NeuRoboScope

geon's speed command is the input of the system. Therefore, the proper active compliant control algorithm for this scenario is an impedance controller. It is designed according to the desired criterion mentioned above to obtain safe interaction between the endoscope attached to the NeuRoboScope's end-effector and the soft tissues of the nasal concha.

The design criteria of the controller is presented as follows.

✓ Stability: The pole location of the system are checked.

✓ Robustness: The controller gains are designed to minimize the sensitivity function.

6.3.1.1. Impedance Controller Design

In Chapter 4, the motion control algorithms, such as computed torque controller and independent joint controller with gravity compensation, are designed and implemented in the NeuRoboScope. The experimental results show that the independent joint controller with gravity compensation performs better than the computed torque method with the simplified dynamic model. Due to that, the independent joint controller with gravity compensation is used as a low-level motion controller in the active compliant control algorithms. The NeuRoboScope with the independent joint controller with gravity compensation is presented in Fig. 6.12 where $\bar{X}$ and $\bar{\theta}$ are task space and joint space variables. $\bar{e}$, $\bar{u}$, $\bar{T}$, and $\bar{T}_{ext}$ are error, control input, torques applied by actuators, and

external torque matrices, respectively. $\hat{\mathbb{C}}_p$, $\hat{P}$, and $\hat{J}_n$ blocks refer to the independent joint motion controller with gravity compensation, the plant which contains the dynamics of the NeuRoboScope with actuation systems, and Jacobian matrix. $()_d$, $\dot{()}$, and $()^{-1}$ refer to a desired matrix, the derivative of a matrix with respect to time, and the inverse of the matrix.

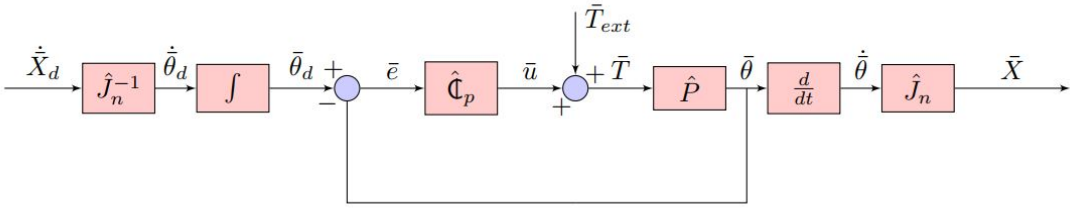

Figure 6.12. Motion controller scheme in task space

Since the relatively higher reduction ratio decreases the effect of $\hat{T}_{ext}$ on the actuation system, $\hat{T}_{ext}$ is neglected. The independent joint controller with gravity compensation cancels the NeuRoboScope's gravitational effect on the actuation systems by calculating the simplified gravitational torque matrix. Also, the velocity and acceleration-related terms of the NeuRoboScope's dynamics are neglected due to having a relatively low effect on the system compared to actuation dynamics. The independent joint controller is designed as a PD controller concerning the actuation dynamics as explained in Chapter 4. Therefore, the NeuRoboScope system, including the motion controller, and the dynamics of the NeuRoboScope with actuation system is derived linearly as $\hat{G}$ where input is $\dot{\bar{X}}_d$ and output is $\dot{\bar{X}}$. Moreover, $\hat{G}$ is defined as $G(s)\hat{1}$ and $G(s)$ is designed below.

$$G(s) = \frac{0.99s + 56.82}{0.0351s^2 + 1.99s + 56.82} \tag{6.1}$$

The block diagram in Fig. 6.13 presents the impedance controller designed in Section 6.3.1 where the $\hat{G}$ implies the low-level motion controller. In this block diagram, $\hat{Z}_e$ and $\hat{Y}$ blocks refer to the MIMO transfer function of the environment and admittance gain, respectively. $\bar{X}_c$, $\bar{X}_m$, and $\bar{F}_m$ are command motion state given by the surgeon, output state of admittance gain, and measured force/torque values from F/T sensor, respectively. $\dot{\bar{X}}_c$ is defined as $\begin{bmatrix}\dot{\phi}_c & \dot{\psi}_c & \dot{d}_c\end{bmatrix}^T$. As known from the NeuRoboScope design criteria, the interaction does not occur along the endoscope; therefore, $\bar{F}_m$ is defined as $\begin{bmatrix}T_{m,\phi} & T_{m,\psi} & 0\end{bmatrix}^T$. In addition, $\hat{Z}_e = Z_e(s)\hat{1}$ and $Z_e(s) = \frac{k_{soft}}{s}$. k_{soft} refers to the soft

silicon specimen's elastic model parameter. As explained in section 6.1, the elastic model parameter is calculated as $752.69\ \frac{N}{m}$ and the interaction between the robot and its environment occurs at a contact point on the endoscope in experimental studies. The distance between the contact point and the F/T sensor is measured as $\approx 240\ mm$. Therefore, the $k_{soft} = 747.1461\ \frac{N}{m}\frac{0.24m}{\frac{rad}{0.24m}} \approxeq 43.0356\frac{Nm}{rad}$.

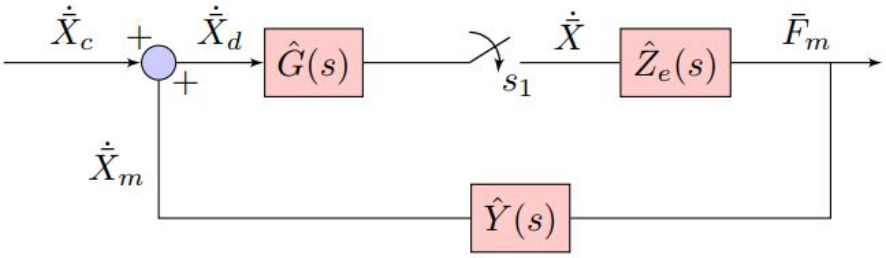

Figure 6.13. Impedance controller scheme in task space

The maximum speed of a surgeon's hand during operation is measured as $55.5\ ^\circ/\mathrm{s}$, which is rarely achieved. Another trusted speed value is measured as $8\ ^\circ/\mathrm{s}$. This value is used as the maximum surgeon's speed command $\dot{\bar{X}}_c$ for designing the active compliant control algorithm of the teleoperated surgical co-worker robot. Moreover, Freund (1986) states that a human moves his/her fingers or hand with $6 - 12\ Hz$; however, human eyes cannot track the object which moves with more than $2\ Hz$. Therefore, the maximum frequency of the surgeon's hand is chosen as $2\ Hz$.

For the design of the impedance controller, the desired impedance is determined by using maximum interaction torque and surgeon speed command.

$$Z_{des}(j\omega) = \frac{T_{max}}{\dot{X}_{c,max}} = \frac{0.3}{8}\frac{180}{pi} = 2.1486\frac{Nms}{rad} \tag{6.2}$$

The impedance displayed by the NeuRoboScope is $\hat{Z}_{disp}$ is defined as $Z_{disp}(s)\hat{1}$ and Z_{disp} is derived below.

$$Z_{disp}(s) = \frac{G(s)Z_e(s)}{1 + G(s)Z_e(s)Y(s)} \tag{6.3}$$

The performance cost function is defined as;

$$C_D = \sum_{f_{c,min}}^{f_{c,max}} |log(\|Z_{des}(j\omega)\|) - log(\|Z_{disp}(j\omega)\|)| \tag{6.4}$$

where $f_{c,max} = 12.57\frac{rad}{s}\ (= 2Hz)$ & $f_{c,min} = 0\ \frac{rad}{s}$

The sensitivity function of the NeuRoboScope is $\hat{L} = L(s)\hat{1}$ and $L(s)$ is;

$$L(s) = \frac{1}{1 + G(s)Z_e(s)Y(s)} \tag{6.5}$$

The cost function of the robustness is designed as follows;

$$C_R = \sum_{f_{c,min}}^{f_{c,max}} \|L(j\omega)\| \tag{6.6}$$

The cost function is defined as

$$C = 0.5C_D + 0.5C_R \tag{6.7}$$

where the robustness and performance have same weight on the cost function.

Generally, the admittance gain is chosen as a mass-spring-damper system; however, the spring K_t forces the robot to return to the position's equilibrium point, which is not desired for surgical operation. Therefore, the admittance gain is chosen as follows.

$$Y(s) = \frac{s}{M_t s^2 + B_t s} \tag{6.8}$$

The optimization problem is obtained as;

$$\underset{\substack{\omega \in [f_{c,min}, f_{c,max}] \\ B_t \in R \\ M_t \in R}}{\text{minimize}} \; C(j\omega) \tag{6.9}$$

By minimizing the cost function, the values are obtained as $M_t = 0$ and $B_t = 2.15$. It is known that the impedance controller is a robust compliant controller. When there is no collision or contact (Switch s_1 is opened in Fig. 6.13.), $F_m = 0$ therefore, $\dot{X} = 0$. When there is collision or contact (Switch s_1 is closed.), $F_m \neq 0$ therefore, $\dot{X} \neq 0$. As a result, there is no discontinuity when the impedance control is applied. Due to that, the system's poles are searched in the system's stability where switch s_1 is closed and the system is stable when $M_t = 0$ and $B_t = 2.15$.

6.3.1.2. Experimental Study

In all experiments, the initial position of the NeuRoboScope is chosen as $\phi \approxeq 0°$, $\psi \approxeq 0°$, and $d \approxeq 150\ mm$ where surgery is performed in the actual surgical scenario.

In the first experiment, the $\dot{\phi}_c$ is changed when $\dot{\psi}_c$ and $\dot{d}_c$ are kept as $0\ \frac{rad}{s}$ and $0\ \frac{mm}{s}$, respectively. Therefore, the robot moves the endoscope in and out of the soft silicon

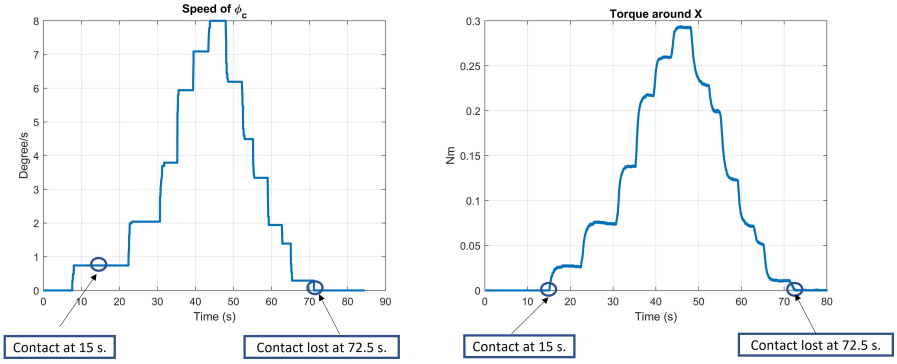

Figure 6.14. The command speed of ϕ and the interaction torque when the NeuRoboScope interacts with the soft silicon specimen

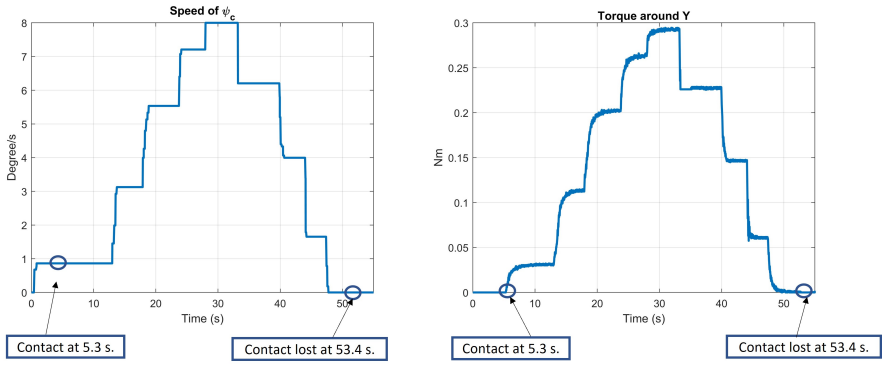

Figure 6.15. The command speed of ψ and the interaction torque when the NeuRoboScope interacts with the soft silicon specimen

specimen. As observed in Fig. 6.14, the NeuRoboScope does not interact with the soft silicon specimen at the initial of the experiment, and the interaction occurs at $t = 15\ s$. The impedance is measured as $2.1372\ \frac{Nms}{rad}$ at $26\ s$, $2.0997\ \frac{Nms}{rad}$ at $46\ s$, and $2.1766\ \frac{Nms}{rad}$ at $57\ s$ where desired impedance is $2.1486 \frac{Nms}{rad}$. The RMSE between desired and measured impedance is calculated during the experiment as $0.0595\ \frac{Nms}{rad}$.

In the second experiment, the location of the soft silicon specimen is changed. The robot moves the endoscope in and out of the soft silicon specimen by changing the value of $\dot{\psi_c}$ while $\dot{\phi_c}$ and $\dot{d_c}$ are kept as $0\ \frac{rad}{s}$ and $0\ \frac{mm}{s}$, respectively. Therefore, as observed in Fig. 6.15, the NeuRoboScope does not interact with the soft silicon specimen at the initial of the experiment, and the interaction occurs at $t = 5.3\ s$. The impedance is measured as $2.0494\ \frac{Nms}{rad}$ at $20\ s$, $2.0883\ \frac{Nms}{rad}$ at $30\ s$, and $2.1131\ \frac{Nms}{rad}$ at $43\ s$ where desired impedance is $2.1486 \frac{Nms}{rad}$. During the experiment, the RMSE between desired and measured impedance is calculated as $0.0444\ \frac{Nms}{rad}$.

6.3.2. Experiments for Soft Tissue Interaction Using Impedance Controller with Increased Agility

In previous study, the safe interaction between the endoscope and the soft tissues is provided by implementing the impedance controller. It regulates the relation between $\dot{\bar{X}}_c$ and $\bar{F}_m$ in Fig. 6.13 to keep interaction torques in the safe region as observed in Fig. 6.11. The interaction torques close to the hazardous zone when the NeuRoboScope moves the endoscope into the soft tissue (moving the endoscope location B to C as represented in Fig. 6.6). Moreover, the interaction torques get extreme values as observed in Fig. 6.9 (inserted into the hazardous zone) when the compliant controller is not implemented; however, the endoscope is getting far from the hazardous zone when the NeuRoboScope moves the endoscope out of the soft tissues (moving endoscope location C to B). It is inferred that moving the endoscope out of the soft tissues is a naturally safe action. According to this inference, the relation between the surgeon's speed command and interaction torque can be regulated concerning the improvement in the system's agility (decreasing the execution time of completing the task) rather than conservatively providing safe interaction for moving the endoscope out the soft tissues.

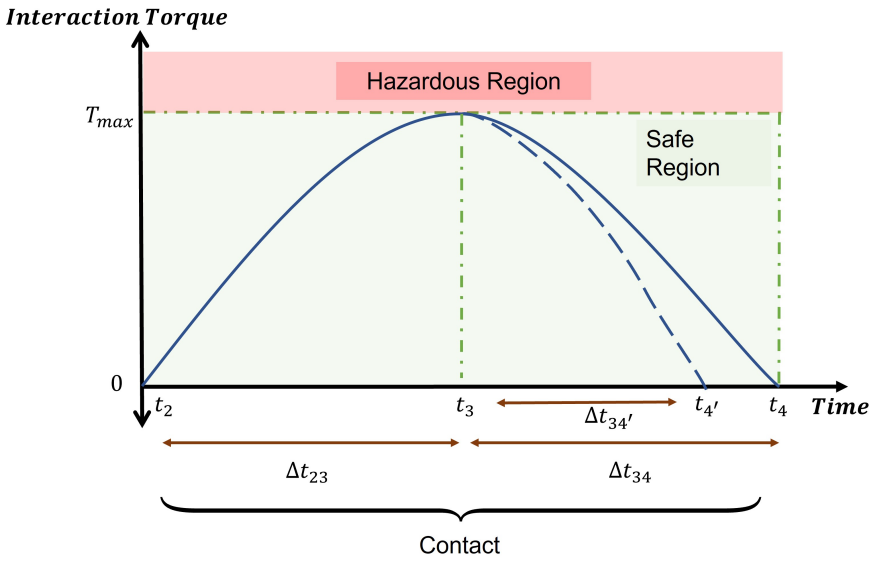

Figure 6.16. The desired interaction torque profile for improving the agility

Fig. 6.16 presents the desired interaction torque profile between t_2 and t_4 of previous study ($Straight - Line$) defined in Fig 6.11 and the desired interaction torque profile for improving the agility ($Dashed - Line$) where the NeuRoboScope moves the endo-

scope into the soft tissue between t_2 and t_3 and moves the endoscope out of the tissue after t_4. The desired interaction torque profile between t_2 and t_3 behaves as same as the desired interaction in the previous study where the design criterion of the controller is that the surgeon's maximum speed command generates the maximum interaction torque value; therefore, the interaction torque does not exceed the T_{max} and the controller provides safe interaction. When the desired interaction torque profile between t_3 and t_4 for previous and current studies are compared, it is observed that the action for moving the endoscope out of the soft tissues is completed in Δt_{34} for the previous study and in $\Delta t_{34'}$ for this study where $\Delta t_{34'} < \Delta t_{34}$. According to the desired torque profile, a designed criterion in addition to the criterion defined in the previous study is defined as that the system's impedance must be modified when moving the endoscope out of the soft tissue to improve the agility by decreasing the execution time Δt_{34} to $\Delta t_{34'}$.

To perform the designed criteria, the impedance controller is the proper active compliant control algorithm for this scenario, and the desired impedance is changed according to the actions. Therefore, agility is improved by providing a safe interaction between the endoscope attached to the NeuRoboScope's end-effector and the soft tissues of the nasal concha.

The design criteria of the controller is presented as follows.

- ✓ Stability: The pole location of each system and stability of the switched systems are checked.
- ✓ Robustness: The controller gains are designed to minimize the sensitivity function.
- ✓ Agility: The execution time of the tasks is improved.

6.3.2.1. The Design of the Impedance Controller with Increased Agility

Fig 6.17 presents the impedance control scheme where s_1 and s_2 refer to switches. Switch s_1 is closed when contact has occurred. In contrast, switch s_1 is opened when contact is lost. When the robot moves the endoscope into the tissue, the admittance gain Y_1 becomes active, and Y_2 becomes disabled. However, the admittance gain Y_2 becomes active when the robot moves the endoscope out of the tissue. The optimum parameter of Y_1 can be chosen as the optimum parameter used in Section 6.3.1 where $M_t = 0$ and $B_t = 2.15$. However, the parameter M_t cannot be equal to zero due to the stability of

switched systems. By considering the $M_t \neq 0$, the Y_1 is redesigned by applying the same method in Section 6.3.1, and the optimum parameters of Y_1 are derived as $M_t = 0.01$ and $B_t = 2.15$ where the desired impedance is $2.1486 \frac{Nms}{rad}$. To improve execution time when moving the endoscope out of tissue, the desired impedance of Y_2 is chosen as $1.0743 \frac{Nms}{rad}$, which is half of Y_1's target impedance. By applying the same method in Section 6.3.1, the optimum parameters of Y_2 are calculated as $M_t = 0.01$ and $B_t = 1.04$.

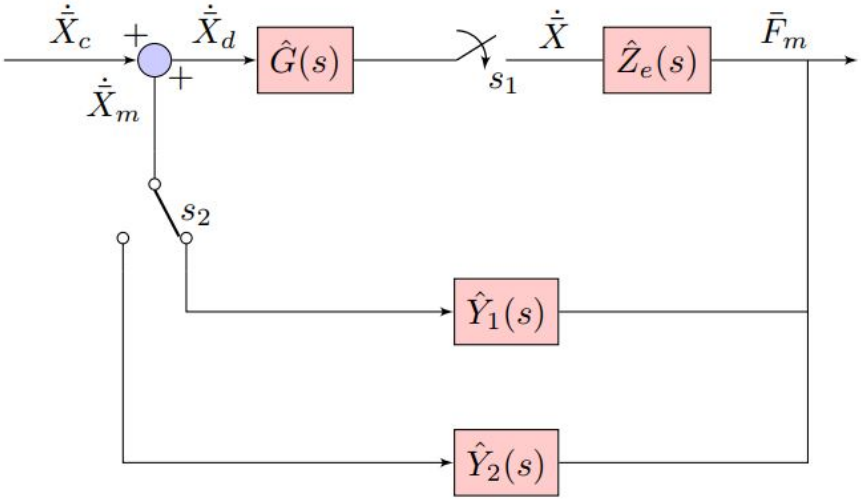

Figure 6.17. Impedance controller scheme with switching between the admittance gains

6.3.2.2. Stability Analysis of the Switched Systems

It is assumed that the robot's motion through each axis shows the same behavior, and it will be valid for other DOFs if the stability is proven in a DOF of the system.

To derive the state space representation of the $G(s) = \frac{0.99s+56.82}{0.0351s^2+1.99s+56.82}$, the input and output states are defined as;

$$\text{State } \chi_p\text{: } \xrightarrow{\text{Input } U_p\text{: } \dot{X}_c} \text{Output } Y_p\text{:}\dot{X} \tag{6.10}$$

$$\dot{\chi}_p = A_p\chi_p + B_pU_p \tag{6.11}$$

$$Y_p = C_p\chi_p + D_pU_p \tag{6.12}$$

where $A_p = \begin{bmatrix} 0 & 1 \\ -1618.80 & -56.89 \end{bmatrix}$, $B_p = \begin{bmatrix} 0 \\ 1 \end{bmatrix}$, $C_p = \begin{bmatrix} 1618.80 & 28.4160 \end{bmatrix}$ & $D_p = \begin{bmatrix} 0 \end{bmatrix}$.

Therefore, the state space representation of $G(s)$ is defined as;

$$\dot{\chi}_p = A_p\chi_p + B_pU_p \tag{6.13}$$

$$Y_p = C_p\chi_p \tag{6.14}$$

State space representation of $Z_e(s)$ are defined below where $\frac{Z_e(s)}{s} = k_{soft}X$ and $k_{soft} = 43.0356\frac{Nm}{rad}$.

$$\text{State } \chi_z\text{: } \xrightarrow{\text{Input } U_z\text{: } \dot{X}} \text{Output } Y_z\text{:}F_m \tag{6.15}$$

$$\dot{\chi}_z = A_z\chi_z + B_zU_z \tag{6.16}$$

$$Y_z = C_z\chi_z + D_zU_z \tag{6.17}$$

where $A_z = \begin{bmatrix}0\end{bmatrix}$, $B_z = \begin{bmatrix}43.0356\end{bmatrix}$, $C_z = \begin{bmatrix}1\end{bmatrix}$ & $D_z = \begin{bmatrix}0\end{bmatrix}$. Therefore, the state space representation of $Z_e(s)$ is defined as;

$$\dot{\chi}_z = A_z\chi_z + B_zU_z \tag{6.18}$$

$$Y_z = C_z\chi_z \tag{6.19}$$

State space representation of $Y(s) = \frac{s}{M_ts^2+B_ts}$ is defined as;

$$\text{State } \chi_c\text{: } \xrightarrow{\text{Input } U_c\text{:}F_m} \text{Output } Y_c\text{:}X_m \tag{6.20}$$

$$\dot{\chi}_c = A_c\chi_c + B_cU_c \tag{6.21}$$

$$Y_c = C_c\chi_c + D_cU_c \tag{6.22}$$

where $A_c = \begin{bmatrix}-\frac{B_t}{M_t}\end{bmatrix}$, $B_c = \begin{bmatrix}-\frac{1}{M_t}\end{bmatrix}$, $C_c = \begin{bmatrix}1\end{bmatrix}$ & $D_c = \begin{bmatrix}0\end{bmatrix}$. Therefore, the state space representation of $Y(s)$ is defined as;

$$\dot{\chi}_c = A_c\chi_c + B_cU_c \tag{6.23}$$

$$Y_c = C_c\chi_c \tag{6.24}$$

System 1 is defined when admittance gain Y_1 is active and Y_2 is disabled. System 2 is defined when admittance gain Y_2 is active and Y_1 is disabled.

For System 1 & 2; state $\chi = \begin{bmatrix}\chi_p\\ \chi_c\\ \chi_z\end{bmatrix}$

$$\dot{\chi}_p = A_p\chi_p + B_p(\dot{X}_c - C_c\chi_c) \tag{6.25}$$

$$\dot{\chi}_c = A_c\chi_c + B_cC_z\chi_z \tag{6.26}$$

$$\dot{\chi}_z = A_z X_z + B_z C_p \chi_p \tag{6.27}$$

State space of the system 1 and 2;

$$\dot{\chi} = A_{1,2}\chi + B_{1,2}\varsigma \tag{6.28}$$

$$Y = C_1 \chi \tag{6.29}$$

where $A_{1,2} = \begin{bmatrix} A_p & -B_p C_c & \hat{0} \\ \hat{0} & A_c & B_c C_Z \\ B_z C_p & 0 & A_z \end{bmatrix}$, $B_{1,2} = \begin{bmatrix} B_p \\ \hat{0} \\ \hat{0} \end{bmatrix}$ & $\varsigma = \begin{bmatrix} \dot{X}_c \end{bmatrix}$. $C_{1,2} = \begin{bmatrix} C_p & \hat{0} & \hat{0} \end{bmatrix}$

With numerical values, $A_1 = \begin{bmatrix} 0 & 1 & 0 & 0 \\ 1618.80 & -56.89 & -1 & 0 \\ 0 & 0 & -215 & 100 \\ 70183.13 & 1231.97 & 0 & 0 \end{bmatrix}$ where $M_t = 0.01$ and $B_t = 2.15$. and $A_2 = \begin{bmatrix} 0 & 1 & 0 & 0 \\ 1618.80 & -56.89 & -1 & 0 \\ 0 & 0 & -104 & 100 \\ 70183.13 & 1231.97 & 0 & 0 \end{bmatrix}$ where $M_t = 0.01$ and $B_t = 1.04$. B_1 and B_2, also C_1 and C_2 are same. B_1 and B_2 are bounded and A_1 and A_2 are $Hurwitz$ matrices; therefore, the common Lyapunov function is searched as explained in Section 5.1.1.1. As a result, the system is stable under arbitrary switching in the sense of Lyapunov.

6.3.2.3. Experimental Study

In all experiments, the initial position of the NeuRoboScope is chosen as $\phi \approxeq 0°$, $\psi \approxeq 0°$, and $d \approxeq 150\ mm$ where surgery is performed in an actual surgical scenario.

In this experimental study, the robot inserts the endoscope into the soft silicon specimen and reaches the maximum torque value. Then, the robot moves the endoscope out of the tissue with a constant speed. These experiments are done by implementing the impedance controller with switching its parameters. The execution time of getting the endoscope out of the specimen is measured. The same experiment is done by implementing the impedance controller without switching its parameters to compare the designed controller's performance.

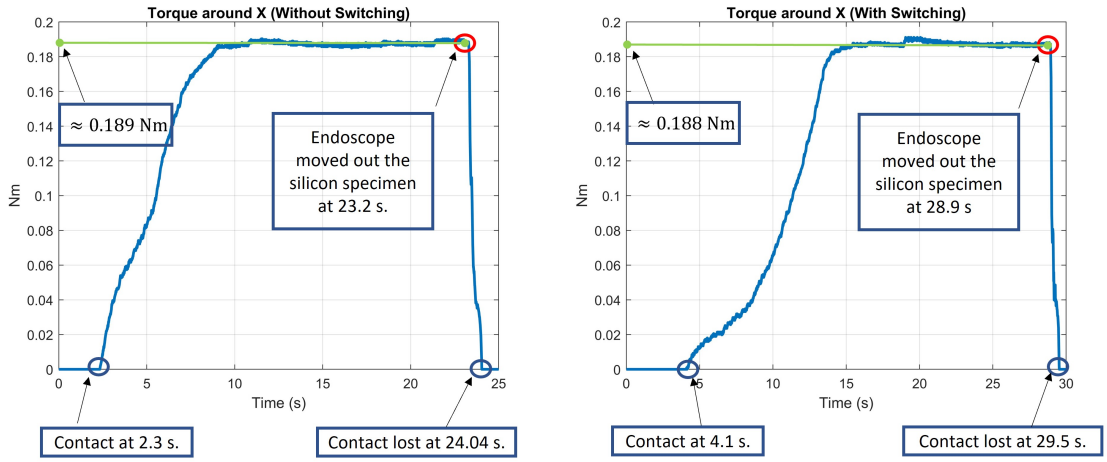

Figure 6.18. The torques values without switching (located left side) and the torques values with switching (located right side) when endoscope is moved out the soft silicon specimen with $\dot{\phi}_c = 0.0873\ \frac{rad}{s}$

In the first experiment, the $\dot{\phi}_c$ is changed when $\dot{\psi}_c$ and $\dot{d}_c$ are kept as $0\ \frac{rad}{s}$ and $0\ \frac{mm}{s}$, respectively. Therefore, the endoscope moves into a soft silicon specimen with admittance gain Y_1 and moves out with $\dot{\phi}_c = 0.0873\ \frac{rad}{s}$. The results are shown in Fig. 6.18 where the execution times when moving the endoscope out of the specimen by implementing the impedance controller without switching are calculated as $0.75\ s$ and $0.61\ s$ by implementing the impedance controller with switching. The execution time is improved by 19% with the switching method.

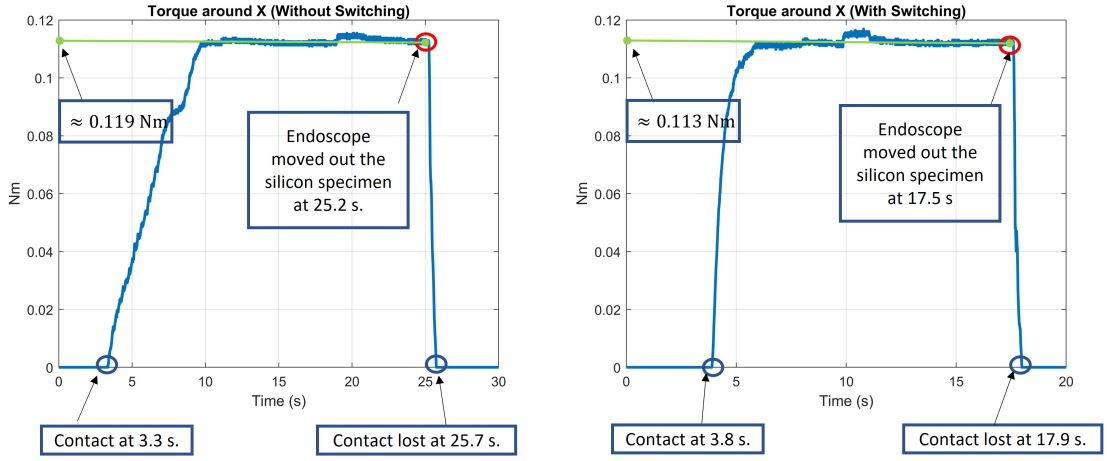

Figure 6.19. The torques values without switching (located left side) and the torques values with switching (located right side) when endoscope is moved out the soft silicon specimen with $\dot{\phi}_c = 0.0524\ \frac{rad}{s}$

In the second experiment, the $\dot{\phi}_c$ is changed when $\dot{\psi}_c$ and $\dot{d}_c$ are kept as $0\ \frac{rad}{s}$ and $0\ \frac{mm}{s}$, respectively. Therefore, the endoscope moves into a soft silicon specimen with admittance gain Y_1 and moves out with $\dot{\phi}_c = 0.0524\ \frac{rad}{s}$. The results are shown in Fig. 6.19 where the execution times when moving the endoscope out of the specimen are calculated as $0.53\ s$ by implementing the impedance controller without switching and $0.41\ s$ by implementing the impedance controller with switching. The execution time is improved by 21% with the switching method.

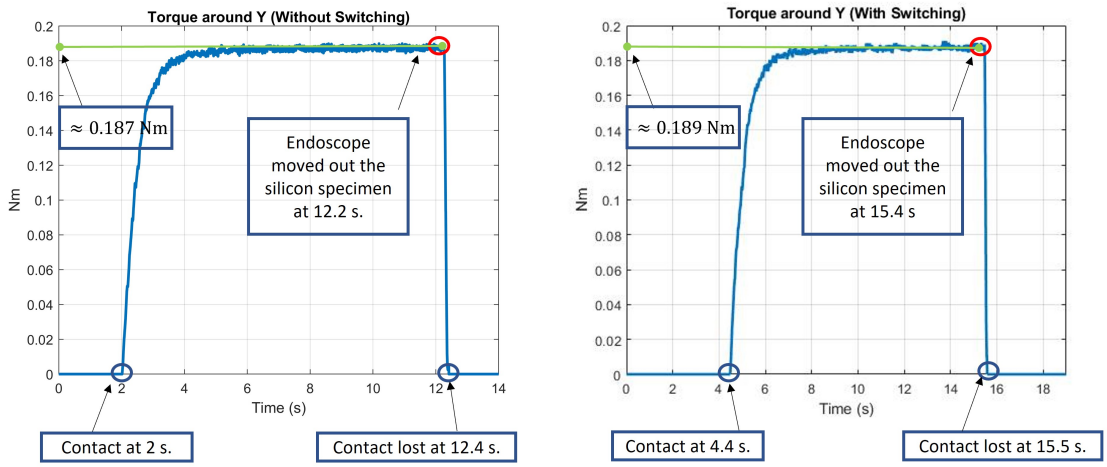

Figure 6.20. The torques values without switching (located left side) and the torques values with switching (located right side) when endoscope is moved out the soft silicon specimen with $\dot{\psi}_c = 0.0873\ \frac{rad}{s}$

In the third experiment, the $\dot{\psi}_c$ is changed when $\dot{\phi}_c$ and $\dot{d}_c$ are kept as $0\ \frac{rad}{s}$ and $0\ \frac{mm}{s}$, respectively. Therefore, the endoscope moves into a soft silicon specimen with admittance gain Y_1 and moves out with $\dot{\phi}_c = 0.0873\ \frac{rad}{s}$. The results are shown in Fig. 6.20 where the execution times when moving the endoscope out of the specimen are calculated as $0.09\ s$ by implementing the impedance controller without switching and $0.07\ s$ by implementing the impedance controller with switching. The execution time is improved by 20% with the switching method.

In the fourth experiment, the $\dot{\psi}_c$ is changed when $\dot{\phi}_c$ and $\dot{d}_c$ are kept as $0\ \frac{rad}{s}$ and $0\ \frac{mm}{s}$, respectively. Therefore, the endoscope moves into a soft silicon specimen with admittance gain Y_1 and moves out with $\dot{\phi}_c = 0.0524\ \frac{rad}{s}$. The results are shown in Fig. 6.21 where the execution times when moving the endoscope out of the specimen are calculated as $0.16\ s$ by implementing the impedance controller without switching and $0.13\ s\ s$ by implementing the impedance controller with switching. The execution time is improved by 20% with the switching method.

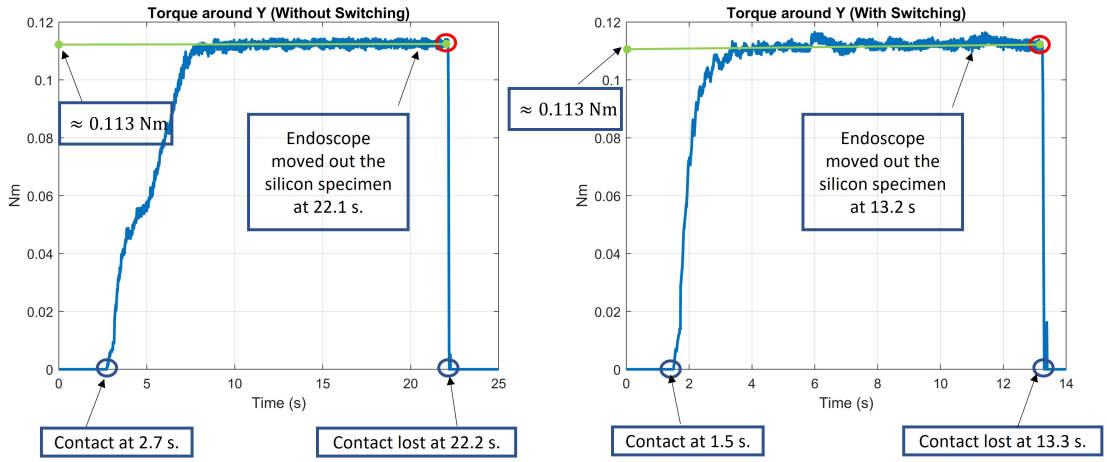

Figure 6.21. The torques values without switching (located left side) and the torques values with switching (located right side) when endoscope is moved out the soft silicon specimen with $\dot{\psi}_c = 0.0524\ \frac{rad}{s}$

As a result, the execution time of moving the endoscope out of the soft tissue is improved as $\approx 20\%$ by implementing the impedance controller with switching methodology, which changes the stiffness of system $2.1486 \frac{Nms}{rad}$ to $1.0743 \frac{Nms}{rad}$.

6.3.3. Experiments for Soft Tissue Interaction Using Hybrid Position/Force Controller

In previous studies, the impedance controller regulates the relation between the surgeon's speed command and interaction torques to avoid excessive interaction torque values, which might result in hazardous situations. In this study, the controller's purpose is to allow the robot to follow the given speed command when the interaction torque value is in the safe region. When the interaction torque value reaches a predefined threshold torque value T_{th} around the normal to the interaction surface, which implies that the interaction torque is close to a dangerous region, the controller is switched to the torque controller around the corresponding axis by modifying the $\hat{S}$ matrix in Fig. 6.23. By applying the torque controller, the interaction torques are kept at T_{th} in the safe region until the surgeon gives a speed command for moving the endoscope out of the tissue. This desired interaction profile according to the surgeon's speed command in Fig. 6.7 is presented in Fig. 6.22 where there is no interaction between 0 & t_1, and t_5 & t_6. The contact initially occurs at t_2, where the applied interaction torque values are positioned in the safe region.

The robot follows the given speed trajectory between t_2 and t_i until it reaches the T_h, although there is contact between the endoscope and the soft tissues. Between t_i and t_4, the interaction torque value is kept at T_h. At t_4, the speed trajectory gets the negative value; therefore, the robot starts to follow the speed trajectory again. At t_5, the contact is lost.

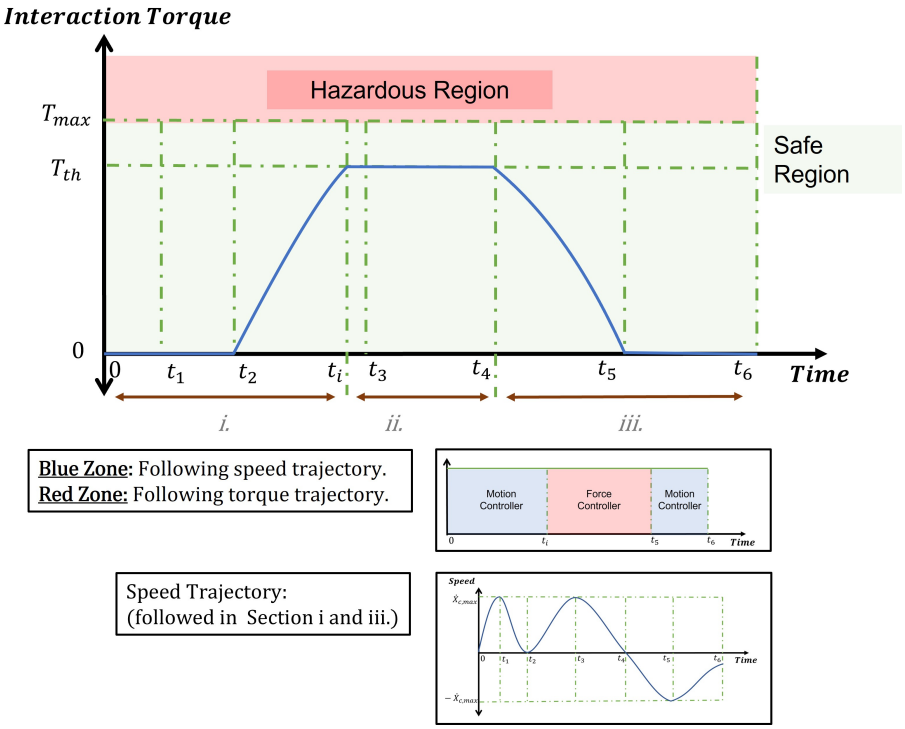

Figure 6.22. The desired interaction torque profile where pure torque controller is applied between t_i and t_4 and pure motion controller is applied between 0 and t_i, and t_4 and t_6

As a result, the desired criterion for the controller is that the robot follows the surgeon's speed command by applying a pure motion controller until the interaction torque reaches the T_h. Then, the motion controller switches to a torque controller for following the torque trajectory by the robot, and the torque controller is switched to the motion controller when the surgeon's speed command gets a negative value. Therefore, the interaction torques are limited with T_h to hold them in a safe region. For the NeuRoboScope, T_h is chosen as T_{max}.

In this study, the proper controller makes the robot follow the motion and torque trajectories independently, in contrast to the impedance and admittance controller. Therefore, the proper controller for limiting the interaction torques is chosen as a hybrid position/force controller. The arbitrary switching between motion and force controller is

required to satisfy the desired criterion.

The design criteria of the controller is presented as follows.

✓ Stability: The pole location of each system and stability of the switched systems are checked.

✓ Robustness: The controller gains are designed to minimize the sensitivity function.

6.3.3.1. Hybrid Position/Force Controller Design

Fig. 6.23 presents the traditional hybrid position/force control algorithm scheme where the force and position are controlled independently. The force controller part replaces with torque controller when implemented in the NeuRoboScope.

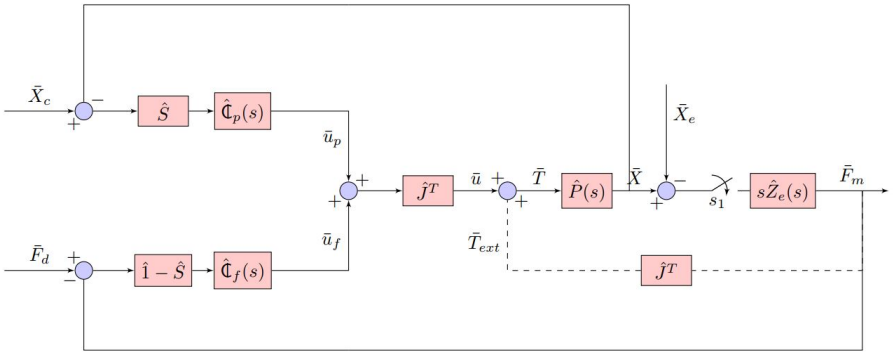

Figure 6.23. Hybrid position/force controller scheme

The diagonal $\hat{S}$ and its orthogonal complement $\hat{1} - \hat{S}$ matrices are designed to select the axes where the position control and torque control is implemented, respectively. In NeuRoboScope, $\hat{S}$ is defined as below where the position controller is applied for ϕ, ψ, and d when $S_\phi = 1$, $S_\psi = 1$ and $S_d = 1$ and the force controller is applied for ϕ, ψ, and d when $S_\phi = 0$, $S_\psi = 0$ and $S_d = 0$.

$$\hat{S} = \begin{bmatrix} S_\phi & 0 & 0 \\ 0 & S_\psi & 0 \\ 0 & 0 & S_d \end{bmatrix} \tag{6.30}$$

According to NeuRoboScope's design criteria, the contact between the endoscope and the tissue does not occur along the endoscope axis. Therefore, the position controller

is applied for d and $S_d = 1$. The force control algorithm is only active when the interaction torque values between the endoscope and the soft silicon specimen are reached to maximum torque value ($= 0.3\ Nm$) and $F_d = 0.3\ Nm$ in Fig. 6.23 for each direction. In this situation, the parameters S_ϕ and S_ψ are switched to 0 from 1. Moreover, the parameters S_ϕ and S_ψ are switched to 1 from 0 when NeuRoboScope moves the endoscope out of the tissue.

From the previous studies, the transfer function where input $\dot{X}_c$ and output $\dot{X}$ is derived as $\hat{G}(s)$ as shown in Eq. 6.1. In addition, the external torque is neglected due to the high reduction ratio in the actuation system. By using the $\hat{G}(s)$, the transfer function $\hat{H}(s)$ where input X_c and output X is derived as;

$$H(s) = \frac{sG(s)}{s} \tag{6.31}$$

where $\hat{H} = H(s)\hat{1}$.

By using $\hat{H}(s)$, the block diagram in Fig. 6.23 is modified as shown in Fig. 6.24 where input of $\hat{H}(s)$ is $\bar{X}_c$ for that reason, the $\hat{\mathbb{C}}_p(s) = \hat{1}$. $\dot{\bar{X}}_c$ refers to the surgeon's speed command column matrix. $\bar{X}_i$ refers to the initial condition column matrix when the switching in the selection matrix occurs.

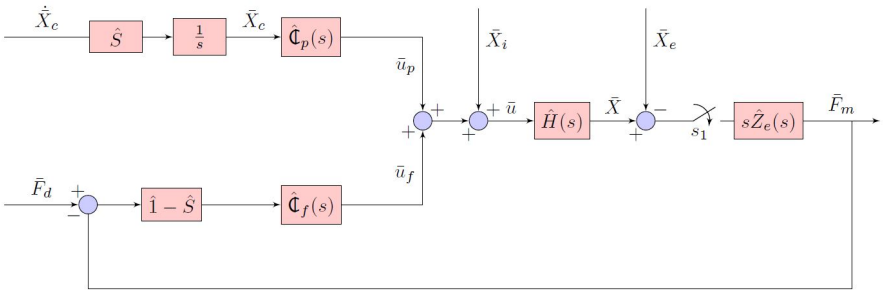

Figure 6.24. The block diagram of the hybrid position/force controller which is implemented in the NeuRoboScope

The system $H(s)$ is a type-0 system; therefore, a PI controller must be designed to deal with the steady-state error. However, the stability of switched systems is not guaranteed due to the integral term in this controller; for that reason, a P controller is designed.

$$u_f = K_p(F_d - F_m) \tag{6.32}$$

The open-loop transfer function $H(s)sZ_e(s)$is defined in Eq. 6.33 where $sZ_e(s) = k_{soft}(= 43.0356\frac{Nm}{rad})$.

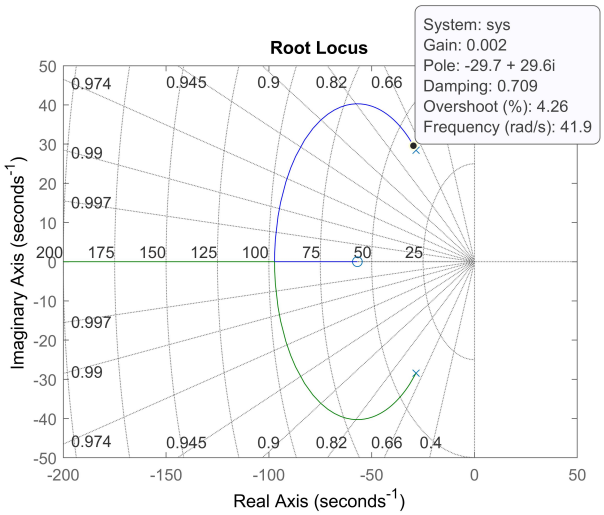

Figure 6.25. The root-locus of the open-loop model of the force control scheme

$$H(s)sZ_e(s) = \frac{42.92s + 2445}{0.0351s^2 + 1.997s + 56.82} \tag{6.33}$$

The performance criteria for the design of the P controller are determined as $\zeta = 0.707$ and $w_n = 40.2971\frac{rad}{s}$ as mentioned in Chapter 4. Fig. 6.25 presents the root-locus of the open-loop transfer function, and K_p is calculated as 0.02.

6.3.3.2. Stability Analysis of the Switched Systems

It is assumed that the robot's motion through each axis shows the same behavior, and it will be valid for other DOFs if the stability is proven in a DOF of the system.

To derive the state space representation of the $H(s) = \frac{0.99s+56.82}{0.0351s^2+1.99s+56.82}$, the input and output states are defined as;

$$\text{State } \chi_H\text{: } \xrightarrow{\text{Input } U_H\text{: } u_p + u_f + X_i} \text{Output } Y_H\text{:}X \tag{6.34}$$

$$\dot{\chi}_H = A_H\chi_H + B_HU_H \tag{6.35}$$

$$Y_H = C_H\chi_H + D_HU_H \tag{6.36}$$

where $A_H = \begin{bmatrix} 0 & 1 \\ -1618.80 & -56.89 \end{bmatrix}$, $B_H = \begin{bmatrix} 0 \\ 1 \end{bmatrix}$, $C_H = \begin{bmatrix} 1618.80 & 28.4160 \end{bmatrix}$ & $D_H = \begin{bmatrix} 0 \end{bmatrix}$. Therefore, the state space representation of $H(s)$ is defined as;

$$\dot{\chi}_H = A_H\chi_H + B_HU_H \tag{6.37}$$

$$Y_H = C_H \chi_H \tag{6.38}$$

From Fig. 6.24, the position and force control inputs are derived as:

$$u_p = SX_c \tag{6.39}$$

$$u_f = K_p(1-S)(F_d - F_m) \tag{6.40}$$

where $i = \phi, \psi$ and $F_m = k_{soft}(X - X_e)$ and the control input u is derived as;

$$u = SX_c + K_p(1-S)(F_d - k_{soft}(X - X_e)) + X_i \tag{6.41}$$

When Eq. 6.41 is combined with the Eq. 6.38,

$$\dot{\chi}_H = (A_H - B_H K_p(1-S)k_{soft}C)\chi_H + B_H(SX_c + K_p(1-S)F_d + K_p(1-S)k_{soft}X_e + X_i) \tag{6.42}$$

$$Y_H = C_H \chi_H \tag{6.43}$$

When the interaction force is not reached to the maximum value where $S = 1$, the state space representation of the system is represented as;

$$\dot{\chi}_H = A_H \chi_H + B_H(X_c + X_i) \tag{6.44}$$

$$Y_H = C_H \chi_H \tag{6.45}$$

When the interaction force is reached to the maximum value where $S = 0$, the state space representation of the system is represented as;

$$\dot{\chi}_H = (A_H - B_H K_p k_{soft} C)\chi_2 + B_H(K_p F_d + K_p k_{soft} X_e + X_i) \tag{6.46}$$

$$Y_H = C_H \chi_H \tag{6.47}$$

where $U_1 = (X_c + X_i)$ and $U_2 = (K_p F_d + K_p k_{soft} X_e + X_i)$ are bounded. $A_1 = A_H$ and $A_2 = (A_H - B_H K_p k_{soft} C)$ are $Hurwitz$ matrices; therefore, the common Lyapunov function is searched as explained in Section 5.1.1.1. As a result, the system is stable under arbitrary switching in the sense of Lyapunov.

6.3.3.3. Experimental Study

In all experiments, the initial position of the NeuRoboScope is chosen as $\phi \approxeq 0°$, $\psi \approxeq 0°$, and $d \approxeq 150\ mm$ where surgery is performed in the real surgical scenario. The

robot inserts the endoscope into the tissue with the speed command given by the user and reaches the maximum torque value. The designed torque controller becomes active while the position controller is deactivated for the specific direction.

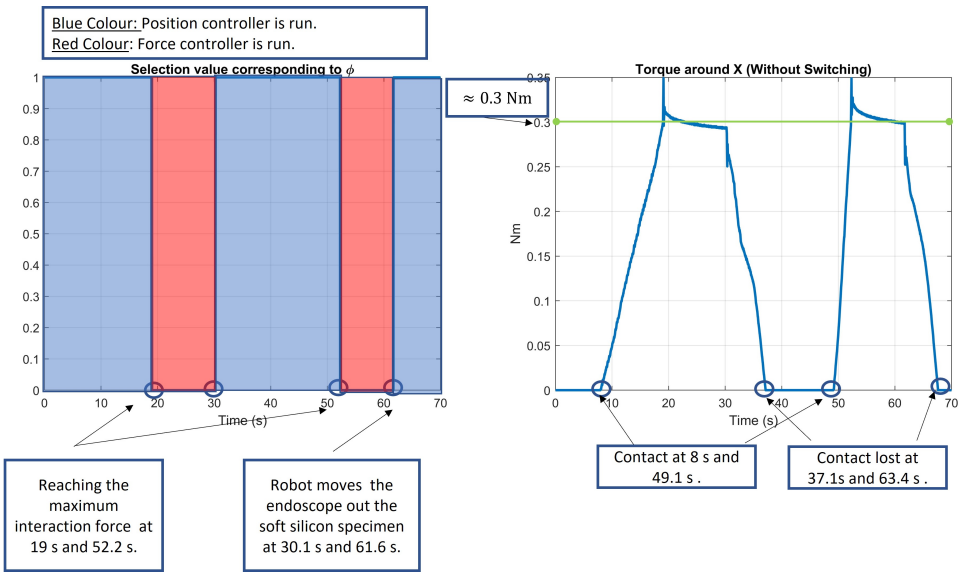

Figure 6.26. The signal S_p and interaction torques of the first experiment is presented.

In the first experiment, the $\dot{\phi}_c$ is changed when $\dot{\psi}_c$ and $\dot{d}_c$ are kept as 0 $\frac{rad}{s}$ and 0 $\frac{mm}{s}$. The endoscope penetrates soft silicon specimen by implementing the motion control algorithm. The force controller is activated when the maximum interaction torque value is reached. As observed in Fig. 6.26, the force controller is initially run at $19s$ and $52s$ where S is switched from 1 to 0. The controller aims to keep the system at 0.3 Nm; however, the overshoot is observed when the switching occurs. Due to the overshoot, the torque value is reached 0.35 Nm instantaneously, and the torque value settles to its steady-state response. As mentioned previously, the system is type-0; however, the integral term is not used in the controller due to the stability of switched systems. For that reason, a steady-state error is expected, and in the first experiment, the maximum steady-state error is observed as 2% of the desired force value.

In the second experiment, the $\dot{\psi}_c$ is changed when $\dot{\phi}_c$ and $\dot{d}_c$ are kept as 0 $\frac{rad}{s}$ and 0 $\frac{mm}{s}$. The endoscope penetrates the soft silicon specimen by implementing the motion control algorithm. The force controller is activated when the maximum interaction torque value is reached. As observed in Fig. 6.27, the force controller is initially run at $14.5s$ and $53.5s$ where S is switched from 1 to 0. The controller aims to keep the system at 0.3 Nm; however, the overshoot is not observed in this experiment while the endoscope is inserted into the soft silicon specimen at approximately the same speed as in the first experiment.

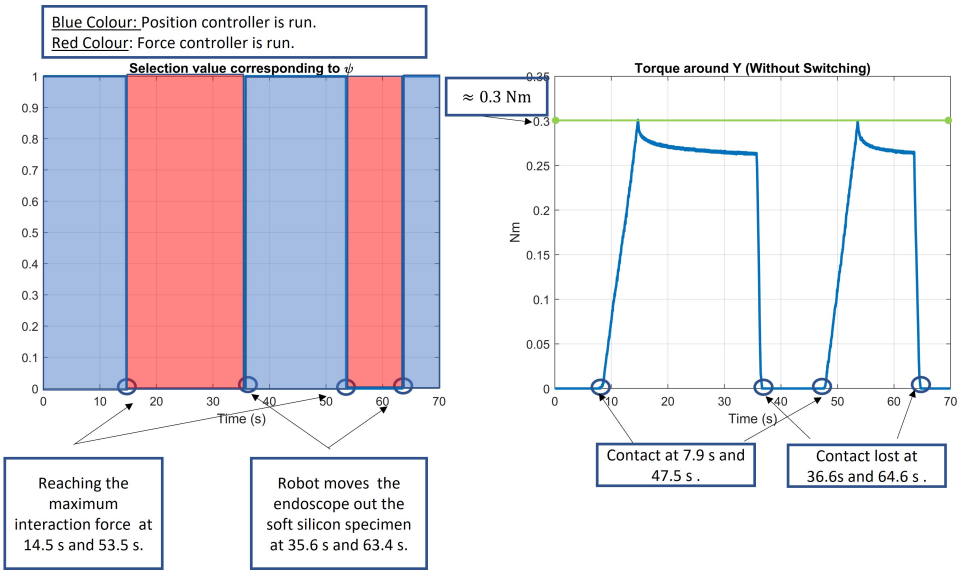

Figure 6.27. The signal S_p and interaction torques of the second experiment is presented.

The maximum steady-state error is observed as 12% of the desired force value.

6.4. Experiments for Interacting with the Medical Tool and Soft Tissue

In this surgical scenario, the surgeon commands the teleoperated co-worker robot without physical interaction. For instance, in the surgery for the pituitary tumors, NeuRoboScope inserts into the surgical workspace through the nasal cavity for monitoring the tumor on the pituitary gland; in addition, the surgeon uses a rigid medical tool for operating in the surgical workspace. Therefore, the NeuRoboScope shares the workspace with the soft tissues of the nasal concha and the rigid medical tool held by the surgeon, as represented in Fig. 6.28.

In this scenario, the endoscope does not interact with the soft tissue and the medical device at the same time, as observed in Fig. 6.29 where there is no interaction between the robot and its environment when the endoscope is located between locations B and D. The locations of the soft tissue and the medical device are known for this scenario; however, their locations have to be estimated by using the sensor's data when the environment's locations are unknown. The endoscope initially interacts with the soft tissue at location B and the medical tools held by the surgeon at location D. It is assumed that the surgeon sends the speed commands shown in Fig. 6.30 to NeuRoboScope. The

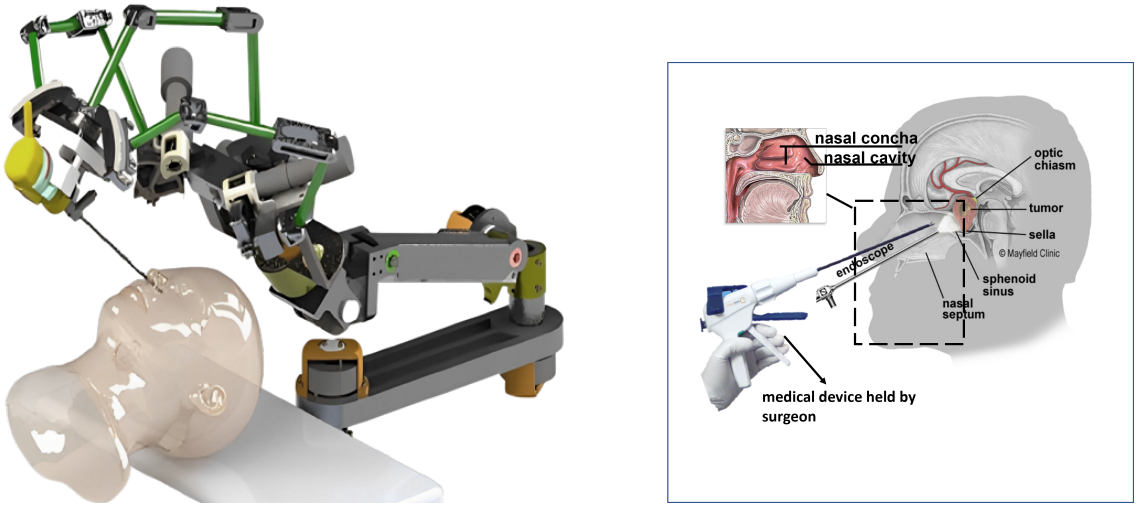

(a) NeuRoboScope during the operation

(b) Endoscope and its environment

Figure 6.28. The surgical robotic operation for removing tumor on the pituitary gland by using the NeuRoboScope

desired endoscope's position and interaction torque profile corresponding the surgeon's speed command are shown in Fig. 6.31 and 6.32, respectively. The NeuRoboScope moves the endoscope through the soft tissues and interacts with them at t_2, and the maximum interaction torque value is obtained when the maximum speed command is given at t_3. When the surgeon's speed command gets $0\ \frac{rad}{s}$, the interaction between the endoscope and the soft tissues is lost at t_4. There is no interaction between t_4 and t_6. When the robot moves the endoscope to location D, the interaction between the endoscope and the medical tool held by the surgeon occurs at t_6. The maximum interaction torque value is obtained when the maximum speed command is given at t_7. The interaction between the endoscope and the soft tissues is lost at t_8 when the surgeon's speed command gets $0\ \frac{rad}{s}$.

According to the interaction torque profile corresponding to the surgeon's speed command trajectory, the interaction behavior in Fig. 6.11 is desired for both environments with different dynamics, such as soft (soft tissues) and stiff (the medical tool held by the surgeon) environments. The designed criterion for the active compliant controller designed in Section 6.3.1 is that surgeon's maximum speed command generates the maximum interaction torque value. Also, the controller is designed in this scenario according to this criterion to provide a safe interaction between the endoscope and both environments.

In this scenario, the impedance (the desired relation between interaction torque and the surgeon's speed command) must be regulated to achieve a safe interaction. Also,

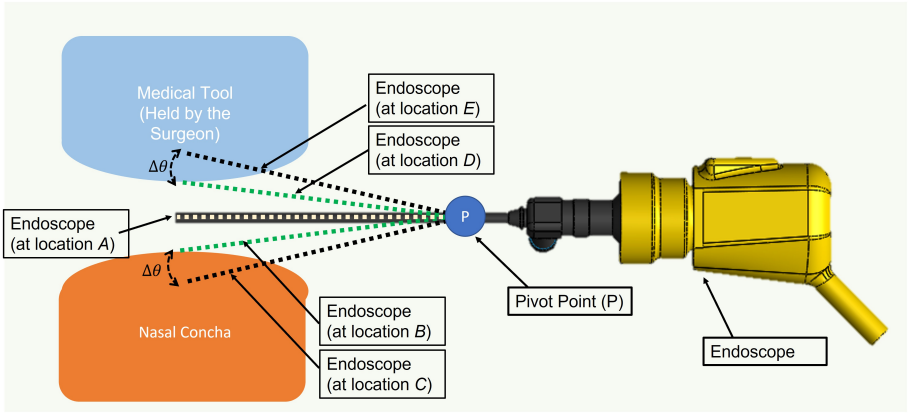

Figure 6.29. The interaction scenario between the endoscope and its environment constituted by the soft tissues of the nasal concha and a medical tool held by surgeon

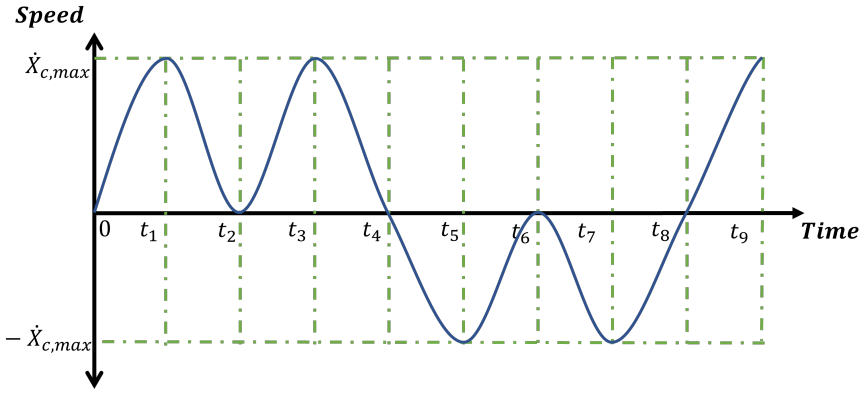

Figure 6.30. The surgeon's arbitrary speed command for the NeuRoboScope

the surgeon's speed command is the input of the system. Therefore, the proper active compliant control algorithm for this scenario is an impedance controller designed according to the desired criterion mentioned above to obtain safe interaction between the endoscope and its environments. Due to the environments having different dynamics, the controller parameters must be switched according to the environment to reach the desired behavior.

The design criteria of the controller is presented as follows.

✓ Stability: The pole location of each system and stability of the switched systems are checked.

✓ Robustness: The controller gains are designed to minimize the sensitivity function.

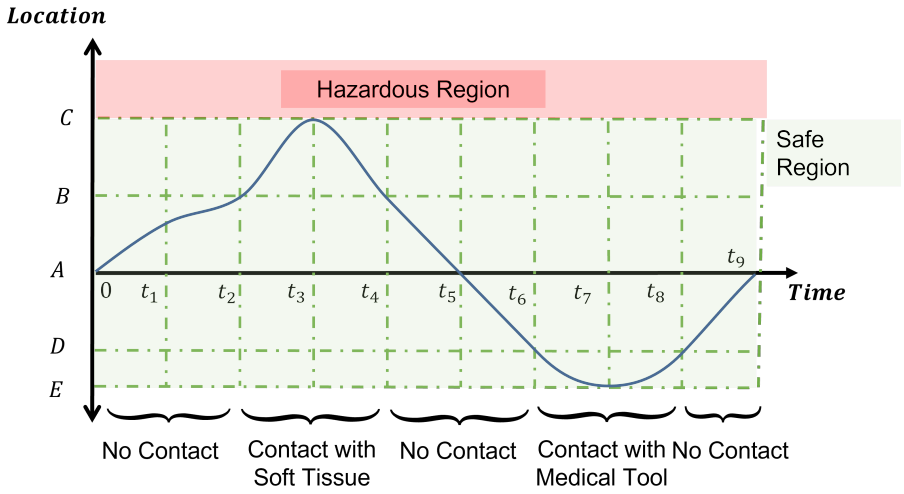

Figure 6.31. The changes in the endoscope's location according to the given surgeon's speed command when an active compliant controller is implemented in the NeuRoboScope

6.4.1. Impedance Controller Design

In Section 6.1, the soft and stiff silicon specimens are modeled as the elastic model, and the parameters are measured as $747.14\ \frac{N}{m}$ and $1070.5\ \frac{N}{m}$ for soft and stiff silicon specimens, respectively. The distance between the contact point and the F/T sensor is measured as ≈ 240 mm. Therefore, the $k_{soft} = 747.1461\ \frac{N}{m}\frac{0.24m}{\frac{rad}{0.24m}} \approxeq 43.0356\frac{Nm}{rad}$ as mentioned previously. In addition, the $k_{stiff} = 1070.5\ \frac{N}{m}\frac{0.24m}{\frac{rad}{0.24m}} \approxeq 61.6608\frac{Nm}{rad}$. By applying the same methodology explained in Section 6.3.2 with considering $M_t \neq 0$, the optimum admittance gains are found as $M_t = 0.01$ and $B_t = 2.15$ for soft silicon specimen and $M_t = 0.01$ and $B_t = 2.11$ for stiff silicon specimen. In a similar way mentioned in Section 6.3.2, the stability analysis of the switched systems is done.

With numerical values, $A_1 = \begin{bmatrix} 0 & 1 & 0 & 0 \\ 1618.80 & -56.89 & -1 & 0 \\ 0 & 0 & -211 & 100 \\ 99820.9 & 1752.22 & 0 & 0 \end{bmatrix}$ where $M_t = 0.01$, $B_t = 2.11$, and $k_{stiff} = 61.6608\frac{Nm}{rad}$. and $A_2 = \begin{bmatrix} 0 & 1 & 0 & 0 \\ 1618.80 & -56.89 & -1 & 0 \\ 0 & 0 & -410 & 100 \\ 79666.19 & 1222.89 & 0 & 0 \end{bmatrix}$

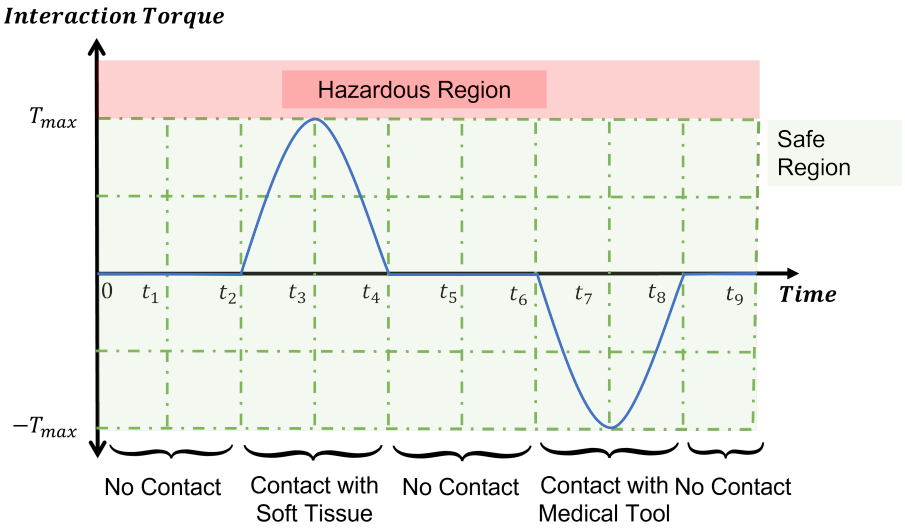

Figure 6.32. The interaction torque between the endoscope and the soft tissues according to the given surgeon's speed command when an active compliant controller is implemented in the NeuRoboScope

where $M_t = 0.01$, $B_t = 2.15$, and $k_{soft} = 43.0356\frac{Nm}{rad}$. B_1. A_1 and A_2 are $Hurwitz$ matrices. Therefore, the common Lyapunov function is searched as explained in Section 5.1.1.1. As a result, the system is stable under arbitrary switching in the sense of Lyapunov.

6.4.2. Experimental Study

In all experiments, the initial position of the NeuRoboScope is chosen as $\phi \approxeq 0°$, $\psi \approxeq 0°$, and $d \approxeq 150\ mm$ where surgery is performed in the real surgical scenario.

In the first experiment, the $\dot{\phi}_c$ is changed when $\dot{\psi}_c$ and $\dot{d}_c$ are kept as $0\ \frac{rad}{s}$ and $0\ \frac{mm}{s}$ As observed in Fig. 6.33, the NeuRoboScope does not interact with the soft or stiff silicon specimen at the initial of the experiments. The endoscope initially penetrates the soft silicon specimen at $2\ s$ and moves out at $18\ s$. During the endoscope moving inside the soft specimen, the RMSE between desired impedance and measured impedance is calculated as $0.12335\ \frac{Nms}{rad}$ where the desired impedance is $2.1486\frac{Nms}{rad}$. At $20.9\ s$, the endoscope penetrates a stiff specimen, and the control parameters are switched. During the endoscope moving inside the stiff specimen, the RMSE between desired impedance and measured impedance is calculated as $0.4621\ \frac{Nms}{rad}$ where the desired impedance is $2.1486\frac{Nms}{rad}$.

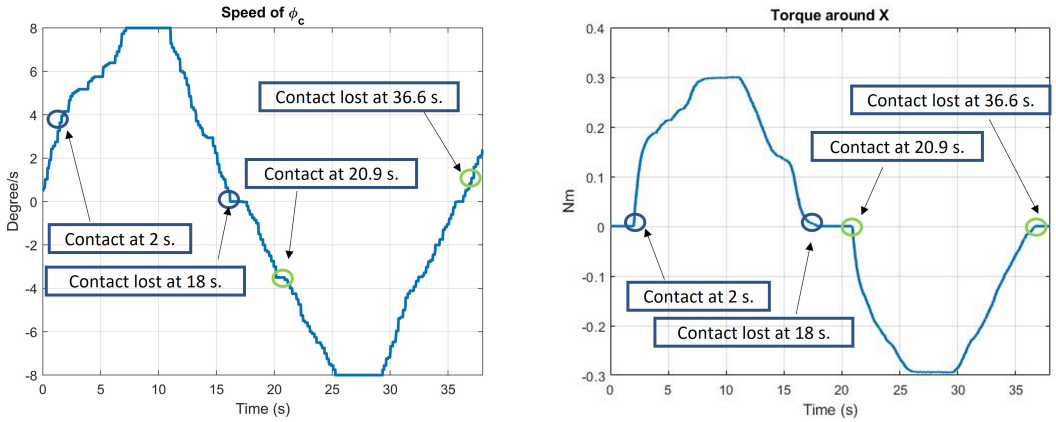

Figure 6.33. The command speed of ϕ and the interaction torque when the NeuRoboScope interacts with the soft and stiff silicon specimens

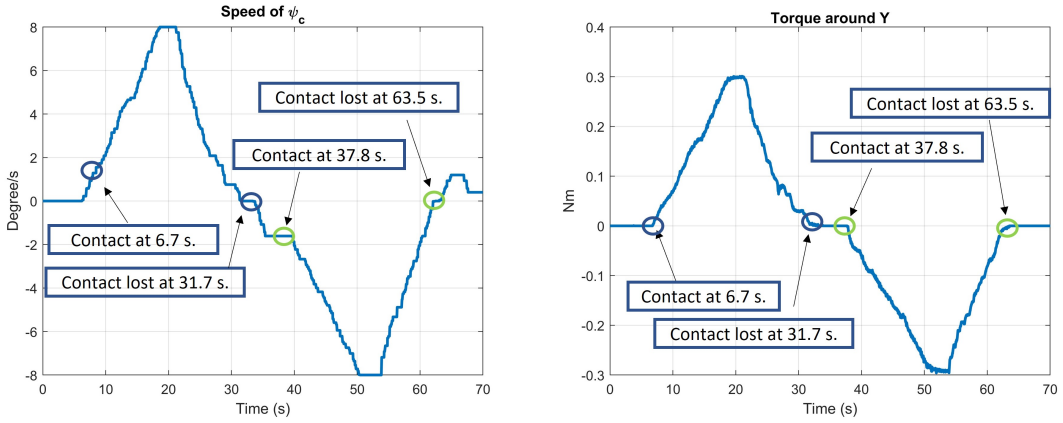

Figure 6.34. The command speed of ϕ and the interaction torque when the NeuRoboScope interacts with the soft and stiff silicon specimens

In the second experiment, the $\dot{\psi}_c$ is changed when $\dot{\phi}_c$ and $\dot{d}_c$ are kept as $0\ \frac{rad}{s}$ and $0\ \frac{mm}{s}$ As observed in Fig. 6.34, the NeuRoboScope does not interact with the soft or stiff silicon specimen at the initial of the experiments. The endoscope initially penetrates the soft silicon specimen. at $6.7\ s$ and moves out at $31.7\ s$. During the endoscope moving inside the soft specimen, the RMSE between desired impedance and measured impedance is calculated as $0.5333\ \frac{Nms}{rad}$ where the desired impedance is $2.1486\frac{Nms}{rad}$. At $37.8\ s$, the endoscope penetrates the stiff specimen, and the control parameters are switched. During the endoscope moving inside the stiff specimen, the RMSE between desired impedance and measured impedance is calculated as $0.17\ \frac{Nms}{rad}$ where the desired impedance is $2.1486\frac{Nms}{rad}$.

CHAPTER 7

DESIGN AND EXPERIMENTAL VERIFICATION OF THE ACTIVE COMPLIANT CONTROLLER FOR "HANDS-ON" CONTROLLED MODE

In this scenario, the surgeon physically interacts with the co-worker robot. The surgeon holds the robot and moves it, as shown in Fig. 1.1a. The NeuRoboScope has a non-backdrivable actuation system; therefore, an admittance controller is designed and implemented to NeuRoboScope for making the robot backdrivable, and the results are obtained experimentally.

7.1. Experimental Setup for Testing Active Compliant Controller in "Hands-on" Controlled Mode

The experimental setup is explained in Section 6.2, where an actuator with a handle is added for driving the endoscope, as shown below.

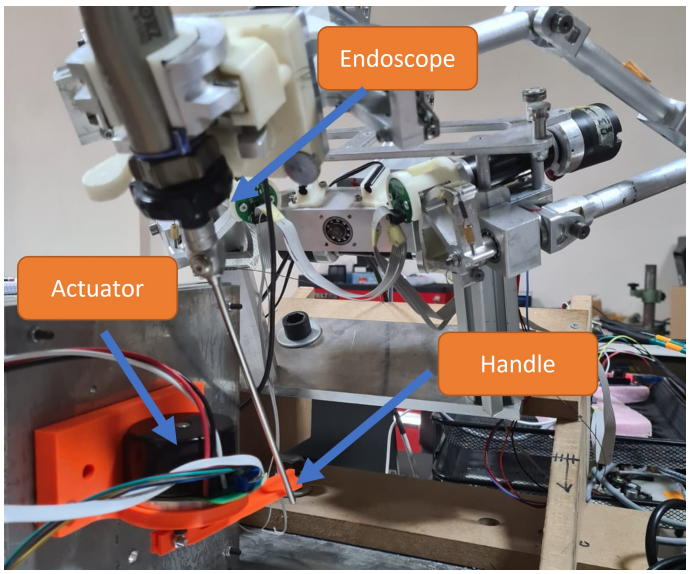

Figure 7.1. The experimental setup for experimental studies of the admittance controller

In this new setup, an EC motor (EC 60 flat Ø60 mm, brushless, 100 Watt) with

a handle is used for interacting with the endoscope. The ESCON 50/5 Servocontroller drives the actuation system, and the operation mode is chosen as an open-loop speed controller. The input of the actuation system is kept constant, and the system is enabled/disabled by using the STM32 Discovery board.

7.2. Experiments for Surgeon Interaction Using Admittance Controller

In previous scenarios, the surgeon remotely commands the teleoperated co-worker robot; however, in this scenario, the surgeon moves the endoscope through physical interaction. It is known from the previous chapters that the NeuRoboScope has non-backdrivable actuation systems; therefore, the interaction forces applied by the surgeon cannot move the robot. The admittance controller is designed to make the system backdrivable where the input and output of the system are interaction torque values and the motion, respectively. As shown in Fig. 7.2, the surgeon applies interaction torques T_x and T_y to move the robot around $\vec{x}_2$ and $\vec{y}_2$ defined in Fig. 3.5. The applied torques by the surgeon are converted to θ_x and θ_y to move the robot by proper admittance controller's parameters M_t and B_t. This study investigates the effect of these parameters on performance in terms of agility and human-effort.

The design criteria of the controller is presented as follows.

- ✓ Stability: The pole location of the system are checked.
- ✓ Robustness: The controller gains are designed to minimize the sensitivity function.
- ✓ Agility: In this study, the average speed of the robot during operation is used as an agility metric.
- ✓ Human - Effort: In this study, an actuator with handle imitates the surgeon's hand motion, the applied total force will be evaluated as human-effort.

7.2.1. Admittance Controller Design

Fig. 7.3 presents the block diagram of the admittance control scheme. As mentioned previously, the $\hat{T}_{ext}$ is neglected due to the high reduction of the actuation system

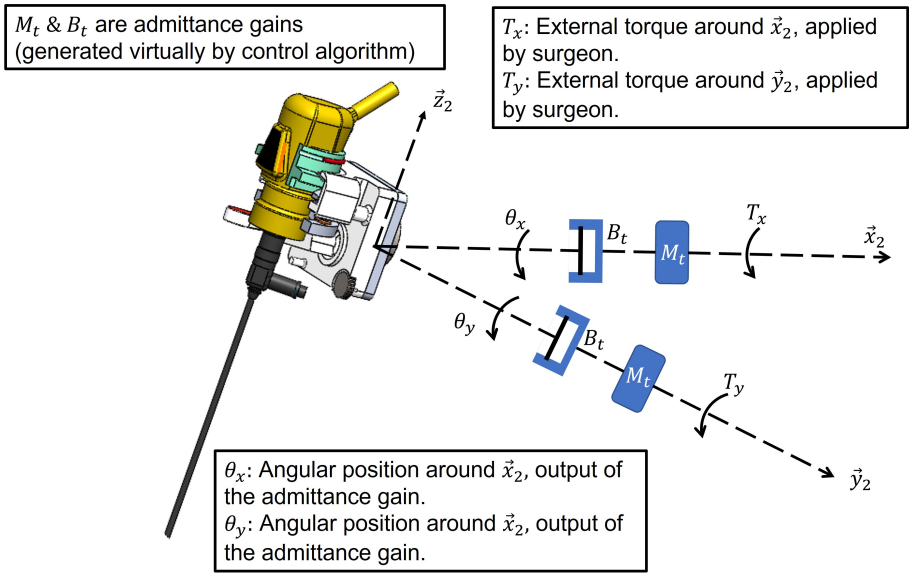

Figure 7.2. The virtual mass M_t and damper B_t system is represented where the input of system is the external torques applied by the surgeon and the output is angular position.

and running the control algorithm at high frequency. Therefore, the block diagram is modified as in Fig. 7.4, where the admittance gain is designed as shown in Eq. 7.1.

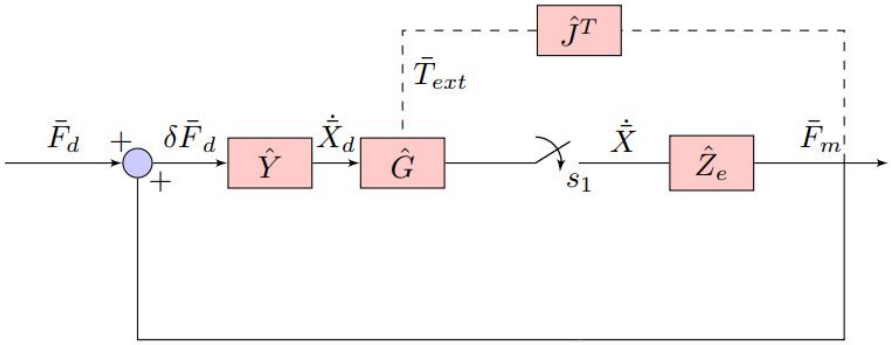

Figure 7.3. Admittance controller scheme in task space

$$Y(s) = \frac{s}{M_t s^2 + B_t s} \tag{7.1}$$

For this case, $\bar{F}_d$ is chosen as $\bar{0}$, and the admittance gain parameters are chosen as shown in Table 7.1 for evaluating the M_t and B_t's effect on agility and human-effort.

It is known that the admittance controller is a robust compliant controller. When there is no collision or contact (Switch s_1 is opened in Fig. 7.4), $F_m = 0$ therefore,

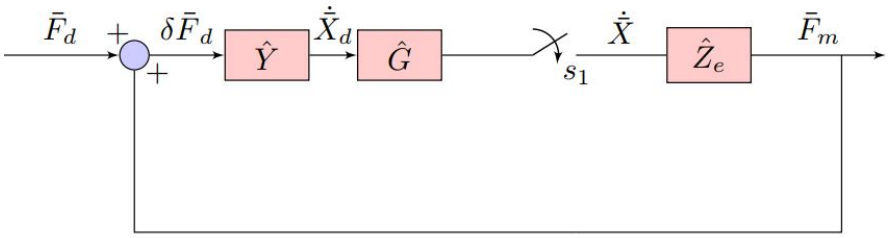

Figure 7.4. The modified admittance controller scheme

Table 7.1. The designed parameters M_t and B_t of the admittance gain for each experiment

	1^{st} Exp.	2^{nd} Exp	3^{rd} Exp.	4^{th} Exp.	5^{th} Exp.	6^{th} Exp.
M_t (kgm^2)	1	2	3	1	2	3
B_t $(\frac{kgm^2}{s})$	4	4	4	8	8	8

$\dot{X} = 0$. When there is collision or contact (Switch s_1 is closed.), $F_m \neq 0$ therefore, $\dot{X} \neq 0$. However, there is no discontinuity. Due to that, the system's poles are searched for stability where switch s_1 is closed, and the stability is guaranteed for each admittance parameter.

7.2.2. Experimental Study

In this scenario, the surgeon holds and moves the NeuRoboScope, which has a non-backdrivable system. Therefore, an admittance controller is implemented in NeuRoboScope to make the system backdrivable. The admittance parameters have a significant role in the human-effort and agility. For evaluating these performance metrics, the experiments are done where an experimental setup is prepared to imitate the surgeon's hand, as explained in Section 7.1. This setup interacts with an endoscope, and the robot moves the endoscope according to the applied torque and admittance parameters. In experiments, the admittance parameters are changed for each experiment as shown in Table 7.1, and the performances are compared.

In all experiments, the initial position of the NeuRoboScope is chosen as $\phi \approxeq 0°$, $\psi \approxeq 0°$, and $d \approxeq 150\ mm$ where surgery is performed in an actual surgical scenario. The applied torque to the endoscope changes the angle ϕ and ψ. However, the analyses

are done for ϕ because there is a slight variation around the ψ due to the location of the experimental setup. Moreover, the analyzes for the ϕ are found to be sufficient to evaluate the admittance parameters. In experiments, the average of $\dot{\phi}$ is used as an agility metric while the ϕ reaches from 0° to -15°, and the total applied torque value is used for evaluating the human effort.

In experiments 1 to 3, the B_t term is kept as $4\ \frac{kgm^2}{s}$ where the M_t is chosen as $1\ kgm^2$ for experiment 1, $2\ kgm^2$ for experiment 2, and $3\ kgm^2$ for experiment 3. When M_t term is increased 1 to $2\ kgm^2$, the average of $\dot{\phi}$ is decreased as 6% however, applied total torque is increased 4% for changing the ϕ from 0° to -15°. When M_t term is increased 2 to $3\ kgm^2$, the average of $\dot{\phi}$ is decreased as 5% however, applied total torque is increased 7% for changing the ϕ from 0° to -15°.

In experiments 4 to 6, the B_t term is kept as $8\ \frac{kgm^2}{s}$ where the M_t is chosen as $1\ kgm^2$ for experiment 4, $2\ kgm^2$ for experiment 5, and $3\ kgm^2$ for experiment 6. When M_t term is increased 1 to $2\ kgm^2$, the average of $\dot{\phi}$ is decreased as 2% however, applied total torque is increased 1% for changing the ϕ from 0° to -15°. When M_t term is increased 2 to $3\ kgm^2$, the average of $\dot{\phi}$ is decreased as 2% however, applied total torque is approximately the same for changing the ϕ from 0° to -15°.

When experiment 1 is compared with experiment 4 where B_t is increased $4\ \frac{kgm^2}{s}$ to $8\ \frac{kgm^2}{s}$ while M_t is $1\ kgm^2$, the average of $\dot{\phi}$ is decreased as 35% however, applied total torque is increased 97% for changing the ϕ from 0° to -15°. When experiment 2 is compared with experiment 5 where B_t is increased $4\ \frac{kgm^2}{s}$ to $8\ \frac{kgm^2}{s}$ while M_t is $2\ kgm^2$, the average of $\dot{\phi}$ is decreased as 33% however, applied total torque is increased 92% for changing the ϕ from 0° to -15°. When experiment 3 is compared with experiment 6 where B_t is increased $4\ \frac{kgm^2}{s}$ to $8\ \frac{kgm^2}{s}$ while M_t is $3\ kgm^2$, the average of $\dot{\phi}$ is decreased as 30% however, applied total torque is increased 79% for changing the ϕ from 0° to -15°.

As observed in experiments 1 to 3, the increasing M_t parameter decreases the agility and increases the human-effort. This inference is not made explicitly in experiments 4 to 6 because the effect of B_t(= $8\ \frac{kgm^2}{s}$) has a dominant effect on agility and human-effort. Due to that, the effect of changing in M_t is not observed explicitly. This situation is also observed when the experiments have the same M_t but different B_t values. According to the results, decreasing the value of M_t and B_t increases agility and it decreases the human-effort.

CHAPTER 8

CONCLUSIONS

The use of co-worker robots in surgical fields has provided many advantages as mentioned previously which are categorized as teleoperated and "hands-on" controlled robots. Teleoperated robots are controlled by a surgeon without physical interaction and they share the workspace with the tissues and medical tools. Surgeons move the "hands-on" controlled robots by applying physical interaction in free space. These robots can exert excessive forces to harm their environment or themselves. Active or passive compliant controllers were proposed in the literature to provide a safe or desired interaction. These controllers are designed to solve the issues for different applications. The controllers were reviewed in Chapter 2 to understand the purposes of using the controllers. This dissertation focused on active compliant control algorithms such as implicit impedance control, explicit impedance control, admittance control, hybrid position/force control, and parallel position/force control algorithms. Implicit controller (absence of F/T sensor in the control loop) can be applied to the only non-backdrivable system; however, explicit controller (presence of F/T sensor in the control loop) is proper for both backdrivable and non-backdrivable systems. Moreover, impedance and admittance controllers regulate the dynamics between motion and force to reach desired interaction. In the impedance controller, the motion is the system's input, while the system's output is force. In contrast, admittance control gets force value as input and motion as output. A hybrid position/-force controller and parallel position/force controller aim to follow the given motion and force trajectories simultaneously. These controllers are suitable for a system having more than one degree of freedom. They make the robots behave stiffer in the desired directions by applying position control while they behave in compliance in other directions. The parallel position/force controller is robust to uncertainties; in contrast, the hybrid position/force controller is sensitive to uncertainties in the system model. However, stability problems are observed when the parallel position/force controller is implemented in the NeuRoboScope. Due to that, this controller was not used in this dissertation.

The algorithms studied in the dissertation were implemented in the novel surgical co-worker NeuRoboScope. This robot aims to solve the issues encountered during endoscopic pituitary glands surgery, such as communication problems and physical fatigue. The NeuRoboScope has two parts which are active and passive. The passive one is used

for positioning the active part's base. The active part controls the endoscope according to commands. NeuRoboScope is a parallel manipulator with an RCM mechanism, and the actuation system of the NeuRoboScope is non-backdrivable. For that reason, explicit controllers are suitable for these systems.

Explicit active compliant controller in Fig. 2.5 generally requires a motion control algorithm as a low-level controller, and this controller must be run at high frequencies. For a precise position controller, the computed torque control algorithm was designed as a motion control algorithm, and this algorithm requires the full dynamics of the NeuRoboScope. To run the algorithm at high frequencies, a simplified dynamic model with a new correction coefficient is proposed in this dissertation. In Chapter 3, the dynamics of the NeuRoboScope was calculated by using the recursive Newton-Euler algorithm, and the terms related to acceleration, velocity, and gravitational acceleration were investigated, and it was observed that the velocity, acceleration, gravity related terms have 11.5%, 13% and 75.5% effect on the total torques, respectively. In addition, the mobile platform has a higher effect on the dynamics of the NeuRoboScope when compared to the robot's links, as observed in Table 3.1. By using this information, assumptions are made to simplify the system's dynamics, such as assuming that the links and joints of the robot as rigid, neglecting frictions, masses except for the mobile platform, the moment of inertia values except for the mobile platform & an actuator connected to the middle leg, and the Coriolis and centripetal terms. When the simplified model is compared with the actual model, it is inferred that the derived model is not substituted for the accurate dynamics model. To deal with this, a correction coefficient method is proposed by calculating the torque values of the model. Also, the correction coefficients for the orientation of the active part's base is obtained as shown in Fig. 3.12. The result shows that the simplified dynamic model with correction coefficient can be used rather than deriving the full dynamic model in surgical robotic applications. ARM Cortex M4 is capable of running the computed torque method with a proposed simplified dynamic model at $\approx 700\ Hz$.

The motion controller was run at $500\ Hz$ in an experimental study in Chapter 4, where the computed torque method and independent joint controller were implemented in the NeuRoboScope, and the results are discussed. Before designing the controller, the dynamics of the actuation system were derived; therefore, the mechanical time constant is calculated to use in the design of the controller. Three experiments were done for each motion controller, and the RMSE in degree was obtained as Table 4.2 to 4.4 for computed torque method with simplified dynamics model and Table 4.5 to 4.7 for an independent joint method where simplified gravity matrix is added as a feedforward term. The results

show that both controllers have adequate performance for the NeuRoboScope. Moreover, the independent joint controller performs better than the computed torque method. The reason is that the simplified inertia matrix cannot mimic the real inertia matrix of the system. To solve this, the correction coefficient can be calculated by the inertia matrix and gravity matrix separately.

The design criteria of the proper active compliant control algorithms are explained in Chapter 5. The safety criteria, stability and robustness, and performance criteria, agility for both types of surgical co-worker robots, and human effort for only "hands-on" controlled surgical robots are discussed.

In Chapter 6, the design and implementation of the proper active compliant control algorithms were explained according to interaction scenarios of the teleoperated surgical robots. The safe interaction between teleoperated robot and the soft tissue on the nasal concha is desired in the first interaction scenario. Because of the difficulty of accessing the actual patient's tissue, a soft silicon specimen is used to imitate the soft tissue. The system's input is velocity, and there is no requirement to follow the predetermined force or position trajectory. Therefore, the impedance controller is a proper active compliant control for this scenario. From preliminary studies in Chapter 2, the desired impedance value is calculated as $2.1486\ \frac{Nms}{rad}$. The impedance controller aims to make the NeuRoboScope display the desired impedance. Therefore, the error between the impedance displayed by the NeuRoboScope and the desired impedance is designed as a cost function. By concerning the robustness and stability, the optimum impedance gains M_t and B_t are calculated as 0 and 2.15, respectively. Experimental results show that the safe interaction between the endoscope attached to the NeuRoboScope's end-effector and the soft silicon specimen is provided by implementing the impedance controller.

Another impedance controller is designed and implemented for the same interaction scenario to improve agility and provide safety. This controller behaves as same as the former controller when the robot moves the endoscope into the soft silicon specimen. However, the controller aims to switch the system's impedance to half of the desired impedance ($= 1.0743\frac{Nms}{rad}$) to improve the agility when the endoscope is moved out of the soft silicon specimen. By concerning the robustness and switching stability, the optimum impedance gains M_t, and B_t are calculated as 0.01 and 2.15 where the desired impedance is $2.1486\ \frac{Nms}{rad}$ also the optimum impedance gains M_t and B_t are calculated as 0.01 and 1.04 where the desired impedance is $1.074\ \frac{Nms}{rad}$, respectively. Experimental results show that the safe interaction between the robot and the soft silicon specimen is provided; in addition, the execution time of moving the endoscope out of the soft silicon specimen is

improved as $\approx 20\%$.

To provide a safe interaction in the first interaction scenario, a hybrid position/-force controller is designed to prevent exceeding the interaction torque threshold when the tip of the teleoperated robot penetrates the tissue rather than following the desired impedance. In this controller, the position controller is applied until the interaction torque value reaches the maximum interaction torque $0.3\ Nm$. The force controller is applied when reaching the maximum interaction torque to prevent exceeding maximum interaction torque. By changing the selection matrix $\hat{S}$, the switching between force and position controllers is provided. Concerning switching stability, the P controller is designed rather than the PI controller. For that reason, the steady-state error is observed in experiments. The maximum steady-state error is observed as 2% of the desired torque value around the x-direction while the maximum steady-state error is observed as 12% of the desired torque value around the y-direction

In the second interaction scenario for the teleoperated surgical robots, the safe interaction between teleoperated robot and its environment constituted of soft and silicon specimens is desired. The stiff silicon specimen imitates a medical tool held by the surgeon. In this scenario, the robot cannot interact with both soft and stiff tissues at the same time. The system's input is velocity, and there is no requirement to follow the predetermined force or position trajectory. Therefore, the impedance controller is a proper active compliant control for this scenario. The desired impedance value is calculated as 2.1486 $\frac{Nms}{rad}$ for both soft and stiff silicon specimens. The desired impedance controller aims to make the NeuRoboScope display the desired impedance. Therefore, the error between the impedance displayed by the NeuRoboScope and the desired impedance is designed as a cost function. By concerning the robustness and switching stability, the optimum impedance gains M_t and B_t are calculated as 0.01 and 2.15 for soft silicon specimen and 0.01 and 2.11 for stiff silicon specimen, respectively. Experimental results show that the safe interaction between the endoscope attached to the NeuRoboScope's end-effector and its environments is provided by implementing the impedance controller.

In Chapter 7, the safe interaction between a 'hands-on' controlled robot and the surgeon is desired. The system's input is torque, and there is no requirement to follow the predetermined force or position trajectory. The admittance controller is selected as a proper active compliant control for this scenario. Admittance controller gains are chosen by considering the stability, as shown in Table 7.1. The results show that decreasing the value of M_t and B_t increases agility and decreases the human effort.

In this dissertation, the active compliant control algorithms are designed consid-

ering performance and safety criteria for the interaction scenarios that the surgical co-worker robots encounter during the surgery. For achieving safe interaction between the robot and its environment having different dynamics, such as soft tissue and medical tool, a switching methodology for the active compliant controllers are presented. In the future work of this dissertation, the controller with switching methodology will be evaluated for different interaction scenarios where the environment consists of soft tissues, bones, medical tools, and surgeons. Also, the robot will physically interact with them at the same time, which is not included in this dissertation. Moreover, the transparency criterion for feeling the environment by the surgeon and the accuracy criterion for improving precision will be considered in the admittance controller design for the "hands-on" controlled surgical co-worker robots.

REFERENCES

Albakri, A. (2015). *Haptic Teleoperation for Robotic-Assisted Surgery*. Ph. D. thesis, Université Montpellier, Montpellier, France.

Aldanmaz, A. B., O. Ayit, G. Kiper, and M. s. C. Dede (2023). Gravity compensation of a 2r1t mechanism with remote center of motion for minimally invasive transnasal surgery applications. *Robotica 41*(3), 807–820.

An, C. and J. Hollerbach (1987). Kinematic stability issues in force control of manipulators. In *Proceedings. 1987 IEEE International Conference on Robotics and Automation*, Volume 4, pp. 897–903. IEEE.

Arnold, J. and H. Lee (2021). Variable impedance control for phri: Impact on stability, agility, and human effort in controlling a wearable ankle robot. *IEEE Robotics and Automation Letters 6*(2), 2429–2436.

Attanasio, A., B. Scaglioni, E. De Momi, P. Fiorini, and P. Valdastri (2021). Autonomy in surgical robotics. *Annual Review of Control, Robotics, and Autonomous Systems 4*(1), 651–679.

Baumgart, F. (2000). Stiffness-an unknown world of mechanical science? *Injury-International Journal for the Care of the Injured 31*(2), 14–23.

Beasley, R. A. (2012). Medical robots: Current systems and research directions. *Journal of Robotics 2012*, 1–14.

Bicchi, A. and G. Tonietti (2004). Fast and" soft-arm" tactics [robot arm design]. *IEEE Robotics & Automation Magazine 11*(2), 22–33.

Bitz, T., F. Zahedi, and H. Lee (2020). Variable damping control of a robotic arm to improve trade-off between agility and stability and reduce user effort. In *2020 IEEE International Conference on Robotics and Automation (ICRA)*, pp. 11259–11265.

Blaya, J. A. and H. Herr (2004). Adaptive control of a variable-impedance ankle-foot orthosis to assist drop-foot gait. *IEEE Transactions on neural systems and rehabilitation engineering 12*(1), 24–31.

Borutzky, W. (2009). *Bond graph methodology: development and analysis of multidisciplinary dynamic system models*. Springer Science & Business Media.

Braun;, J. (2012). *Maxon Formulae Handbook*. Maxon Academy.

Broeders, I. and J. Ruurda (2001). Robotics revolutionizing surgery: the intuitive surgical "da vinci" system. *Industrial Robot 28*(5), 387–392.

Burchett, B. T. (2005). Parametric time domain system identification of a mass-spring-

damper system. In *Proc. Amer. Soc. Eng. Edu. Annu. Conf. Expo.*, pp. 12–15.

Calanca, A. (2014). *Compliant Control of Elastic Actuators for Human Robot Interaction*. Ph. D. thesis, University of Verona, Verona, Italy.

Chiaverini, S. and L. Sciavicco (1988). Force/position control of manipulators in task space with dominance in force. *IFAC Proceedings Volumes 21*(16), 137 – 143. 2nd IFAC Symposium on Robot Control 1988 (SYROCO '88), Karlsruhe, FRG, 5-7 October.

Ciblak, N. and H. Lipkin (1999). Synthesis of cartesian stiffness for robotic applications. In *Proceedings 1999 IEEE International Conference on Robotics and Automation (Cat. No. 99CH36288C)*, Volume 3, pp. 2147–2152. IEEE.

Dede, M. İ. C., G. Kiper, T. Ayav, B. Özdemirel, E. Tatlıcıoğlu, S. Hanalioglu, İ. Işıkay, and M. Berker (2021). Human–robot interfaces of the neuroboscope: A minimally invasive endoscopic pituitary tumor surgery robotic assistance system. *Journal of Medical Devices 15*(1).

Drouet, P., S. Dubowsky, and C. Mavroidis (1998). Compensation of geometric and elastic deflection errors in large manipulators based on experimental measurements: Application to a high accuracy medical manipulator. In *Advances in Robot Kinematics: Analysis and Control*, pp. 513–522. Springer.

Fagogenis, G., M. Mencattelli, Z. Machaidze, B. Rosa, K. Price, F. Wu, V. Weixler, M. Saeed, J. E. Mayer, and P. E. Dupont (2019). Autonomous robotic intracardiac catheter navigation using haptic vision. *Science robotics 4*(29), eaaw1977.

Firestone, F. A. (1933). A new analogy between mechanical and electrical systems. *The Journal of the Acoustical Society of America 4*(3), 249–267.

Fisher, W. D. and M. S. Mujtaba (1992). Hybrid position/force control: A correct formulation. *The International Journal of Robotics Research 11*(4), 299–311.

Freund, H.-J. (1986). Time control of hand movements. In H.-J. Freund, U. Büttner, B. Cohen, and J. Noth (Eds.), *The Oculomotor and Skeletalmotor Systems: Differences and Similarities*, Volume 64 of *Progress in Brain Research*, pp. 287–294. Elsevier.

Fujimoto, Y., T. Kominami, and H. Hamada (2009). Development and analysis of a high thrust force direct-drive linear actuator. *IEEE Transactions on Industrial Electronics 56*(5), 1383–1392.

Goldfield, E. C., Y.-L. Park, B.-R. Chen, W.-H. Hsu, D. Young, M. Wehner, D. G. Kelty-Stephen, L. Stirling, M. Weinberg, D. Newman, et al. (2012). Bio-inspired design of soft robotic assistive devices: The interface of physics, biology, and behavior. *Ecological Psychology 24*(4), 300–327.

Gomes, P. (2011). Surgical robotics: Reviewing the past, analysing the present, imag-

ining the future. *Robotics and Computer-Integrated Manufacturing 27*(2), 261–266. Translational Research – Where Engineering Meets Medicine.

Goodrich, M. and D. Olsen (2003). Seven principles of efficient human robot interaction. In *SMC'03 Conference Proceedings. 2003 IEEE International Conference on Systems, Man and Cybernetics. Conference Theme - System Security and Assurance (Cat. No.03CH37483)*, Volume 4, pp. 3942–3948 vol.4.

Gosrisirikul, C., K. Don Chang, A. A. Raheem, and K. H. Rha (2018). New era of robotic surgical systems. *Asian journal of endoscopic surgery 11*(4), 291–299.

Gullapalli, V., R. A. Grupen, and A. G. Barto (1992). Learning reactive admittance control. In *ICRA*, pp. 1475–1480.

Hanna, G. B. and A. Cuschieri (2008). *Ergonomics of Task Performance in Endoscopic Surgery*, pp. 39–50. Berlin, Heidelberg: Springer Berlin Heidelberg.

Hespanha, J. P. and A. Morse (2002). Switching between stabilizing controllers. *Automatica 38*(11), 1905–1917.

Howard, S., M. Zefran, and V. Kumar (1998). On the 6× 6 cartesian stiffness matrix for three-dimensional motions. *Mechanism and machine theory 33*(4), 389–408.

Howell, L. L. (2013). *Introduction to Compliant Mechanisms*, Chapter 1, pp. 1–13. John Wiley and Sons, Ltd.

Hu, P., F. Wu, J. Peng, P. Liang, and D. Kong (2016). Automatic 3d liver segmentation based on deep learning and globally optimized surface evolution. *Physics in Medicine & Biology 61*(24), 8676.

Ilievski, F., A. D. Mazzeo, R. F. Shepherd, X. Chen, and G. M. Whitesides (2011). Soft robotics for chemists. *Angewandte Chemie International Edition 50*(8), 1890–1895.

Ishida, T. and A. Takanishi (2006). A robot actuator development with high backdrivability. In *2006 IEEE Conference on Robotics, Automation and Mechatronics*, pp. 1–6. IEEE.

Işıtman, O. (2018). *Compliant control of a teleoperated endoscope robot*. Ph. D. thesis, Izmir Institute of Technology, Izmir, Turkey.

Işıtman, O., O. Ayit, and M. İ. C. Dede (2018). The effects of admittance term on backdrivability. In M. I. C. Dede, M. İtik, E.-C. Lovasz, and G. Kiper (Eds.), *Mechanisms, Transmissions and Applications*, Cham, pp. 181–190. Springer International Publishing.

Işıtman, O., O. Ayit, E. Vardarlı, Ş. Hanalioğlu, İ. Işıkay, M. Berker, and M. İ. C. Dede (2019). Viscoelastic modeling of human nasal tissues with a mobile measurement device. In G. Carbone, M. Ceccarelli, and D. Pisla (Eds.), *New Trends in Medical and Service Robotics*, Cham, pp. 216–224. Springer International Publishing.

ISO (2019). Medical electrical equipment — part 2-77: Particular requirements for the basic safety and essential performance of robotically assisted surgical equipment. *Journal of Medical Devices 1*.

Jackson, R. C., R. Yuan, D.-L. Chow, W. S. Newman, and M. C. Çavuşoğlu (2018). Real-time visual tracking of dynamic surgical suture threads. *IEEE Transactions on Automation Science and Engineering 15*(3), 1078–1090.

Jaffray, B. (2005). Minimally invasive surgery. *Archives of Disease in Childhood 90*(5), 537–542.

Jakopec, M., S. Harris, F. Rodriguez y Baena, P. Gomes, and B. Davies (2002). Acrobot: a "hands-on" robot for total knee replacement surgery. In *7th International Workshop on Advanced Motion Control. Proceedings (Cat. No.02TH8623)*, pp. 116–120.

Kanik, M., O. Ayit, M. I. C. Dede, and E. Tatlicioglu (2021). Toward safe and high-performance human–robot collaboration via implementation of redundancy and understanding the effects of admittance term parameters. *Robotica*, 1–16.

Keemink, A. Q., H. van der Kooij, and A. H. Stienen (2018). Admittance control for physical human–robot interaction. *The International Journal of Robotics Research 37*(11), 1421–1444.

Khan, S. G., G. Herrmann, M. Al Grafi, T. Pipe, and C. Melhuish (2014). Compliance control and human–robot interaction: Part 1—survey. *International Journal of Humanoid Robotics 11*(03), 1430001.

Khatib, O. (1987). A unified approach for motion and force control of robot manipulators: The operational space formulation. *IEEE Journal on Robotics and Automation 3*(1), 43–53.

Knott, L. (2013, January). Minimally invasive surgery. [Online; posted 14-January-2013], Reviewed by Jackson C.

Konstantinova, J., A. Jiang, K. Althoefer, P. Dasgupta, and T. Nanayakkara (2014). Implementation of tactile sensing for palpation in robot-assisted minimally invasive surgery: A review. *IEEE Sensors Journal 14*(8), 2490–2501.

Leonard, S., K. L. Wu, Y. Kim, A. Krieger, and P. C. Kim (2014). Smart tissue anastomosis robot (star): A vision-guided robotics system for laparoscopic suturing. *IEEE Transactions on Biomedical Engineering 61*(4), 1305–1317.

Li, X., H. Chen, X. Qi, Q. Dou, C.-W. Fu, and P.-A. Heng (2018). H-denseunet: Hybrid densely connected unet for liver and tumor segmentation from ct volumes. *IEEE Transactions on Medical Imaging 37*(12), 2663–2674.

Liberzon, D. (2003). *Switching in systems and control*, Volume 190. Springer.

Liberzon, D. and R. Tempo (2004). Common lyapunov functions and gradient algorithms.

IEEE Transactions on Automatic Control 49(6), 990–994.

Liu, C., P. Moreira, and P. Poignet (2012). Viscoelastic model based force tracking control for robotic-assisted surgery. In *2012 4th IEEE RAS EMBS International Conference on Biomedical Robotics and Biomechatronics (BioRob)*, pp. 1199–1204.

Maaroof, O. W. N. (2020). *Design of a robot assisted minimally invasive surgical system for pituitary tumor surgery based on safety features*. Ph. D. thesis, Izmir Institute of Technology, Izmir, Turkey.

Majidi, C. (2014). Soft robotics: a perspective—current trends and prospects for the future. *Soft Robotics 1*(1), 5–11.

Mason, M. T. (1981). Compliance and force control for computer controlled manipulators. *IEEE Transactions on Systems, Man, and Cybernetics 11*(6), 418–432.

McKenna, S., H. N. Charif, and T. Frank (2005). Towards video understanding of laparoscopic surgery: Instrument tracking. In *Proc. of Image and Vision Computing, New Zealand*.

Mirtich, B. V. (1996). *Impulse-based dynamic simulation of rigid body systems*. University of California, Berkeley.

Misra, S., K. Ramesh, and A. M. Okamura (2008). Modeling of tool-tissue interactions for computer-based surgical simulation: a literature review. *Presence: Teleoperators and Virtual Environments 17*(5), 463–491.

Moyer, A. E. (1977). Robert hooke's ambiguous presentation of" hooke's law". *Isis 68*(2), 266–275.

Murphy, R. R. and D. Schreckenghost (2013). Survey of metrics for human-robot interaction. In *2013 8th ACM/IEEE International Conference on Human-Robot Interaction (HRI)*, pp. 197–198.

Nageotte, F., P. Zanne, C. Doignon, and M. de Mathelin (2009). Stitching planning in laparoscopic surgery: Towards robot-assisted suturing. *The International Journal of Robotics Research 28*(10), 1303–1321.

Najafi, F. and N. Sepehri (2008). A novel hand-controller for remote ultrasound imaging. *Mechatronics 18*(10), 578–590.

Newman, W. S. (1992, 12). Stability and Performance Limits of Interaction Controllers. *Journal of Dynamic Systems, Measurement, and Control 114*(4), 563–570.

Nichols, K. A. and A. M. Okamura (2013). Autonomous robotic palpation: Machine learning techniques to identify hard inclusions in soft tissues. In *2013 IEEE International Conference on Robotics and Automation*, pp. 4384–4389.

Ogata, K. (2004). *System dynamics*, Volume 4. Prentice Hall Upper Saddle River, NJ.

Olsen, D. R. and M. A. Goodrich (2003). Metrics for evaluating human-robot interactions. In *Proceedings of PERMIS*, Volume 2003, pp. 4.

Osa, T., C. F. Abawi, N. Sugita, H. Chikuda, S. Sugita, H. Ito, T. Moro, Y. Takatori, S. Tanaka, and M. Mitsuishi (2014). Autonomous penetration detection for bone cutting tool using demonstration-based learning. In *2014 IEEE International Conference on Robotics and Automation (ICRA)*, pp. 290–296.

Pandilov, Z. and V. Dukovski (2014). Comparison of the characteristics between serial and parallel robots. *Acta Technica Corvininesis-Bulletin of Engineering 7*(1).

Pappalardo, A., A. Albakri, C. Liu, L. Bascetta, E. D. Momi], and P. Poignet (2016). Hunt–crossley model based force control for minimally invasive robotic surgery. *Biomedical Signal Processing and Control 29*, 31 – 43.

Pashkevich, A., D. Chablat, and P. Wenger (2009). Stiffness analysis of overconstrained parallel manipulators. *Mechanism and Machine Theory 44*(5), 966–982.

Patil, S. and R. Alterovitz (2010). Toward automated tissue retraction in robot-assisted surgery. In *2010 IEEE International Conference on Robotics and Automation*, pp. 2088–2094.

Perret, J. and P. Vercruysse (2014). Advantages of mechanical backdrivability for medical applications of force control. In *Conference on Computer/Robot Assisted Surgery (CRAS)*, pp. 84–86.

Poignet, P. and B. Bayle (2012). *Interaction Modeling and Force Control*, pp. 233–269. Londra, UK: Wiley.

Raibert, M. H. and J. J. Craig (1981). Hybrid Position/Force Control of Manipulators. *Journal of Dynamic Systems, Measurement, and Control 103*(2), 126–133.

Rice, J. J. and J. M. Schimmels (2018). Passive compliance control of redundant serial manipulators. *Journal of Mechanisms and Robotics 10*(4), 044507.

Sabanovic, A. and K. Ohnishi (2011). *Motion Control Systems* (1st ed.). Wiley-IEEE Press.

Saleh, J. A. and F. Karray (2010). Towards generalized performance metrics for human-robot interaction. In *2010 International Conference on Autonomous and Intelligent Systems, AIS 2010*, pp. 1–6.

Salisbury, J. K. (1980). Active stiffness control of a manipulator in cartesian coordinates. In *1980 19th IEEE conference on decision and control including the symposium on adaptive processes*, pp. 95–100. IEEE.

Schiavi, R., A. Bicchi, and F. Flacco (2009). Integration of active and passive compliance control for safe human-robot coexistence. In *2009 IEEE International Conference on Robotics and Automation*, pp. 259–264. IEEE.

Schimmels, J. M. and M. A. Peshkin (1994). Force-assembly with friction. *IEEE Transactions on Robotics and Automation 10*(4), 465–479.

Schoonmaker, R. E. and C. G. Cao (2006). Vibrotactile force feedback system for minimally invasive surgical procedures. In *2006 IEEE International Conference on Systems, Man and Cybernetics*, Volume 3, pp. 2464–2469.

Schumacher, M., J. Wojtusch, P. Beckerle, and O. [von Stryk] (2019). An introductory review of active compliant control. *Robotics and Autonomous Systems 119*, 185 – 200.

Sensinger, J. W. and R. F. Weir (2005). Design and analysis of a non-backdrivable series elastic actuator. In *9th International Conference on Rehabilitation Robotics, 2005. ICORR 2005.*, pp. 390–393. IEEE.

Sherwani, F., M. M. Asad, and B. Ibrahim (2020). Collaborative robots and industrial revolution 4.0 (ir 4.0). In *2020 International Conference on Emerging Trends in Smart Technologies (ICETST)*, pp. 1–5.

Singh, B., N. Sellappan, and P. Kumaradhas (2013). Evolution of industrial robots and their applications. *International Journal of emerging technology and advanced engineering 3*(5), 763–768.

Surdilovic, D. and M. Vukobratovic (2002). *Control of Robotic Systems in Contact Tasks*, pp. 597–648. Florida, USA: CRC Press LLC.

Sutherland, G. R., S. Wolfsberger, S. Lama, and K. Zarei-nia (2013). The evolution of neuroarm. *Neurosurgery 72*(suppl_1), A27–A32.

Taylor, R., P. Jensen, L. Whitcomb, A. Barnes, R. Kumar, D. Stoianovici, P. Gupta, Z. Wang, E. deJuan, and L. Kavoussi (1999). A steady-hand robotic system for microsurgical augmentation. In C. Taylor and A. Colchester (Eds.), *Medical Image Computing and Computer-Assisted Intervention – MICCAI'99*, Berlin, Heidelberg, pp. 1031–1041. Springer Berlin Heidelberg.

Townsend, W. T. (1988). *The effect of transmission design on force-controlled manipulator performance*. Ph. D. thesis, Massachusetts Institute of Technology,Cambridge, Massachusetts.

Townsend, W. T. and J. K. Salisbury (1993). Mechanical design for whole-arm manipulation. In *Robots and Biological Systems: Towards a New Bionics?*, pp. 153–164. Springer.

Trivedi, D., C. D. Rahn, W. M. Kier, and I. D. Walker (2008). Soft robotics: Biological inspiration, state of the art, and future research. *Applied bionics and biomechanics 5*(3), 99–117.

Tugal, H., B. Gautier, B. Tang, G. Nabi, and M. S. Erden (2022). Hand-impedance measurements with robots during laparoscopy training. *Robotics and Autonomous Sys-*

tems 154, 104130.

UL (2019). White paper: Safety testing in healthcare robotics. White paper.

Van Ham, R., T. G. Sugar, B. Vanderborght, K. W. Hollander, and D. Lefeber (2009). Compliant actuator designs. *IEEE Robotics & Automation Magazine 16*(3), 81–94.

Versace, J. (1971). A review of the severity index. In *SAE Technical Paper Series. 15th Stapp Car Crash Conference (1971)*. SAE International.

Villani, L. (2008). *Force Control*, pp. 161–185. Berlin, Heidelberg: Springer Berlin Heidelberg.

Vukobratovic, M. and A. Tuneski (1994). Contact control concepts in manipulation robotics/spl minus/an overview. *IEEE Transactions on industrial electronics 41*(1), 12–24.

Whitney, D. E. (1977). Force feedback control of manipulator fine motions. *Journal of Dynamic Systems Measurement and Control-transactions of The Asme 99*, 91–97.

Yang, G.-Z., J. Cambias, K. Cleary, E. Daimler, J. Drake, P. E. Dupont, N. Hata, P. Kazanzides, S. Martel, R. V. Patel, V. J. Santos, and R. H. Taylor (2017). Medical robotics—regulatory, ethical, and legal considerations for increasing levels of autonomy. *Science Robotics 2*(4), eaam8638.

Yaşır, A., G. Kiper, and M. C. Dede (2020). Kinematic design of a non-parasitic 2r1t parallel mechanism with remote center of motion to be used in minimally invasive surgery applications. *Mechanism and Machine Theory 153*, 104013.

Yaşır, A. (2018). *Design of a 2R1T mechanism with remote center of motion for minimally invasive transnasal surgery applications*. Ph. D. thesis, Izmir Institute of Technology, Izmir, Turkey.

Yi, B.-J. and R. A. Freeman (1993). Geometric analysis of antagonistic stiffness in redundantly actuated parallel mechanisms. *Journal of Robotic systems 10*(5), 581–603.

Zahedi, F., J. Arnold, C. Phillips, and H. Lee (2021). Variable damping control for phri: Considering stability, agility, and human effort in controlling human interactive robots. *IEEE Transactions on Human-Machine Systems 51*(5), 504–513.

Zemiti, N., G. Morel, B. Cagneau, D. Bellot, and A. Micaelli (2006). Kinematic instability of kinematically constrained manipulators under pure force control. *IFAC Proceedings Volumes 39*(15), 260 – 265.

Zhang, H. (1989). Kinematic stability of robot manipulators under force control. In *Proceedings, 1989 International Conference on Robotics and Automation*, pp. 80–85 vol.1.

VITA

Orhan Ayit

Experience: (1) Teaching assistant - Me 407: Embedded Systems, Instructor: Assoc. Prof. Ahmet Onat (between Sept., 2013 – Feb., 2014) **(2)** Teaching assistant - Ens 206: Systems Modeling and Control, Instructor: Assoc. Prof. Ahmet Onat (between Feb., 2014 – June, 2014) **(3)** Teaching assistant - Me 407: Embedded Systems, Instructor: Assoc. Prof. Ahmet Onat (between Sept., 2013 – Feb., 2014) **(4)** Project assistant – "Quadruped Robot Design, Construction and Control" , Funded by The Scientific and Technological Research Council of Turkey (TÜBİTAK) (2015). **(5)** Project assistant – "NeuRoboScope: Robot Assisted endoscope Control that can be controlled by the surgical tools", Funded by The Scientific and Technological Research Council of Turkey (TÜBİTAK) (2016-2018). **(6)** Project assistant "Sualtında Manipülasyon İçin İnsansız Robot Mürekkepbalığı Geliştirilmesi ve Tasarımı", Funded by The Scientific and Technological Research Council of Turkey (TÜBİTAK) (2020 -2022).

Awards/Grant: 100/2000 CoHE (Council of Higher Education, TURKEY) Doctoral Scholarship.

Publications: Thesis: Ayit, O. "Contact Modeling as Applied to the Dynamic Simulation of Legged Robots", M.Sc. Thesis, 2015. **Articles: (1)** Hashlamon, I., Gülhan, M., Ayit, O., & Erbatur, K. (2017). A novel method for slip prediction of walking biped robots. Robotica, 35(4), 766-786. **(2)** Kanık, M., Ayit, O., Dede, M.İ.C., & Tatlicioglu, E. (2022). Toward safe and high-performance human–robot collaboration via implementation of redundancy and understanding the effects of admittance term parameters. Robotica, 40(7), 2112-2127. **(3)** Aldanmaz, A., Ayit, O., Kiper, G., & Dede, M. (2023). Gravity compensation of a 2R1T mechanism with remote center of motion for minimally invasive transnasal surgery applications. Robotica, 41(3), 807-820. **(4)** Ayit, O. and Dede M. İ. C., "A study on a computational efficient controller design for a surgical robotic system", International Journal of Dynamics and Control.(Under Review). **Peer-reviewed Conference Papers: (First Author): (1)** Ayit, O., Yaşır, A., Vardarlı, E., Kiper, G., & Dede, M. İ. C. (2018). Bir ameliyat robotunun denetimi için basitleştirilmiş dinamik modeli. TOK 2018 Bildiriler Kitabı. **(2)** Ayit, O., & Dede, M. İ. C. (2020). A New Correction Coefficient Formula for the Simplified Dynamic Model of a Surgical Robot. In New Trends in Medical and Service Robotics: MESROB 2020 (pp. 89-96). Cham: Springer International Publishing.